



THE UNIVERSITY OF QUEENSLAND
AUSTRALIA

TIDAL DWARF GALAXIES
IN GAS-RICH GROUPS

Sarah M. Sweet

BSc(Maths) BBusMan BSc(Hons I Phys) GCResComm

A THESIS SUBMITTED FOR THE DEGREE OF DOCTOR OF PHILOSOPHY AT
THE UNIVERSITY OF QUEENSLAND IN 2014
SCHOOL OF MATHEMATICS AND PHYSICS

Abstract

I develop new methods for identifying and measuring tidal dwarf galaxies, using a sample of galaxies within HI-rich groups that have no evidence of advanced major mergers. These groups are taken from the Survey of Ionization in Neutral Gas Galaxies (SINGG, Meurer et al., 2006), an optical follow-up survey to the HI Parkes All Sky Survey (HiPASS, Barnes et al., 2001). Fifteen of the fields contain four or more emission line galaxies and are named Choir groups. I detect new dwarf galaxies that are too small to be individually detectable in HiPASS; they are detectable in the SINGG narrow-band imaging because of their star formation and membership of these HI-rich groups. The Choir groups are compact, with a mean projected separation between the two brightest members of 190 kpc. They have comparable star formation efficiency (the ratio of star formation rate to HI mass) to the remaining SINGG fields. The Choir member galaxies also match the wider SINGG sample in their radii, H α equivalent width and surface brightness.

I define a new, more robust calibration for the metallicity diagnostic for identifying tidal dwarf galaxy candidates in the absence of tidal tails, based on the luminosity-metallicity relation with a consistent metallicity definition. Using that calibration, SDSS dwarfs fainter than $M_R = -16$ have a mean metallicity of $12 + \log(\text{O}/\text{H}) = 8.28 \pm 0.10$, regardless of their luminosity. Tidal dwarf galaxy candidates in the literature are elevated above this at $12 + \log(\text{O}/\text{H}) = 8.70 \pm 0.05$ on average. Our hydrodynamical simulations also predict that tidal dwarf galaxies should have metallicities elevated above the normal luminosity-metallicity relation. I compare 53 star-forming galaxies in 9 of the HI gas-rich Choir groups and find those brighter than $M_R \sim -16$ to be consistent with the normal relation defined by the SDSS sample. At fainter magnitudes my sample has a wide range in metallicity, suggestive of varying HI content and environment. Three (16%) of the dwarfs are strong tidal dwarf galaxy candidates ($12 + \log(\text{O}/\text{H}) > 8.6$), and four (21%) are very metal poor dwarfs ($12 + \log(\text{O}/\text{H}) < 8.0$); these are probably gas-rich dwarfs with recently ignited star formation.

I fit model mass-follows-light rotation curves to optical slit spectroscopic observations of 22 dwarf galaxies in the sample. Due to observational limitations, ten of these are of sufficient quality to measure mass-to-light (M/L) ratios. These are low ($M/L = 0.73 \pm 0.39 M_{\odot}/L_{\odot}$), consistent with the star-forming nature of these galaxies, though in most cases I do not measure out to radii where normal galaxies are dark-matter-dominated. I find a suggestion of a trend

towards higher M/L ratio with increasing luminosity and metallicity, albeit with large scatter. I find a relatively large pressure support component ($\sigma_D = 13.1 \pm 1.9 \text{ km s}^{-1}$), indicating that the galaxies are experiencing tidal fields. One galaxy has a strongly-falling rotation curve, which could be explained by 1) a rotating disk that becomes pressure-supported at large radii; 2) a tilted bar surrounded by a face-on disk; or, 3) a kinematic twist. I consider whether or not falling rotation curves can be measured, based on a tidal stripping model. The tidal radius r_{tidal} must be larger than twice the turnover radius r_{turn} where the rotation curve falls significantly, otherwise the baryons there do not remain bound and the measurement cannot be made. As much as half of this sample is affected by tidal stripping. Further to this, the H α light at this radius must be sufficiently bright to be detectable; this is only the case for three (14%) galaxies in my sample. It seems that the falling rotation curves predicted for tidal dwarf galaxies are rarely, if ever, observable.

Declaration by Author

This thesis is composed of my original work, and contains no material previously published or written by another person except where due reference has been made in the text. I have clearly stated the contribution by others to jointly-authored works that I have included in my thesis.

I have clearly stated the contribution of others to my thesis as a whole, including statistical assistance, survey design, data analysis, significant technical procedures, professional editorial advice, and any other original research work used or reported in my thesis. The content of my thesis is the result of work I have carried out since the commencement of my research higher degree candidature and does not include a substantial part of work that has been submitted to qualify for the award of any other degree or diploma in any university or other tertiary institution. I have clearly stated which parts of my thesis, if any, have been submitted to qualify for another award.

I acknowledge that an electronic copy of my thesis must be lodged with the University Library and, subject to the General Award Rules of The University of Queensland, immediately made available for research and study in accordance with the *Copyright Act 1968*.

I acknowledge that copyright of all material contained in my thesis resides with the copyright holder(s) of that material. Where appropriate I have obtained copyright permission from the copyright holder to reproduce material in this thesis.

Publications during candidature

Peer-reviewed publications

- Sweet, S. M., Drinkwater, M. J., Meurer, G., Bekki, K., Dopita, M. A., Kilborn, V., Nicholls, D. C.
Choirs, HI galaxy groups: the metallicity of dwarf galaxies.
The Astrophysical Journal **782**, 35-45 (2014)
- Sweet, S. M., Meurer, G., Drinkwater, M. J., Kilborn, V., Dénes, H., Bekki, K., Hanish, D., Ferguson, H., Knezek, P., Bland-Hawthorn, J., Dopita, M., Doyle-Pegg, M. T., Elson, E., Freeman, K., Heckman, T., Kennicutt, R., Kim, J. H., Koribalski, B., Meyer, M., Putman, M., Ryan-Weber, E., Smith, C., Stavelly-Smith, L., Wong, O. I., Webster, R., Werk, J., Zwaan, M.
Choirs, HI galaxy groups: catalogue and detection of star-forming dwarf group members.
Monthly Notices of the Royal Astronomical Society **433**, 543-559 (2013)

Publications included in this thesis

Paper One (incorporated as Chapter 2):

Sweet, S. M., Meurer, G., Drinkwater, M. J., et al. *Choirs, HI galaxy groups: catalogue and detection of star-forming dwarf group members.* Monthly Notices of the Royal Astronomical Society **433**, 543-559 (2013)

Statement of contributions for Paper One:

- Sweet (candidate): measured additional galaxies (100%), performed analysis (100%), wrote paper (100%).
- Meurer: inspected SINGG images by eye to identify Choir groups (100%), further inspected images to identify additional emission line galaxies (100%), constructed Figure 3 (100%), provided comments (25%).
- Drinkwater: wrote Appendix A notes (100%), provided comments (25%).
- Kilborn: manually remeasured HIPASS measurements for the groups; provided comments to the text (25%).
- Dénes: provided the HI scaling relation for calculating HI deficiency (100%).
- Bekki: provided comment (25%).
- Hanish: inspected SINGG images by eye to identify Choir groups (100%)

- Ferguson, Knezek, Bland-Hawthorn, Dopita, Doyle-Pegg, Elson, Freeman, Heckman, Kennicutt, Kim, Koribalski, Meyer, Putman, Ryan-Weber, Smith, Stavelly-Smith, Wong, Webster, Werk, Zwaan: provided SINGG images, and unpublished photometry (100%)

Paper Two (incorporated as Chapter 3):

Sweet, S. M., Drinkwater, M. J., Meurer, G., et al. *Choirs, HI galaxy groups: the metallicity of dwarf galaxies*. *The Astrophysical Journal* **782**, 35-45 (2014)

Statement of contributions for Paper Two:

- Sweet (candidate): wrote observing proposals (80%); conducted observations (90%); measured and analysed data (100%); wrote paper (100%).
- Drinkwater: wrote observing proposal (20%); assisted with observations (10%); assisted with data processing (100%); provided comments on the text (25%).
- Meurer: provided comments on the text (25%).
- Bekki: conducted simulations of tidal dwarf galaxies (100%); provided comments on the text (25%).
- Dopita: provided the metallicity diagnostic and helpful discussions on its implementation (100%).
- Kilborn: provided comments on the text (25%).
- Nicholls: provided measurements for two unpublished, isolated, gas-rich dwarf galaxies (100%)

Contributions by others to the thesis

I acknowledge the following contributions by others:

- Drinkwater: assisted with target selection (20%) and observations (10%) for Chapter 4
- Meurer: assisted with target selection (10%) for Chapter 4
- Kilborn: assisted with observations (20%) for Chapter 4
- Audcent-Ross: measured SINGG photometry for additional galaxies for Chapter 4
- Baumgardt: participated in helpful discussions and suggestions for analysis for Chapter

Statement of parts of the thesis submitted to qualify for the award of another degree

None.

Acknowledgements

I wish to thank my advisors Michael Drinkwater, Gerhardt Meurer and Holger Baumgardt for guiding me in this research and developing me as an astrophysicist. Michael, thank you especially for sharing your wisdom and encouragement, and entrusting me with observing trips from the beginning. Thank you also for your generous travel funding support. Gerhardt, thank you for hosting me during my visits to UWA.

Thank you to my colleagues Virginia Kilborn and Kenji Bekki; it has been an honour working with you in the Choirs project. Virginia, thank you for the access to Keck and your mentorship.

To David Parkinson, thank you for conducting my thesis review and to Tamara Davis, thank you for acting as chair of examiners. Thank you to my examiners Pierre-Alain Duc and Christy Tremonti for both providing a timely, thoughtful and constructive review of my thesis.

UQ Astro, you have made it a pleasure to do a PhD here: thank you for the sense of community.

I would particularly like to thank my dear husband Matthew for chairing the Sarah Sweet fan club and for bringing out the best in me.

I acknowledge receipt of an Australian Postgraduate Award, and additional travel funding from the School of Mathematics and Physics.

Keywords

Dwarf galaxy formation, tidal dwarf galaxies, galaxy groups, HI galaxy groups, metallicity, galaxy kinematics, integral field spectroscopy, multi-object spectroscopy.

Australian and New Zealand Standard Research Classification (ANZSRC)

ANZSRC code: 020103, Cosmology and Extragalactic Astronomy, 100%

Field of Research (FoR) Classification

FoR code: 0201, Astronomical and Space Sciences, 100%

Contents

List of Figures	xii
List of Tables	xiv
List of Abbreviations	xv
1 Introduction	1
1.1 Galaxy formation: implications of models and observations	1
1.2 Formation and properties of normal dwarf galaxies	2
1.3 Formation and properties of tidal dwarf galaxies	3
1.4 Specific significance of tidal dwarf galaxies	4
1.5 Tidal dwarfs in the literature	5
1.6 Thesis outline	6
2 Catalogue and Detection of Star-Forming Dwarf Members	8
3 The Metallicity of Dwarf Galaxies	27
4 The Kinematics of Gas-Rich Dwarf Galaxies	42
4.1 Chapter Outline	42
4.2 Background and Aims	43
4.3 Sample Selection, Observations and Data Processing	43
4.4 Results and Discussion	54
4.4.1 Luminosity-metallicity relation	54
4.4.2 Rotation curve modelling	55
4.4.3 Pressure support	58
4.4.4 Rotation curve quality	59

CONTENTS	xi
4.4.5 M/L ratios	60
4.4.6 Can the falling rotation curves of TDGs be detected?	61
4.4.7 The strongly-falling rotation curve of J0443-05:S4	64
4.5 Chapter Summary	66
5 Conclusions	79
5.1 Motivation	79
5.2 Aims	80
5.3 Catalogue and detection of star-forming dwarf group members	80
5.4 The metallicity of tidal dwarf galaxies	81
5.5 The kinematics of tidal dwarf galaxies	81
5.6 Future work	82
References	84

List of Figures

4.1	SINGG image of HIPASS J0443-05	46
4.2	SINGG image of HIPASS J1051-17	47
4.3	SINGG image of HIPASS J1059-09	48
4.4	SINGG image of HIPASS J1403-06	49
4.5	Luminosity-metallicity relation	55
4.6	SINGG image, DEIMOS spectrum and rotation curve for HIPASS J0443-05:S4.	57
4.7	Mass-to-light ratio as a function of the luminosity-metallicity relation.	61
4.8	Tidal radius vs. effective radius	64
4.9	SINGG image, DEIMOS spectrum and rotation curve for HIPASS J0443-05:S3	68
4.10	as above for HIPASS J1051-17:S3	68
4.11	as above for HIPASS J1051-17:S4	69
4.12	as above for HIPASS J1051-17:S5	69
4.13	as above for HIPASS J1051-17:S6	70
4.14	as above for HIPASS J1051-17:S7	70
4.15	as above for HIPASS J1051-17:S8	71
4.16	as above for HIPASS J1051-17:g07	71
4.17	as above for HIPASS J1051-17:g07	72
4.18	as above for HIPASS J1051-17:g11	72
4.19	as above for HIPASS J1051-17:g13	73
4.20	as above for HIPASS J1051-17:2905	73
4.21	as above for HIPASS J1059-09:S2	74
4.22	as above for HIPASS J1059-09:S5	74
4.23	as above for HIPASS J1059-09:S7	75
4.24	as above for HIPASS J1059-09:S8	75

4.25 as above for HIPASS J1059-09:S9	76
4.26 as above for HIPASS J1059-09:S10	76
4.27 as above for HIPASS J1403-06:S3	77
4.28 as above for HIPASS J1403-06:S4	77
4.29 as above for HIPASS J1403-06:595	78

List of Tables

4.1 Measured quantities for group member galaxies, including new group members.
Columns (1) to (11). 50

4.1 Columns (12) to (23). 52

List of Abbreviations

2MASS	2-Micron All-Sky Survey, extended source catalogue
6dF	6-degree field of view
AB mag	AB magnitude system
ALFA	Arecibo L-band feed array
ALFALFA	Arecibo Legacy Fast ALFA
APMUKS	automated plate measurement United Kingdom Schmidt
BCD	blue compact dwarf
C	classical observing mode
CTIO	Cerro Tololo Inter-American Observatory
Dec., Decl.	declination
DEF_{HI}	HI deficiency
dE,N	nucleated dwarf elliptical
DM	dark matter
DR8	eighth data release
ELdot	emission line dot
ELG	emission line galaxy
ESO	European Southern Observatory
EW	equivalent width
FLASH	first large absorption survey in HI
$F_{H\alpha}$	$H\alpha$ flux
g_{SDSS}	g -band SDSS magnitude
GALEX	galaxy evolution explorer
GASS	GALEX Arecibo SDSS Survey
GNX	Galaxies North field X

H	hydrogen
H α	hydrogen- α
H β	hydrogen- β
HCG	Hickson compact group
HI	neutral hydrogen
HII	singly-ionized hydrogen
HiPASS	HI Parkes All Sky Survey
HOPCAT	HiPASS optical catalogue
IC	index catalog
IFU	integral field unit
IMF	initial mass function
IDL	interactive data language
Int. Time	integration time
IPAC	Infrared Processing & Analysis Center
IRAF	image reduction and analysis facility
k	number of clusters
kpc	kiloparsec
KS	Kolmogorov-Smirnov
LG	Local Group
LMC	Large Magellanic Cloud
log	base-10 logarithm
MGC	Millennium Galaxy Catalogue
MRK	Markarian
MRSS	Muenster Red Sky Survey
MW	Milky Way
M_*	stellar mass
M_\odot	solar mass
M_{HI}	mass of neutral hydrogen
M_{HIexp}	expected mass of neutral hydrogen
M_{HIobs}	observed mass of neutral hydrogen
M_R	R -band magnitude
$M_{R(AB)}$	R -band AB magnitude
$M_{R(SDSS)}$	R -band SDSS magnitude

Mag_{RSC}	<i>R</i> -band SuperCosmos magnitude
Mag_{RAB}	<i>R</i> -band AB magnitude
M/L_R	<i>R</i> -band mass-to-light ratio
N	nod and shuffle observing mode
[<i>Nii</i>]	singly-ionized nitrogen forbidden emission line
NASA	National Aeronautics and Space Administration
NED	NASA/IPAC Extragalactic Database
NGC	New General Catalogue
N_{ns}	number of new stars
NUV	near ultra-violet
O	oxygen
[<i>Oiii</i>]	doubly-ionized oxygen forbidden emission line
Obs. Date	observing date
q	ionization parameter
RA, R.A.	right ascension
r_e	effective radius
r_{SDSS}	<i>r</i> -band SDSS magnitude
R_{Vega}	<i>R</i> -band Vega magnitude
R_{AB}	<i>R</i> -band AB magnitude
S	sub-aperture nod and shuffle observing mode
[<i>Sii</i>]	singly-ionized sulfur forbidden emission line
SDSS	Sloan Digital Sky Survey
SEGC	Sloan Extension for Galactic Understanding and Exploration catalogue
SEL	strong emission line
SINGG	Survey for Ionization in Neutral Gas Galaxies
SFE	star formation efficiency
SFE_T	total (group) star formation efficiency
SFR	star formation rate
SMC	Small Magellanic Cloud
sSFR	specific star formation rate
TDG	tidal dwarf galaxy
μ_e	effective surface brightness
UV	ultra-violet

V_{hel}	heliocentric velocity
WiFeS	wide field spectrograph
z	redshift

1

Introduction

In this chapter I give an overview of galaxy formation, dwarf galaxies, and the specific significance of tidal dwarf galaxies. I also provide general motivation for the use of a sample of star-forming, HI-rich groups for the study of tidal dwarf galaxies (TDGs). Each of the following chapters contains a more detailed background as appropriate for each topic.

1.1 Galaxy formation: implications of models and observations

In the standard model of our universe, structure formation occurs through hierarchical build-up of dark matter (DM) haloes containing galaxies (Klypin et al., 1999). These haloes interact and merge over time, forming small groups and large clusters of galaxies arranged in a web-like structure of connecting filaments and spacing voids.

This cosmological understanding is based upon our current theories of local physics plus the

invocation of DM and new physics such as dark energy as instructed by observations of galaxies, groups and clusters. However, there are serious discrepancies between observations and the simulations that attempt to model them. For example, while the galaxy stellar mass function is matched at L_* galaxies, DM simulations consistently overpredict the number of low-mass galaxies (the ‘missing satellites problem’, e.g. Klypin et al., 1999; Moore et al., 1999). Many models have attempted to correct this by the inclusion of additional physics such as ‘warm’ DM, supernova feedback or UV irradiation (e.g. Bode et al., 2001; Benson et al., 2002, 2003), but it is not clear which of these is dominant. Others have approached the problem by artificially tuning the models so that fewer galaxies form in low-mass haloes (e.g. Guo et al., 2010; Font et al., 2011), but this solution is not physically motivated. Further, only one galaxy formation channel is currently included in these cosmological simulations as the relative importance of other channels is not known.

The galaxy group environment is observed to play an important role in galaxy formation and evolution; changes in properties such as star formation, morphology and gas-richness are seen at this environmental density (Lewis et al., 2002; Gómez et al., 2003). The group environment is therefore used as a reference point for simulations. Our observations of the Local Group (LG) are the basis for this calibration, as it is this group that is best observed by virtue of its proximity to us (Boylan-Kolchin et al., 2012). However, it is unknown whether or not the LG is typical of other groups in the Universe (Benson et al., 2002), so the models may be incorrectly calibrated. In addition to this, dwarf galaxies are progressively more difficult to observe at further distances from the LG, so the stellar mass function is currently poorly constrained at low masses (e.g. Bell et al., 2003; Baldry et al., 2012). Part of the tension with simulations could therefore potentially be resolved with future improvements to observational sensitivity.

1.2 Formation and properties of normal dwarf galaxies

While galaxies of all masses are the standard observational tracers of cosmological structure and its formation, dwarf galaxies are particularly ideal for tracing the gravitational potential and environmental assembly of the groups and clusters to which they belong. They are test particles that are sensitive to structure formation and evolution due to their small, compact nature. Moreover, they are sufficiently numerous to provide a high spatial density of data

(Fontana et al., 2006).

Most galaxies are born as dwarf galaxies in their own dark matter haloes, which attract baryonic matter in the form of gas and provide the necessary gravitational fields to cause star and therefore galaxy formation. Because of the surrounding dark matter, measurements of galaxy rotational velocity show a flat rotation curve elevated above a mass-follows-light profile as described in Freeman (1970). This phenomenon has been observed in many galaxies spanning a wide range in stellar mass (e.g. Freeman, 1970; de Blok et al., 1996; van Zee et al., 1997), and is consistent with the current hierarchical model of galaxy assembly in which galaxies are born in DM haloes (Navarro et al., 1997). As DM haloes merge, the galaxies within them also merge, forming larger and larger galaxies over time (Klypin et al., 1999).

The ratio relative to hydrogen of heavier elements, known as metallicity, also increases with galaxy age. This is due to ongoing metal production in stars and subsequent distribution of these metals during the supernova death of the stars (Larson, 1974). Massive galaxies are better able to retain the supernova ejecta and/or recycle the enriched gas into new stars than low-mass galaxies are (Gibson & Matteucci, 1997; Kauffmann et al., 2003; Dalcanton, 2007). These two processes of halo merging and self-enrichment result in the observed luminosity-metallicity relation. In general, small, faint galaxies are metal-poor, while big, bright galaxies are metal-rich (Lequeux et al., 1979; Garnett & Shields, 1987; Skillman et al., 1989; Brodie & Huchra, 1991; Zaritsky et al., 1994; Tremonti et al., 2004).

Consequently, in the context of the hierarchical model, dwarf galaxies have low luminosity, large dark matter haloes, and low metallicity.

1.3 Formation and properties of tidal dwarf galaxies

However, it is not well understood whether or not there is another significant formation channel for dwarf galaxies. Consequently no other formation channels are currently included in cosmological simulations. One process that has received growing attention is that of tidal formation. In this scenario, interactions between the gas-rich giant galaxies within groups can provide the required tidal fields for gas to condense into massive star clusters (e.g. at the end of one tail of the Antennae galaxies; Mirabel et al., 1992). When detached from the giant galaxies these systems are then known as tidal dwarf galaxies (TDGs). Simulations such as Bournaud & Duc (2006) predict that TDGs form mainly in major, gas-rich mergers. These galaxies do

not contain DM because the local DM particles belonging to the giant galaxies have a velocity that is greater than the escape velocity of the new TDG (Bournaud, 2010). This absence of DM leads to falling (mass-follows-light) rotation curves and low mass-to-light (M/L) ratios. In addition, local TDGs have a high metallicity, being composed of pre-enriched material¹ (Bournaud, 2010). These TDGs are formed in streams of gas, old stars and new stars formed out of the shocked gas. The streams are not gravitationally bound, so are theoretically expected to dissipate and fade over time. This prediction is confirmed by observational evidence of a faint stellar streams that surrounds a 4 Gyr TDG (Duc et al., 2014). TDGs are generally defined as being gravitationally bound objects that form in tidal debris and have masses consistent with dwarf galaxies (Duc et al., 2000).

TDGs in the local universe have the following observable characteristics, which can be used for their classification: they -

1. have **high metallicity** because they are formed from the pre-enriched material of their hosts,
2. have **falling rotation curves** because they do not form in their own dark matter halo, and,
3. are **embedded in stellar streams** composed of old and new stars formed from shocked gas.

1.4 Specific significance of tidal dwarf galaxies

To reiterate, the observed dwarf galaxy stellar mass function poses a particular problem for cosmological simulations. It is important to understand the relative importance of dwarf galaxy formation methods in order to better instruct the simulations. For TDGs in particular, the dwarf galaxy mass function is affected by the fraction of TDGs that survive the intense tidal fields in which they form (Bournaud, 2010). If this fraction is significant then the missing satellite problem may be deepened.

TDGs also have special significance in theories of gravity, as the dark matter fraction and rotation curves of these objects can provide necessary tests of alternative theories (Gentile et al.,

¹On the other hand, TDGs in the high-redshift universe should have a low metallicity, along with their metal-poor progenitors. This thesis deals only with local TDGs.

2007). For example, a falling galaxy rotation curve indicative of a lack of dark matter would be in tension with theories that ascribe flat rotation curves to a modification to Newtonian dynamics (MOND; e.g. Milgrom, 1983; Sanders & McGaugh, 2002; Milgrom, 2007; Kroupa et al., 2012). These models predict a flat rotation curve for all types of galaxies, including TDGs.

1.5 Tidal dwarfs in the literature

Current efforts to classify and measure tidal dwarf galaxies suffer from several difficulties. Most TDG candidates in the literature are discovered due to their location in the young tidal streams in which they are forming (e.g. Mirabel et al., 1992; Iglesias-Paramo & Vilchez, 1997; Duc & Mirabel, 1998; Duc et al., 2000; Weilbacher et al., 2000; Duc et al., 2011). Because these streams are still young, the TDG candidates within them have not yet reached dynamical equilibrium, meaning that it is not possible to make an accurate virial mass measurement and confirm whether or not they are bonafide TDGs (Casas et al., 2012). Consequently there is little reliable evidence for falling rotation curves (*c.f.* Carignan & Purton, 1998). Flat or rising rotation curves in apparent TDGs are variously attributed to the presence of baryonic DM (Bournaud et al., 2007) or MOND (Gentile et al., 2007), or simply do not probe to sufficient distances to reach the DM-dominated region (Mendes de Oliveira et al., 2001).

Confirmed TDGs (both real and simulated) generally have high metallicity (e.g. Weilbacher et al., 2000; Weilbacher et al., 2003; Sweet et al., 2014; Duc et al., 2014). However, the different galaxy samples from which they are drawn are measured using different metallicity calibration methods. Unfortunately there is a wide variation in metallicity between these calibration methods, so a galaxy measured with one type of metallicity calibration cannot be compared against a control sample measured with a different one (Kewley & Ellison, 2008).

Other optical properties of tidal dwarf galaxies have been proposed for differentiating TDGs from normal dwarfs. Star formation rate is not useful; most observed TDGs are young and have significant star-formation like their DM-rich counterparts (e.g. Mirabel et al., 1992; Iglesias-Paramo & Vilchez, 1997; Duc et al., 2000; Duc et al., 2011), while the oldest TDG measured has an age of 4 Gyr and a low star-formation rate (Duc et al., 2014). It has recently been suggested that the low surface brightness and large effective radius of TDGs might provide a distinct region of parameter space useful for their detection (Duc et al., 2014), though this alone

is not sufficient to positively classify a TDG and additional tests such as metallicity are still required. Furthermore, the faintness of TDGs renders it difficult to detect them at significant distances. Because of the difficulty in identifying TDGs, it is not known how important this formation channel is in the formation of all dwarf galaxies. Predictions range from ‘several’ (Bournaud & Duc, 2006) to 50% (Hunsberger et al., 1996). Moreover, the survival rate of TDGs is also unknown (Duc & Mirabel, 1998; Weilbacher et al., 2000; Ploeckinger et al., 2014), further complicating the issue.

To date, no observation of a TDG meets all three criteria listed above. TDG candidates in the literature are identified on the basis of surrounding tidal streams; metallicities are sometimes measured, but the different calibrations cannot be compared between samples; no convincing falling rotation curve has been measured.

1.6 Thesis outline

In this work I address the problems outlined above by developing new methods to classify and measure TDGs.

Chapter 2 is comprised of Paper 1: catalogue and detection of dwarf galaxies in HI-rich galaxy groups. This paper describes the sample for the thesis. My sample comes from the star-forming dwarf galaxies within ‘Choir groups’, groups of galaxies identified in a HI mass-selected sample (HIPASS; Barnes et al., 2001). These groups span a more representative sample of environment than the small fraction of groups containing tidal tails in which TDG candidates in the literature have been found. As such the Choir groups provide an ideal location for checking the extent to which TDGs can form in fly-bys and weak interactions rather than major mergers. Importantly, the groups in my sample are not in an advanced stage of merging, which would distort the velocity and mass measurements. In addition, the star-forming nature of the dwarfs facilitates emission line metallicity measurement, which is much more efficient than absorption line studies and therefore allows a larger sample to be measured. It also allows detection of several new dwarf galaxy group members based on their location in the HI-selected group.

Chapter 3 contains Paper 2 on the metallicity of the galaxies in my sample. Here I address the virial equilibrium problem by selecting TDG candidates based on my metallicity-luminosity diagnostic instead of their location in a tidal stream. My use of a new, consistent metallicity calibration to define my diagnostic ensures that TDG candidates are not incorrectly classified.

I identify three TDG candidates using this method.

In Chapter 4 I employ high-quality Keck telescope spectroscopic measurements of a selection of TDG candidates to measure their rotation curves and test for the absence of dark matter. The data are very complex, with no direct evidence for an absence of dark matter. I also discuss observational difficulties in measuring falling rotation curves, and physical reasons why such measurements are rarely possible, if at all.

Finally in Chapter 5 I briefly summarise my conclusions in the context of the literature.

2

Catalogue and Detection of Star-Forming Dwarf Members

The first paper in this series introduces the sample for this work. I use narrow-band $H\alpha$ emission line detection of galaxy members to gather a sample of galaxy groups in a blind HI survey. This leads to the detection of faint dwarf galaxies that would be missed if isolated, but are detectable because they are in the same field of view as the larger, HI-rich galaxies. The galaxies in these groups have similar size, $H\alpha$ equivalent width and surface brightness to the single galaxies, pairs and triples from the HI survey. The groups are not in an advanced stage of merging, and many of the groups do not have the young, expanding optical tidal tails that make TDG velocity and mass measurements unreliable. Instead, they provide an ideal environment to detect TDGs that form from recent fly-bys or weak interactions. Further, the fact that the dwarf galaxies are star-forming allows detection and measurement via emission lines of a greater number of galaxies than absorption line studies would allow.



Choirs, H I galaxy groups: catalogue and detection of star-forming dwarf group members

Sarah M. Sweet,^{1*} Gerhardt Meurer,^{2,3} Michael J. Drinkwater,¹ Virginia Kilborn,⁴ Helga Dénes,⁴ Kenji Bekki,^{2,3} Dan Hanish,⁵ Henry Ferguson,⁶ Patricia Knezek,⁷ Joss Bland-Hawthorn,⁸ Michael Dopita,⁹ Marianne T. Doyle-Pegg,¹ Ed Elson,^{2,3} Ken Freeman,⁹ Tim Heckman,⁵ Robert Kennicutt,^{10,11} Ji Hoon Kim,¹² Bärbel Koribalski,¹³ Martin Meyer,^{2,3} Mary Putman,¹⁴ Emma Ryan-Weber,¹⁰ Chris Smith,¹⁵ Lister Staveley-Smith,^{2,3} O. Ivy Wong,¹³ Rachel Webster,¹⁶ Jessica Werk¹⁴ and Martin Zwaan¹⁷

¹*School of Mathematics and Physics, University of Queensland, QLD 4072, Australia*

²*School of Physics, University of Western Australia, 35 Stirling Highway, Crawley, WA 6009, Australia*

³*International Centre for Radio Astronomy Research, ICRAR M468, 35 Stirling Highway, Crawley, WA 6009, Australia*

⁴*Mail number H30, Swinburne University of Technology, PO Box 218, Hawthorn, Victoria 3122, Australia*

⁵*Infrared Processing and Analysis Center, California Institute of Technology, 100-22, Pasadena, CA 91125, USA*

⁶*Space Telescope Science Institute, 3700 San Martin Drive, Baltimore, MD 21218, USA*

⁷*WIYN Consortium, Inc., 950N Cherry Avenue, Tucson, AZ 85719, USA*

⁸*Sydney Institute for Astronomy, School of Physics, University of Sydney, Camperdown, NSW 2006, Australia*

⁹*Research School of Astronomy & Astrophysics, Mount Stromlo Observatory, Cotter Road, Weston Creek, ACT 2611, Australia*

¹⁰*Institute of Astronomy, University of Cambridge, Madingley Road, Cambridge CB 0HA, UK*

¹¹*Department of Astronomy, University of Arizona, 933 North Cherry Avenue, Tucson, AZ 85721-0065, USA*

¹²*Center for the Exploration of the Origin of the Universe, Astronomy Program, Department of Physics and Astronomy, Seoul National University, Seoul, Republic of Korea*

¹³*CSIRO Astronomy and Space Science, Australia Telescope National Facility, PO Box 76, Epping, NSW 1710, Australia*

¹⁴*University of Michigan, 830 Dennison, 500 Church Street, Ann Arbor, MI 48109-1042, USA*

¹⁵*Cerro Tololo Inter-American Observatory (CTIO), part of the National Optical Astronomy Observatory (NOAO), Colina El Pino S/N, Casilla 603, La Serena, Chile*

¹⁶*School of Physics, University of Melbourne, Parkville, Victoria 3010, Australia*

¹⁷*European Southern Observatory, Karl-Schwarzschild-Str. 2, D-85748 Garching b. München, Germany*

Accepted 2013 April 28. Received 2013 April 22; in original form 2012 November 7

ABSTRACT

H α observations centred on galaxies selected from the H I Parkes All-Sky Survey (HiPASS) typically show one and sometimes two star-forming galaxies within the ~ 15 arcmin beam of the Parkes 64 m H I detections. In our Survey for Ionization in Neutral Gas Galaxies (SINGG) we found 15 cases of HiPASS sources containing four or more emission line galaxies (ELGs). We name these fields Choir groups. In the most extreme case, we found a field with at least nine ELGs. In this paper, we present a catalogue of Choir group members in the context of the wider SINGG sample.

The dwarf galaxies in the Choir groups would not be individually detectable in HiPASS at the observed distances if they were isolated, but are detected in SINGG narrow-band imaging due to their membership of groups with sufficiently large total H I mass. The ELGs in these groups are similar to the wider SINGG sample in terms of size, H α equivalent width and surface brightness.

Eight of these groups have two large spiral galaxies with several dwarf galaxies and may be thought of as morphological analogues of the Local Group. However, on average our groups

*E-mail: sarah@sarahsweet.com.au

are not significantly H I deficient, suggesting that they are at an early stage of assembly, and more like the M81 group. The Choir groups are very compact at typically only 190 kpc in projected distance between the two brightest members. They are very similar to SINGG fields in terms of star formation efficiency (SFE; the ratio of star formation rate to H I mass), showing an increasing trend in SFE with stellar mass.

Key words: galaxies: groups: general – galaxies: dwarf – Local Group – radio continuum: galaxies.

1 INTRODUCTION

Galaxies are arranged throughout the Universe in a hierarchy of environments ranging from clusters to groups, to isolation (e.g. Tully 1987; Kilborn et al. 2009; Pisano et al. 2011). Galaxies that reside within denser environments such as clusters are different from those at group densities and yet still different from those that lie in the field. The amount of star formation depends largely on the amount of gas available to fuel the process (Kennicutt 1989, 1998; Bergvall 2012). Moreover, at group densities, the ratio of star-forming spiral galaxies to less prolific elliptical galaxies is lower, so morphology is important as well (Wijesinghe et al. 2012). It is not known exactly how groups transition from gas- and spiral-rich to gas-poor, elliptical-rich ones like those analysed by Kilborn et al. (2009) and Mulchaey & Zabludoff (1998) so the picture is incomplete. Groups of galaxies are particularly interesting because the suppression of star formation begins at group densities (Lewis et al. 2002; Gómez et al. 2003).

The selection technique for star formation studies can lead to inherent biases in the sample. Previous authors have used H α to select their samples (e.g. Gallego et al. 1995; Salzer et al. 2000). However, H α follow-up imaging studies of optically selected galaxies are limited by the selection biases of their parent sample, typically excluding low-surface-brightness galaxies. The result is that these surveys are biased towards galaxies with high rates of star formation, and contain no control sample with low star formation rates (SFRs).

In order to overcome that optical bias, we have selected galaxies based on their H I mass measured by the H I Parkes All-Sky Survey (HiPASS; Barnes et al. 2001; Koribalski et al. 2004; Meyer et al. 2004). With this sample we conducted the Survey for Ionization in Neutral Gas Galaxies (SINGG), an H α and *R*-band imaging follow-up to HiPASS. Meurer et al. (2006) present the SINGG sample, and give data on 93 HiPASS targets observed for SINGG. Now a total of 292 HiPASS targets have been observed by SINGG with the Cerro Tololo Inter-American Observatory (CTIO) 1.5 and 0.9 m telescopes (Meurer et al., in preparation). It is these images which form the basis of this study. 15 fields were discovered to contain four or more H α sources and were dubbed Choir groups. The Choir member galaxies are different from typical field galaxies in that the larger galaxies are distorted and none are elliptical galaxies.

In this paper we present a catalogue of Choir group members. Section 2 outlines the sample selection and observations of SINGG. We present our catalogue of Choir group members in Section 3, along with a discussion of their properties in the context of SINGG. Section 4 concludes the paper.

We base distances on the multipole model of Mould et al. (2000), with $H_0 = 70 \text{ km s}^{-1} \text{ Mpc}^{-1}$ as in Meurer et al. (2006). We adopt a Chabrier (2003) initial mass function (IMF).

2 SAMPLE SELECTION AND DATA

Our sample is drawn from the 292 HiPASS targets observed for SINGG. H I measurements are all from the HiPASS H I catalogue HICAT (Meyer et al. 2004), except for two groups (HiPASS J0443–05 and J1059–09). After noticing an anomalous H I mass for one group, we manually remeasured the H I mass of every Choir group. We found that the unusual H I profiles of the Choir fields caused the automated HiPASS parametrization algorithm to fit poorly in these two cases. Our manually remeasured H I masses are used in this paper for these two fields.

The SINGG observations were mostly conducted at the CTIO 1.5 m telescope, whose field of view of 14.7 arcmin matches the ~ 15 arcmin beam of the Parkes radio telescope well. Additional observations were taken at the CTIO 0.9 m telescope whose field of view is 13.5 arcmin.

Emission line galaxies (ELGs) in SINGG were identified by eye by two of us (DH, GRM) primarily using colour composites of the SINGG data where the red, green and blue images of the display were assigned to the net H α image, the narrow-band image without any continuum subtraction and the *R*-band image, respectively. The colour images are similar to those shown in Fig. B1. ELGs are distinguished by having net line emission, and being noticeably more extended than a point source. For unresolved emission line sources (ELdots; Ryan-Weber et al. 2004; Werk et al. 2010) the distance is not clear. They may be detached H II regions revealed by H α emission or background emitters of other lines (especially [O III] 5007) redshifted into our passband. Ancillary spectroscopy is needed to distinguish between these possibilities, and that is beyond the scope of this work; the ELdots in the Choir fields are not discussed further in this paper. The original data were consulted in the cases where the reality of the line emission was not clear, i.e. low-surface-brightness or low-equivalent-width (EW) objects. The images were then measured using the standard SINGG data analysis pipeline (Meurer et al. 2006).

While most of the (H I-rich, $15 \times 15 \text{ arcmin}^2$) fields in SINGG contain a single ELG, there are 15 fields that have four or more ELGs. These fields of multiple SINGGers we name Choir groups, presented in Table 1.

Our working assumption is that the line emission results from H α at a velocity similar to the HiPASS source, and hence that all ELGs in a field are physically associated. This is in the same manner as Tully et al. (2006), who argued that associations of dwarf galaxies in their sample were bound. For each field, the narrow-band filter was chosen to most closely match the mean wavelength and wavelength range of the filter to the H I velocity profile of the field. The pivot wavelengths and transmission widths are listed in Table 1. Typically filters with bandwidth $\sim 30 \text{ \AA}$ were used for the narrow-band images of these particular SINGG fields. This corresponds to $\sim 3000 \text{ km s}^{-1}$, much broader than the typical H I line widths involved. Therefore, spectroscopic data are needed to firmly

Table 1. Summary of Choir groups.

HIPASS+	Optical ID	RA	Dec.	Dist.	FOV	ELGs	Comp.	$M_{\text{H I}}$	H I def.	$V_{\text{H I}}$	$W_{\text{H I}}$	$W_{50, F}$
(1)	(2)	(h m s)	(d m s)	(Mpc)	(kpc)	(7)	(kpc)	(dex)	(dex)	(km s ⁻¹)	(km s ⁻¹)	(km s ⁻¹)
(1)	(2)	(3)	(4)	(5)	(6)	(7)	(8)	(9)	(10)	(11)	(12)	(13)
J0205–55	AM 0203-552	02 05 05.48	–55 06 42.55	93	406	9	366	10.51	0.03 ^b	6524	193	5051-8297
J0209–10	HCG 16	02 09 42.71	–10 11 01.36	54	236	4	56.2	10.31	0.18	3900	243	2560-5668
J0258–74		02 58 06.48	–74 27 22.79	70	305	4	236	10.41	–0.34	4805	399	2560-5668
J0400–52	Abell 3193	04 00 40.82	–52 44 02.72	151	659	9	420	10.61	0.13	10566	298	8182-11750
J0443–05		04 43 43.90	–05 19 09.91	69	301	5	209	10.41 ^a	0.02	4877	278	2560-5668
J1026–19		10 26 40.81	–19 03 04.03	135	589	6	107	10.63	–0.28	9094	242	6857-9142 ^c
J1051–17		10 51 37.46	–17 07 29.24	83	362	9	216	10.45	–0.26	5477	522	4205-7679
J1059–09	USGC S154	10 59 16.25	–09 47 38.15	122	532	10	283	10.42 ^a	0.20	8175	80.0	6857-9142
J1159–19	ARP 022	11 59 30.13	–19 15 54.86	25	109	4	29.5	9.92	0.00	1668	150	1188-2651
J1250–20		12 50 52.84	–20 22 15.64	114	497	7	123	10.51	–0.11	7742	169	5051-8297
J1403–06	ARP 271	14 03 24.88	–06 04 09.16	41	179	4	27.5	10.29	0.09	2591	330	2217-3725
J1408–21		14 08 42.04	–21 35 49.81	128	559	6	184	10.52	0.05	8732	203	6857-9142
J1956–50		19 56 45.51	–50 03 20.30	110	480	4	299	10.52	–0.33	7446	321	4205-7679 ^c
J2027–51	AM 2024-515	20 28 06.39	–51 41 29.83	87	380	4	224	10.44	–0.22	5881	356	4205-7679
J2318–42a	Grus Quartet	23 16 10.80	–42 35 05.00	23	100	4	73.1	10.10	0.15 ^b	1575	222	1188-2651

Notes. Columns: (1) Name assigned to field in HiPASS. (2) Name assigned to group as found in NASA/IPAC Extragalactic Database (NED; <http://ned.ipac.caltech.edu/>). (3) J2000 right ascension of brightest source in field. (4) J2000 declination of brightest source in field. (5) Distance based on the multipole attractor model as in Mould et al. (2000) and adopting $H_0 = 70 \text{ km s}^{-1} \text{ Mpc}^{-1}$. (6) Field of view of ~ 15 arcmin at the distance of the group. (7) Number of ELGs. (8) Projected group compactness, estimated by projected separation of two largest group members. See Section 3.5. (9) Logarithm of group H I mass from HiPASS. ^aWe remeasured H I mass for two groups whose HiPASS measurements were incorrect. See Section 2 for more details. (10) H I deficiency parameter defined as the logarithmic difference between the observed group H I mass and predicted group H I mass (determined by summing the predicted H I masses of the individual group galaxies). See Section 3.7 for calculation and discussion. ^bWe exclude these two groups from our H I deficiency analysis due to field-of-view restrictions. (11) Heliocentric H I velocity. (12) Observed H I emission width. (13) Narrow-band filter velocity range. ^cWe note that the narrow-band filters used for these two fields overlap but do not completely cover the extent of the observed H I emission width. Therefore, there may be additional ELGs associated with these groups which would be classified as Choir member galaxies but are not detected in our imaging.

associate all ELGs with the HiPASS detection. We are in the process of confirming redshifts and these will be published in a future paper.

As this project progressed, we noticed that some ELGs were missed in the original selection of the Choir fields. These included some small high-surface-brightness galaxies as well as low-surface-brightness and low-EW detections. We also found cases where the morphology of a single galaxy was better described as multiple merging or superposed galaxies. In those cases what distinguishes the companions as separate ELGs is a noticeable concentration in both H α and the R-band continuum. H II regions, on the other hand, are distinguished by having a relatively weak continuum above the local background and being unresolved or barely resolved in H α .

After discovering a few instances of ‘new’ ELGs, one of us (GRM) carefully examined all Choir fields, as well as SINGG fields with three ELGs. In total we found 13 new ELGs. These are distinguished in Table 2 by an asterisk (*). While we think the evidence is strong that all ELGs listed here are separate galaxies with real H α emission, we caution that there are some borderline cases, such as HiPASS J1408–21:S6, where the line emission has a low surface brightness and is displaced from the parent galaxy. While we do believe that our selection based on visual inspection is thorough, spatially varying biases and subjectivity are likely. For example, while a strong blue compact dwarf (BCD) candidate like HiPASS J1051–17:S6 may be recognized even if it is projected near a brighter companion, a small galaxy with only one or two modest H II regions, such as HiPASS J0205–55a:S9, is easily noticed when isolated, but may not be recognized as a separate galaxy if projected on or near a bright spiral. H α concentrations along extended tidal arms, such as HiPASS J1250–20:S5,S6, are especially ambiguous. It is not clear whether they are separate tidal dwarf galaxies (e.g., Bournaud et al. 2007) or just transitional H II regions.

The new ELGs in the sample were not measured using the SINGG measurement pipeline, since it was not operational when the measurements were required. Instead, basic measurements of position and fluxes were measured using IMEXAM in IRAF.¹

In summary, the following criteria must be met to satisfy our Choir group definition:

- (i) H I detection in HiPASS;
- (ii) four or more ELGs in a single field of view of ~ 15 arcmin;
- (iii) where an ELG is defined by net H α emission in an extended source.

We point out that the above is the *minimum* to define a Choir group. The definition has the following caveats:

- (i) Choir groups can be larger than 15 arcmin, with members outside of the field of view;
- (ii) Choir groups can therefore belong to much larger structures, e.g. HiPASS J0400–52, which is in Abell 3193;
- (iii) Choir groups require spectroscopic follow-up to confirm assumed physical association.

These caveats are discussed more fully in Section 3.

We present the Choir groups in Table 1, and key properties of the individual Choir group members in Table 2. These data are preliminary results on all the galaxies observed with the CTIO 1.5 and 0.9 m telescopes for SINGG. Full results are in preparation and will be presented elsewhere (Meurer et al., in preparation).

¹ IRAF is distributed by the National Optical Astronomy Observatories, which are operated by the Association of Universities for Research in Astronomy, Inc., under cooperative agreement with the National Science Foundation (Tody 1993).

Table 2. Choir member descriptions.

SINGG name HIPASS+ (1)	Optical ID (2)	RA (h m s) (3)	Dec. (d m s) (4)	r_c (arcsec) (5)	Axial ratio (6)	M_R (AB mag) (7)	$\log(F_{\text{H}\alpha})$ ($\text{erg s}^{-1} \text{cm}^{-2}$) (8)	μ_e (AB mag arcsec $^{-2}$) (9)	Morphology (10)	Radial velocity (km s^{-1}) (11)
J0205-55:S1	ESO 153-G017	02 05 05.48	-55 06 42.54	17.60 ± 0.22	1.66	-21.95 ± 0.22	-12.01 ± 0.14	20.43 ± 0.02	SAB(rs)bc	6491
J0205-55:S2	ESO 153-IG016	02 04 50.78	-55 13 01.55	05.19 ± 0.00	2.26	-18.91 ± 0.00	-12.86 ± 0.04	21.12 ± 0.02	SB(s)cd pec	5942
J0205-55:S3	ESO 153-G015	02 04 34.92	-55 07 09.65	06.72 ± 0.02	1.92	-21.35 ± 0.02	-12.94 ± 0.70	18.94 ± 0.02	S0	
J0205-55:S4	ESO 153-G013	02 04 19.75	-55 13 50.44	11.25 ± 0.09	3.45	-21.39 ± 0.09	-12.61 ± 0.34	20.02 ± 0.02	Sa:	5942
J0205-55:S5	APMUKS	02 04 54.77	-55 08 31.99	05.84 ± 0.18	2.19	-17.13 ± 0.18	-14.45 ± 0.36	23.28 ± 0.02	[D]	6127
J0205-55:S6	APMUKS	02 04 57.07	-55 13 34.10	02.52 ± 0.06	1.56	-18.14 ± 0.06	-14.13 ± 0.36	20.38 ± 0.03	[D]	5760
J0205-55:S7	6dF	02 05 00.57	-55 15 19.63	01.87 ± 1.08	1.54	-15.65 ± 1.08	-14.35 ± 0.29	22.35 ± 0.35	[cD]	
J0205-55:S8	APMUKS	02 04 29.71	-55 12 56.09	02.61 ± 0.05	1.03	-17.44 ± 0.05	-14.69 ± 0.69	21.21 ± 0.02	[cD]	
J0205-55:S9*	APMUKS	02 05 23.76	-55 14 14.20	01.06 ± 0.21	-	-15.37 ± 0.12	-14.39 ± 0.46	18.78 ± 0.45	[cD]	
J0209-10:S1	NGC 0839	02 09 42.71	-10 11 01.36	11.93 ± 0.12	2.32	-21.00 ± 0.12	-12.11 ± 0.11	19.44 ± 0.02	Spec sp; LINER Sy2	
J0209-10:S2	NGC 0838	02 09 38.48	-10 08 45.79	07.97 ± 0.07	1.33	-21.16 ± 0.07	-11.38 ± 0.03	18.36 ± 0.02	SA(rs)0 ⁺ pec; Sbrst	
J0209-10:S3	NGC 0835	02 09 24.43	-10 08 10.59	16.04 ± 0.18	2.25	-21.47 ± 0.18	-12.68 ± 0.49	19.53 ± 0.03	R*)SA; pec; LINER	
J0209-10:S4	NGC 0833	02 09 20.69	-10 07 58.55	08.87 ± 0.01	1.73	-21.54 ± 0.01	-12.90 ± 0.12	18.63 ± 0.02	SAB(rs)bc HII	
J0258-74:S1	ESO 031-G005	02 58 06.48	-74 27 22.79	20.25 ± 0.26	2.81	-21.50 ± 0.26	-12.06 ± 0.09	20.47 ± 0.02	[S]	
J0258-74:S2	MRSS	02 58 52.43	-74 25 53.25	10.34 ± 0.29	1.22	-19.15 ± 0.29	-13.04 ± 0.08	21.66 ± 0.03	[S]	
J0258-74:S3	2MASX	02 58 42.76	-74 26 03.55	06.72 ± 0.56	3.40	-18.25 ± 0.56	-13.47 ± 0.12	21.70 ± 0.09	[S]	
J0258-74:S4	MRSS	02 57 29.23	-74 22 34.75	04.07 ± 0.85	1.31	-17.13 ± 0.85	-14.05 ± 0.33	21.80 ± 0.27	[dlrr]	
J0400-52:S1	ESO 156-G029	04 00 40.82	-52 44 02.71	06.80 ± 0.06	1.22	-21.32 ± 0.06	-14.67 ± 0.10	23.15 ± 0.02	SA(rs)cd pec:	
J0400-52:S2	APMUKS	04 00 48.07	-52 41 02.81	01.75 ± 0.02	1.44	-15.78 ± 0.02	-12.84 ± 0.20	20.11 ± 0.02	[S]	
J0400-52:S3	2MASX	04 00 06.03	-52 39 32.63	02.95 ± 0.01	1.64	-19.64 ± 0.01	-13.61 ± 0.20	20.18 ± 0.02	[S]	
J0400-52:S4	IC2028	04 01 18.23	-52 42 27.08	08.10 ± 0.01	1.47	-22.07 ± 0.01	-12.63 ± 0.31	19.57 ± 0.02	Scd:	
J0400-52:S5	2MASX	04 00 53.00	-52 49 38.43	09.41 ± 0.05	1.42	-21.98 ± 0.05	-12.65 ± 0.30	20.01 ± 0.02	(R)SB(s)b? pec	
J0400-52:S6	IC2029	04 01 17.84	-52 48 02.81	12.08 ± 0.06	1.80	-21.50 ± 0.06	-13.05 ± 0.42	21.13 ± 0.02	SB(s)c pec	
J0400-52:S7	APMUKS	04 01 08.99	-52 49 32.78	03.72 ± 0.13	1.59	-18.61 ± 0.13	-14.08 ± 0.23	21.81 ± 0.04	[D]	
J0400-52:S8*	-	04 01 17.00	-52 42 08.50	02.07 ± 0.35	-	-17.36 ± 0.08	-14.20 ± 0.52	16.46 ± 0.37	[D]	
J0400-52:S9*	-	04 01 19.29	-52 47 56.10	03.46 ± 1.38	-	-17.56 ± 0.07	-14.09 ± 0.57	15.15 ± 0.87	[D]	
J0443-05:S1	NGC 1643	04 43 43.90	-05 19 09.93	10.71 ± 0.21	1.19	-21.52 ± 0.21	-11.65 ± 0.04	19.05 ± 0.04	SB(rs)bc pec?	
J0443-05:S2	NGC 1645	04 44 06.43	-05 27 56.31	16.90 ± 0.15	1.99	-21.87 ± 0.15	-12.15 ± 0.20	19.62 ± 0.02	(R*)SB(rs)0+ pec	
J0443-05:S3	2MASX	04 44 11.67	-05 14 38.31	04.79 ± 0.19	1.86	-19.56 ± 0.19	-13.38 ± 0.25	19.53 ± 0.06	[S]	
J0443-05:S4	2MASX	04 44 05.54	-05 25 46.50	04.95 ± 0.12	1.60	-18.77 ± 0.12	-13.07 ± 0.06	20.46 ± 0.03	[D]	
J0443-05:S5*	SEGC	04 43 45.02	-05 19 41.90	01.97 ± 0.98	-	-17.65 ± 0.04	-13.47 ± 0.91	14.62 ± 1.09	S0+? pec	
J1026-19:S1	ESO 568-G011	10 26 40.81	-19 03 04.01	11.86 ± 0.19	1.28	-22.01 ± 0.19	-12.49 ± 0.35	20.12 ± 0.03	SAB(s)bc; pec Sbrst	
J1026-19:S2	2MASX	10 26 50.07	-19 04 31.77	05.46 ± 0.20	1.36	-20.16 ± 0.20	-13.04 ± 0.15	20.57 ± 0.05	Irr	
J1026-19:S3	-	10 26 18.93	-18 57 52.12	04.68 ± 0.27	1.45	-18.41 ± 0.27	-14.36 ± 0.54	22.16 ± 0.03	[D]	
J1026-19:S4	-	10 26 24.40	-19 02 02.99	02.19 ± 0.26	1.38	-17.62 ± 0.26	-14.26 ± 0.35	21.35 ± 0.11	[dlrr]	
J1026-19:S5	-	10 26 42.07	-19 07 35.07	05.56 ± 0.60	1.55	-16.87 ± 0.60	-14.67 ± 0.42	24.17 ± 0.04	[dlrr]	
J1026-19:S6	FLASH	10 26 25.21	-19 10 35.31	07.91 ± 0.07	1.10	-19.83 ± 0.07	-14.27 ± 1.67	21.75 ± 0.02	S0	
J1051-17:S1	2MASX	10 51 37.45	-17 07 29.23	27.62 ± 0.26	1.76	-21.01 ± 0.26	-12.62 ± 0.26	22.12 ± 0.02	(R?)PR(?)	5485
J1051-17:S2	NGC 3431	10 51 15.11	-17 00 29.44	14.72 ± 0.05	2.47	-21.25 ± 0.05	-12.40 ± 0.21	20.46 ± 0.02	SABb?	5302
J1051-17:S3	-	10 51 35.94	-16 59 16.80	06.61 ± 0.05	1.02	-17.91 ± 0.05	-13.72 ± 0.13	22.43 ± 0.02	[dS]	5988
J1051-17:S4	-	10 51 26.01	-17 05 03.61	03.48 ± 0.09	1.40	-16.19 ± 0.09	-14.51 ± 0.19	22.84 ± 0.02	[dlrr]	5485
J1051-17:S5	-	10 51 50.91	-16 58 31.64	03.58 ± 0.06	1.75	-17.02 ± 0.06	-14.35 ± 0.33	22.03 ± 0.02	[dlrr]	5485
J1051-17:S6	-	10 51 42.78	-17 06 34.59	02.11 ± 0.04	1.29	-16.78 ± 0.04	-14.18 ± 0.13	21.14 ± 0.02	[cD]	5668
J1051-17:S7	-	10 51 33.36	-17 08 36.63	04.18 ± 0.12	1.53	-16.77 ± 0.12	-14.28 ± 0.21	22.63 ± 0.02	[cD]	5394

Table 2 – continued

SINGG name HiPASS+	Optical ID	RA (h m s)	Dec. (d m s)	r_e (arcsec)	Axial ratio	M_R (AB mag)	$\log(F_{H\alpha})$ ($\text{erg s}^{-1} \text{cm}^{-2}$)	μ_e (AB mag arcsec $^{-2}$)	Morphology	Radial velocity [km s^{-1}]
(1)	(2)	(3)	(4)	(5)	(6)	(7)	(8)	(9)	(10)	(11)
J1051–17:S8*	–	10 51 25.92	–17 08 16.44	01.52 ± 0.67	–	–17.48 ± 0.04	–13.46 ± 0.88	15.44 ± 0.97	[dS]	5314
J1051–17:S9*	–	10 51 56.54	–17 05 03.50	00.34 ± 0.17	–	–16.68 ± 0.05	–13.78 ± 0.71	19.51 ± 1.09	[dE,N]	5606
J1059–09:S1	MCG-01-28-013	10 59 16.25	–09 47 38.16	15.08 ± 0.20	1.91	–22.26 ± 0.20	–12.12 ± 0.12	20.20 ± 0.03	SAB(rs)b pec:	
J1059–09:S2	GNX034	10 59 06.77	–09 45 04.38	11.72 ± 0.24	1.36	–19.80 ± 0.24	–12.91 ± 0.05	22.51 ± 0.02	[lrr]	
J1059–09:S3	MCG-01-28-012	10 59 15.61	–09 48 59.41	14.66 ± 0.37	3.13	–20.84 ± 0.37	–12.51 ± 0.06	21.82 ± 0.03	Sab pec sp	
J1059–09:S4	MRK1273	10 58 46.84	–09 50 43.31	08.79 ± 0.15	1.32	–21.53 ± 0.15	–12.48 ± 0.12	19.91 ± 0.03	SB0-a Sbrst	
J1059–09:S5	GNX066	10 59 30.98	–09 44 25.26	09.11 ± 0.13	2.84	–19.57 ± 0.13	–13.15 ± 0.08	22.21 ± 0.02	[S]	
J1059–09:S6	–	10 59 08.46	–09 43 14.49	08.04 ± 0.16	1.69	–19.00 ± 0.16	–13.54 ± 0.12	22.56 ± 0.02	[lrr]	
J1059–09:S7	–	10 59 21.31	–09 47 50.49	02.50 ± 0.15	1.59	–18.83 ± 0.15	–13.47 ± 0.08	20.21 ± 0.06	[cD]	
J1059–09:S8	–	10 59 01.73	–09 52 46.76	03.46 ± 0.40	1.81	–16.81 ± 0.40	–14.91 ± 0.41	23.07 ± 0.10	[D]	
J1059–09:S9*	–	10 58 44.69	–09 53 28.60	00.59 ± 0.29	–	–13.56 ± 0.10	–14.38 ± 0.43	19.58 ± 1.09	[dlrr]	
J1059–09:S10*	2MASX	10 59 02.64	–09 53 19.90	00.37 ± 0.07	–	–17.03 ± 0.02	–16.16 ± 0.44	17.13 ± 0.44	[dS]	
J1159–19:S1	NGC 4027	11 59 30.13	–19 15 54.88	34.37 ± 0.13	1.07	–21.24 ± 0.13	–10.97 ± 0.04	19.71 ± 0.02	SB(s)dm HII	
J1159–19:S2	NGC 4027A	11 59 29.34	–19 19 59.52	16.26 ± 0.10	1.40	–17.83 ± 0.10	–12.83 ± 0.06	21.86 ± 0.02	IB(s)m:	
J1159–19:S3	–	11 59 35.79	–19 19 02.99	03.80 ± 0.29	1.00	–15.18 ± 0.29	–14.21 ± 0.28	21.48 ± 0.06	[D]	
J1159–19:S4	ISZ108A	11 59 37.88	–19 19 45.80	06.18 ± 0.36	1.34	–15.77 ± 0.36	–14.04 ± 0.23	21.91 ± 0.05	[D]	
J1250–20:S1	ESO 575–G006	12 50 52.84	–20 22 15.65	09.95 ± 0.13	1.38	–21.85 ± 0.13	–12.17 ± 0.10	19.58 ± 0.03	SA(s)bc pec H II	
J1250–20:S2	ESO 575–G004	12 50 40.91	–20 20 06.22	10.09 ± 0.04	1.37	–21.44 ± 0.04	–12.44 ± 0.11	20.09 ± 0.02	S	
J1250–20:S3 ^a	ESO-LV5750061	12 50 49.77	–20 22 03.44	04.25 ± 0.14	1.54	–18.57 ± 0.14	–13.36 ± 0.07	21.43 ± 0.04	[lrr]	
J1250–20:S4	–	12 50 39.92	–20 20 52.87	05.93 ± 0.11	1.59	–18.72 ± 0.11	–13.95 ± 0.20	21.98 ± 0.03	[lrrs]	
J1250–20:S5	–	12 50 59.16	–20 28 14.80	02.66 ± 0.27	2.04	–17.43 ± 0.27	–13.84 ± 0.15	21.64 ± 0.10	[cD]	
J1250–20:S6*	–	12 50 45.87	–20 23 30.10	01.54 ± 0.51	–	–15.38 ± 0.15	–14.39 ± 0.43	18.42 ± 0.74	[D]	
J1250–20:S7*	–	12 50 46.92	–20 23 12.40	01.28 ± 0.51	–	–14.16 ± 0.27	–14.83 ± 0.25	20.04 ± 0.91	[D]	
J1403–06:S1	NGC 5426	14 03 24.88	–06 04 09.14	29.64 ± 0.35	1.99	–21.18 ± 0.35	–11.38 ± 0.03	20.57 ± 0.02	SA(s)c pec	2512
J1403–06:S2	NGC 5427	14 03 26.09	–06 01 51.20	36.45 ± 0.09	1.30	–22.01 ± 0.09	–11.11 ± 0.04	20.05 ± 0.02	SA(s)c pec:Sy2 HII	2741
J1403–06:S3	APMUKS	14 03 13.48	–06 06 24.17	04.18 ± 0.85	1.03	–15.27 ± 0.85	–14.40 ± 0.26	22.70 ± 0.17	[cD]	2767
J1403–06:S4	APMUKS	14 03 34.62	–06 07 59.27	05.96 ± 0.86	1.43	–14.42 ± 0.86	–14.85 ± 0.34	24.34 ± 0.02	[cD]	2685
J1408–21:S1	ESO 578–G026	14 08 42.04	–21 35 49.82	10.24 ± 0.26	1.47	–22.35 ± 0.26	–12.24 ± 0.07	19.22 ± 0.05	SB(r)bc	8704
J1408–21:S2	2MASX	14 08 57.72	–21 38 52.47	07.99 ± 0.06	1.39	–21.11 ± 0.06	–12.67 ± 0.04	20.15 ± 0.02	[S]	8831
J1408–21:S3	2MASX	14 08 41.04	–21 37 40.97	06.06 ± 0.10	1.60	–20.26 ± 0.10	–13.19 ± 0.07	20.52 ± 0.03	[S0]	8792
J1408–21:S4	2MASX	14 08 33.28	–21 36 07.18	09.21 ± 0.58	1.18	–20.72 ± 0.58	–13.35 ± 0.12	20.92 ± 0.02	[S0]	9137
J1408–21:S5*	–	14 08 39.82	–21 38 14.30	00.58 ± 0.58	–	–13.31 ± 0.52	–15.16 ± 0.06	22.89 ± 2.24	[cD]	8788
J1408–21:S6*	–	14 08 52.84	–21 42 07.20	01.73 ± 0.58	–	–17.12 ± 0.07	–14.30 ± 0.48	16.70 ± 0.73	[dS]	8682
J1956–50:S1	IC4909	19 56 45.51	–50 03 20.29	15.70 ± 0.19	2.42	–21.68 ± 0.19	–12.38 ± 0.16	20.70 ± 0.03	SA:(rs)bc	7634
J1956–50:S2	2MASX	19 55 53.21	–50 02 10.82	08.03 ± 0.11	1.29	–20.32 ± 0.11	–12.69 ± 0.08	20.81 ± 0.02	[S/lrr]	7039
J1956–50:S3	–	19 56 08.20	–50 02 21.56	01.72 ± 0.22	1.01	–16.49 ± 0.22	–13.67 ± 0.05	21.59 ± 0.11	[BCD]	6400
J1956–50:S4*	–	19 55 45.92	–50 06 15.50	01.74 ± 0.74	–	–15.15 ± 0.23	–14.60 ± 0.10	19.23 ± 0.96	[cD]	7497
J2027–51:S1	ESO 234–G032	20 28 06.39	–51 41 29.83	12.49 ± 0.29	1.89	–21.15 ± 0.29	–12.03 ± 0.06	20.34 ± 0.03	(R')SB(s)bc	5805
J2027–51:S2	ESO 234–G028	20 27 31.97	–51 39 20.81	16.13 ± 0.17	1.66	–21.31 ± 0.17	–12.13 ± 0.08	20.71 ± 0.02	SA(s)bc pec	5805
J2027–51:S3	MRSS	20 27 48.52	–51 44 19.35	05.57 ± 0.12	1.59	–18.93 ± 0.12	–13.20 ± 0.11	21.07 ± 0.03	[dlrr]	5805

Table 2 – continued

SINGG name HiPASS+	Optical ID (2)	RA (h m s) (3)	Dec. (d m s) (4)	r_c (arcsec) (5)	Axial ratio (6)	M_R (AB mag) (7)	$\log(F_{H\alpha})$ ($\text{erg s}^{-1} \text{cm}^{-2}$) (8)	μ_e (AB mag arcsec $^{-2}$) (9)	Morphology (10)	Radial velocity (km s^{-1}) (11)
J2027–51:54	–	20 27 54.64	–51 38 04.52	02.05 ± 0.15	1.15	–17.20 ± 0.15	–13.71 ± 0.14	20.74 ± 0.04	[cD]	5988
J2318–42a:S1	NGC 7582	23 18 23.44	–42 22 11.94	51.63 ± 0.26	1.98	–21.60 ± 0.26	–11.02 ± 0.07	20.04 ± 0.02	(R')SB(s)ab Sy2	1436
J2318–42a:S2	NGC 7590	23 18 54.78	–42 14 18.94	26.70 ± 0.05	2.15	–20.71 ± 0.05	–11.12 ± 0.03	19.64 ± 0.02	S(r')bc Sy2	1457
J2318–42a:S3 ^b	NGC 7599	23 19 21.14	–42 15 24.6	38.99 ± 0.29	2.03	–19.76 ± 0.29	–11.87 ± 0.06	21.53 ± 0.02	SB(s)c	1753
J2318–42a:S4*	APMUKS	23 18 50.44	–42 23 50.30	00.49 ± 0.41	–	–11.45 ± 0.17	–14.77 ± 0.27	20.72 ± 1.82	[LSBD]	1661

Notes. Columns. (1) Name assigned in SINGG (HiPASS name with ;Sn appended for n th source). (2) Previously assigned ID based on position match with NASA/IPAC Extragalactic Database (NED); <http://ned.ipac.caltech.edu/>. (3) Right Ascension (J2000). (4) Declination (J2000). (5) R -band effective radius. (6) Ratio of major and minor axes. (7) R -band absolute magnitude. (8) Logarithm of total $H\alpha$ flux, corrected for Galactic extinction and [N II] contamination. (9) R -band effective surface brightness, face-on and extinction-corrected (Galactic and internal). (10) NED morphological classification where available, or [new classification]. (11) Central radial velocity from our ANU2.3mT/WiFeS data (Sweet et al., in preparation). Sources marked with * have been identified since SINGG release 1; for these we give preliminary measurements performed using IRAF's APPHOT task. IRAF is distributed by the National Optical Astronomy Observatories, which are operated by the Association of Universities for Research in Astronomy, Inc., under cooperative agreement with the National Science Foundation (Tody 1993).

^aOur declination for J1250–20:S3 is 10 arcsec different from the ESO measurement, suggesting a problem with their search radius for this object.

^bOnly half of J2318–42a is within our FOV, so we use the NED position for J2318–42a:S3.

3 DISCUSSION

All the galaxies in SINGG have (by design) $H I$ and all are detected in $H\alpha$, indicating that $H I$ -rich, non-star-forming galaxies are rare (Meurer et al. 2006). Fields observed for SINGG usually contain single ELGs, with some doubles and triples, and more rarely four or more galaxies in a single pointing (our Choir groups). We use the entire SINGG data set as our control sample against which we compare the Choir galaxies. In this section, we discuss selection biases, analyse the Choir member galaxies in terms of size, EW, luminosity and surface brightness, and then focus on the Choir groups' morphology, size, SFR and efficiency, and $H I$ deficiency.

3.1 Selection biases

Although SINGG overcomes biases that are prevalent in optically selected surveys, some selection effects are still present. The two major selection effects are (1) a selection of more massive sources and (2) a bias towards more distant groups.

First, the SINGG sample is selected from HiPASS so that the nearest sources at each $H I$ mass are preferentially chosen; combined with the HiPASS $H I$ detection limit this means that distant, isolated, low-mass $H I$ sources are not selected (see Fig. 1). This is therefore also a selection effect for Choir groups. The detection limits are discussed in detail by Zwaan et al. (2004). At higher redshift (distance $\gtrsim 30$ Mpc) only the most massive $H I$ sources are detected by HiPASS. These sources are so rare that we cannot find many of these except by looking at these distances. Hence, most of the high-mass $M_{H I} > 10^{10} M_{\odot}$ sources selected for SINGG have $D > 30$ Mpc. SINGG can detect galaxies optically to fairly low stellar masses out to the full ~ 150 Mpc distance limit of HiPASS. While the $H I$ mass detection limit precludes us from detecting isolated dwarf galaxies at distances greater than about 30 Mpc, we can detect them at these distances when they are part of a more massive $H I$ system. We illustrate this in Fig. 1. Choir groups (blue stars), SINGG doubles and triples (grey triangles) and SINGG singles (light grey circles) all show an increase in $H I$ mass with distance.

In order to show the likely contribution of the individual galaxies within the Choirs to the system $H I$ mass, we bring some basic correlations seen within SINGG to bear. Following Meurer et al. (2006) we define the gas cycling time $t_{\text{gas}} [\text{yr}] = 2.3 M_{H I} / \text{SFR}$, where $M_{H I}$ is the $H I$ mass and the factor of 2.3 is a correction for molecular hydrogen and helium content. We then adopt the Meurer et al. (2009) conversion of star formation rate $\text{SFR} [M_{\odot} \text{yr}^{-1}] = L_{H\alpha} / (1.5 \times 1.04 \times 10^{41})$, where $L_{H\alpha}$ is the $H\alpha$ luminosity in erg s^{-1} . The factor of 1.5 converts the Salpeter (1955) IMF measurements of SINGG to a Chabrier (2003) profile (Brinchmann et al. 2004; Meurer et al. 2009). In Fig. 2, we plot t_{gas} as a function of the R -band effective surface brightness μ_e , with the best fit

$$\log(t_{\text{gas}}) = (4.14 \pm 0.48) + (0.29 \pm 0.02)\mu_e. \quad (1)$$

This allows us to estimate $M_{H I}$ from $L_{H\alpha}$ and μ_e as follows:

$$\log(M_{H I}) = \log(L_{H\alpha}) + (0.29 \pm 0.02)\mu_e - (37.42 \pm 0.48). \quad (2)$$

The significance of this relation will be discussed in the context of SINGG in a future paper.

We use this relation to predict the $H I$ mass of individual Choir member galaxies, shown as red diamonds in Fig. 1. If the galaxies were isolated, only the brightest galaxies in each Choir group could be detected in $H I$ by Parkes. The smaller members of the Choir

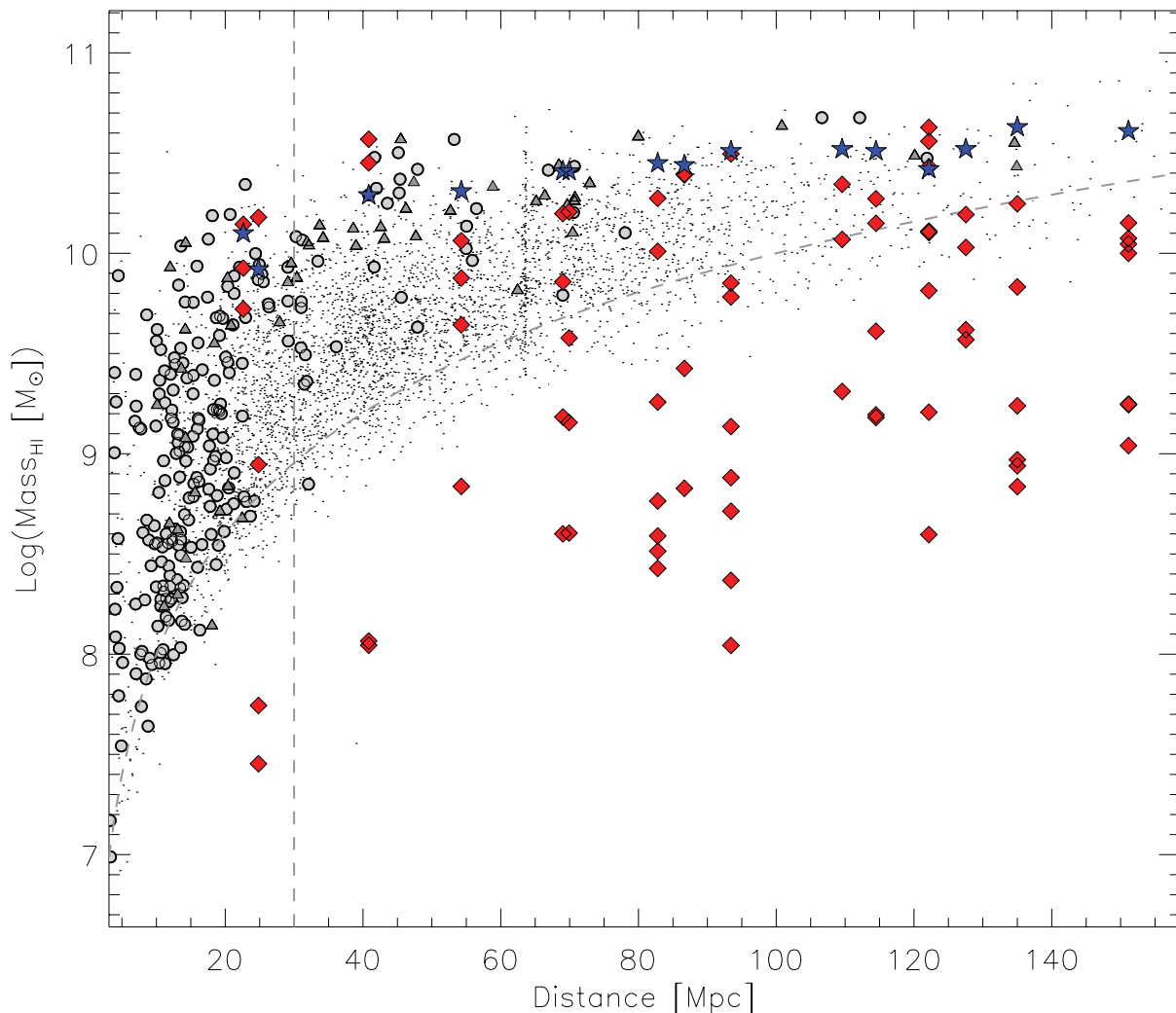


Figure 1. Total H I mass versus distance for SINGG detections compared to HiPASS. The blue stars denote Choir groups, mid-grey triangles denote doubles and triples, and mid-grey filled circles denote single galaxies in SINGG. The black points indicate HiPASS detections not in SINGG. The vertical, dashed line at 30 Mpc represents the field-of-view limit for detecting an average Choir group. See the text for explanation. The curved, dashed line represents the 3σ detection limit in HiPASS as described in Zwaan et al. (2004) and Meurer et al. (2006), from a fake source analysis and integrating over all line widths from 20 to 650 km s⁻¹. Choirs are at the high- $M_{\text{H I}}$ and large-distance end of the distribution. Estimated H I mass for Choir member galaxies is shown as red diamonds. See the text for calculation. Above the nominal group detection limit of 30 Mpc, only the brightest members of each group are detectable at the 3σ limit if isolated: the Choir dwarfs are only detected due to their inclusion in an H I-rich group.

groups could not be detected, and are only included in SINGG due to their inclusion in an H I-rich group. The groups at 40 and 120 Mpc, HiPASS J1403–06 and J1059–09, each have a total *observed* H I mass less than the *predicted* H I mass of their two to three brightest members. This means that these groups are both deficient in H I compared with the amount expected based on the H α luminosity and R -band surface brightness of their group members. See Section 3.7 for a discussion of H I deficiency.

The second selection effect is a bias towards more distant groups; there are fewer Choir groups and fewer members per group detected at small distances. This is because the large angular size of nearby groups is more likely to exceed our 15 arcmin field of view. A single pointing will then contain fewer than all of the members in a group, leading to underrepresentation of the number of galaxies identified as group members. (We note previously detected giants that are likely to be associated with our Choir groups in Appendix A.) Also, if a pointing contains less than four objects (the threshold for defining a Choir), a group will not be de-

tected, leading to underrepresentation of number of groups at small distances.

For a Choir group to be detected, it must have at least four ELGs within the field of view. We characterize group size by measuring the projected distance between the two most luminous galaxies in each group. (See Section 3.5.) Our mean Choir group size is 190 kpc, which will fit inside a single pointing as near as ~ 30 Mpc. Therefore, we do not expect to see any groups of this average size nearer than 30 Mpc (represented by the vertical dashed line in Fig. 1). This corresponds closely with our observations; although there are two groups below this cut, one is very compact (HiPASS J1159–19) and the other barely makes the Choir definition with one member nearly outside of our field of view (HiPASS J2318–42a).

It is important to note that many of the nearby SINGG galaxies are likely to be in groups where only three or fewer galaxies fit within the SINGG field of view. We estimate the fraction of SINGG that is in groups similar to the Choirs by measuring the proportion

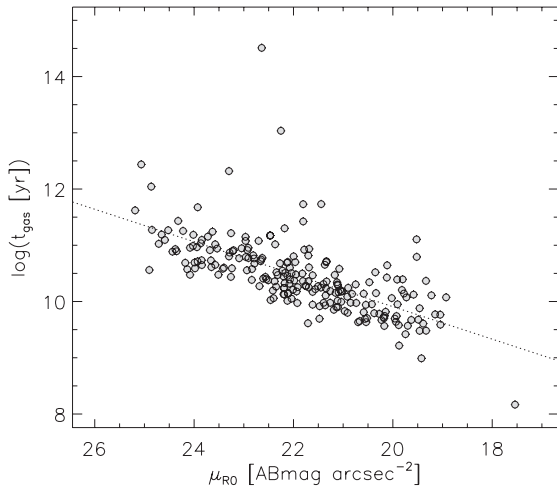


Figure 2. Parametrization of gas cycling time as a function of the R -band effective surface brightness for single galaxies in SINGG.

of Choir groups compared with all SINGG detections at distances greater than 30 Mpc. In this manner, we calculate that 20 percent of SINGG detections are in fact in galaxy groups. Considering that Choir groups are still likely to be underrepresented at the near end of this distance range, the true fraction may be significantly higher. The proportion of groups increases with distance. According to Tully (1987), around 50 percent of galaxies are expected to be in groups of four or more members.

These two selection effects mean that Choirs are among the most distant and $H\text{I}$ massive of the HiPASS sources. Fig. 3 illustrates

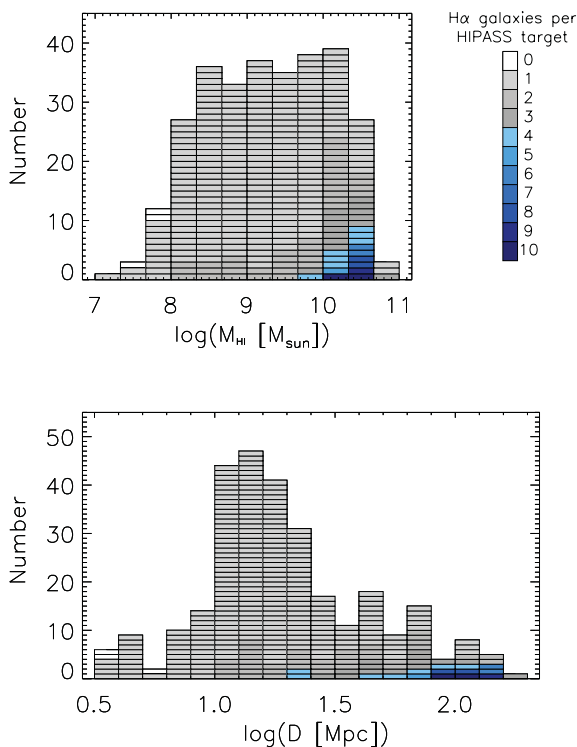


Figure 3. $H\text{I}$ mass histogram and distance histogram of SINGG detections. The blue colour regions correspond to Choir groups; the darker colour regions correspond to more members (see key). These histograms are nested, so that the entire area covers the whole SINGG sample. Choirs are at the high- $M_{H\text{I}}$ and large-distance end of the distribution.

the distribution of groups in both $H\text{I}$ mass and distance. While the SINGG control sample has (by design) a relatively flat distribution in the range $8 < \log(M_{H\text{I}}) < 10.6$, the number of Choir groups peaks at the high-mass end of this range. These differences must be taken into account when comparing Choirs with the control SINGG sample for distance-dependent and mass-dependent quantities.

In the following subsections, we continue this discussion with an analysis of the properties of the Choir member galaxies.

3.2 Size and EW

The histogram of R -band effective (half-light) radius, $r_e(R)$ for Choir member galaxies, in comparison to other single and multiple SINGG galaxies, is shown in Fig. 4. A Kolmogorov–Smirnov (KS) test shows that Choir members are not significantly different from the single detections in SINGG with a fractional probability that they were drawn from the same parent sample of $p = 0.35$. A similar result occurs for the $H\alpha$ effective radius, radius enclosing 90 percent of R -band flux and radius enclosing 90 percent of $H\alpha$ flux. Figures demonstrating this are not shown for the sake of brevity. Applying a magnitude cut at $M_R > -21$ to exclude the most luminous galaxies does not alter the result; lower luminosity Choir galaxies are also not significantly different from their SINGG counterparts.

Fig. 5 is a histogram of $H\alpha$ EW (measured within the $H\alpha$ effective radius and corrected for dust absorption). Choir members do not have high EWs when compared with the SINGG control sample ($p = 0.54$). The same result is seen for lower luminosity galaxies ($M_R > -21$).

Naively, one might expect the distance-dependent detection limit in $H\text{I}$ mass, together with the fact that Choirs are at further distances, to cause a dependence of radius and EW on distance as well. However, as discussed above, Choir dwarfs are included in the SINGG field of view only because of their proximity to $H\text{I}$ -detectable giants. We have used the Choir groups to identify star-forming dwarfs at such large distances that they are not detectable in HiPASS, but

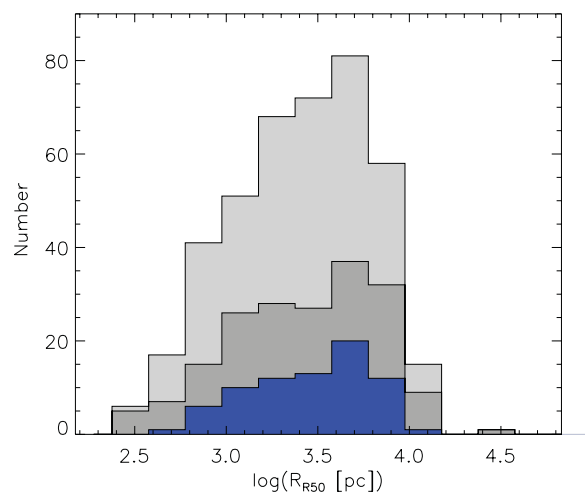


Figure 4. Histogram of R -band half-light radius of ELGs in SINGG. The blue, mid-grey and light grey denote Choir member galaxies, SINGG doubles and triples, SINGG single galaxies, respectively. Choir members are not significantly different from the control SINGG sample ($p = 0.35$). This is similar for $H\alpha$ half-light radius, R -band radius enclosing 90 percent of flux and $H\alpha$ radius enclosing 90 percent of flux. The same is seen when $R > -21$ to compare only dwarf galaxies.

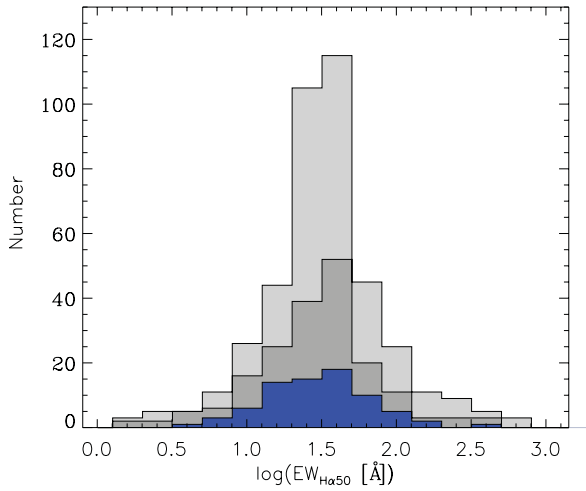


Figure 5. H α EW calculated within the effective radius and corrected for dust. The blue, mid-grey and light grey denote Choir member galaxies, SINGG doubles and triples, SINGG single galaxies, respectively. Choir members do not have high EW for their size ($p = 0.54$). The same is seen when $R > -21$ to compare only dwarf galaxies.

their optical properties are the same as nearby star-forming dwarfs detected in HiPASS.

3.3 Luminosity and surface brightness

In Figs 6 and 7 we plot luminosity–surface brightness and luminosity–radius correlations. Choir galaxies have on average 0.5 dex higher surface brightness and 0.05 dex smaller radius for their luminosities than the control sample. We perform a KS test on the distribution of $\{y - (a + bx)\}$, where y is the surface brightness or radius and x is the R -band magnitude of the Choir galaxies, and a and b are parameters from the fit to single galaxies in SINGG. We find that the offsets are not significant, with p -values of 0.06 and 0.27, respectively.

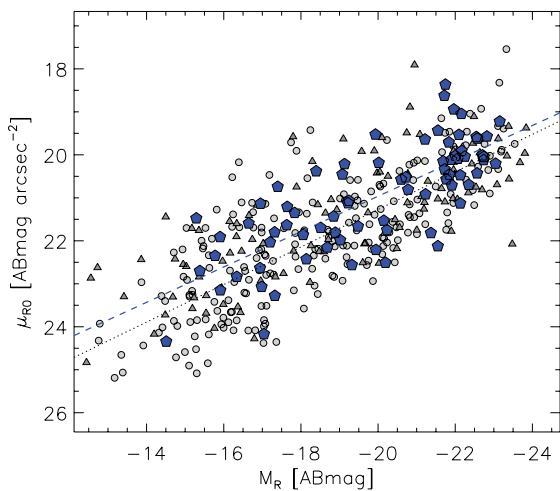


Figure 6. Surface brightness in the R band as a function of absolute magnitude. The blue pentagons denote Choir member galaxies, mid-grey triangles denote doubles and triples, and mid-grey filled circles denote single galaxies in SINGG. The blue, dashed line represents a linear fit to Choir members and the dotted line is for single galaxies in SINGG. The small offset is not significant ($p = 0.06$).

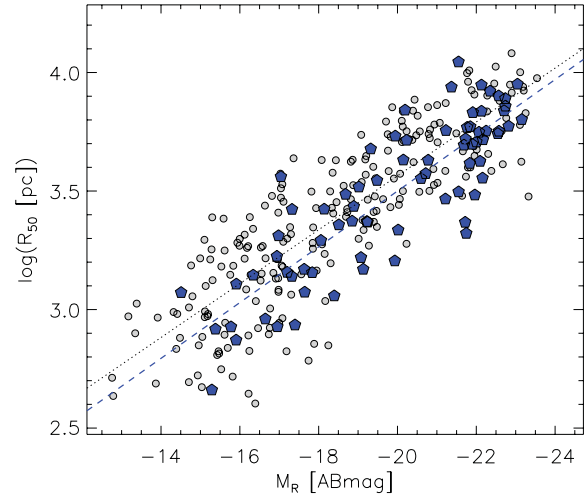


Figure 7. R -band half-light radius as a function of absolute magnitude. The blue pentagons denote Choir member galaxies, mid-grey triangles denote doubles and triples, and mid-grey filled circles denote single galaxies in SINGG. The blue, dashed line shows a linear fit to Choir members and the dotted line is for single galaxies in SINGG. The small offset is not significant ($p = 0.27$).

3.4 Group morphology

The Choir groups by definition have four or more H α -emitting galaxies, without further restriction on morphology or relative size. An interesting subset (eight out of fifteen groups) is groups that are comprised of two large spirals and two to eight smaller galaxies. We illustrate this in Fig. 8, where we show R -band absolute magnitude of Choir members relative to the brightest member in each group. The peak at -0.25 mag represents the second largest giant, and the extended tail peaking at -2.25 mag represents dwarf companions. We note that M_r magnitudes for the Milky Way (MW), M31, Large

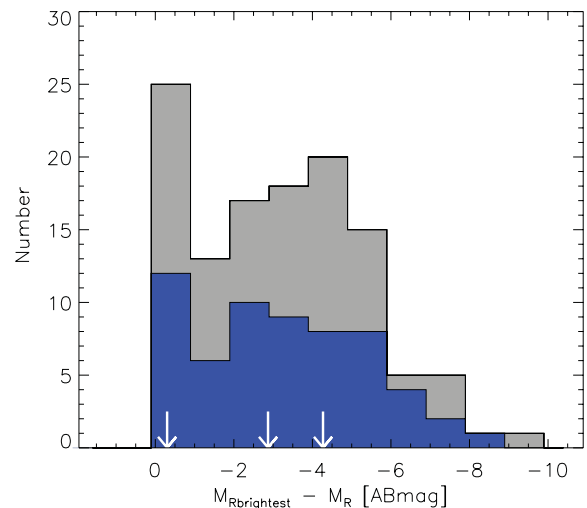


Figure 8. Distribution of relative luminosities of group galaxies compared to the most luminous in each group. The blue area denotes Choir member galaxies, and mid-grey denotes doubles and triples in SINGG. Single galaxies in SINGG are not shown, as there are no fainter companions in these fields. The first peak indicates when there are two large galaxies in a group and the second broader peak shows the dwarf members. The white arrows denote the position of LG members relative to M31 (left to right: MW, LMC, SMC). Qualitatively, our groups have a similar distribution of relative R -band magnitude to our LG.

552 *S. M. Sweet et al.*

Magellanic Cloud (LMC) and Small Magellanic Cloud (SMC) are -21.17 , -21.47 , -18.60 and -17.20 , respectively (Robotham et al. 2012), so that the Local Group (LG) will appear on this plot at the white arrows. In terms of luminosity the Choir groups therefore appear to be possible LG analogues, as discussed by Pisano et al. (2011) and Robotham et al. (2012). Our selection method seems to be good at finding LG analogues (at least in terms of *magnitude* and *morphology*), with an approximate strike rate of 50 per cent. We suggest that perhaps these types of groups are more common than previously thought, but usually the dwarf galaxies fall below the relevant detection limit so the group appears as a pair of bright spirals. In SINGG however, star-forming dwarf galaxies are readily apparent in the $H\alpha$ imaging.

In Appendix A, we point out some morphological features of each Choir group and search larger photographic survey images to check for possible group members outside of our imaging. Interestingly, there are no *bright* ellipticals in the SINGG imaging, and the few nearby giant ellipticals do not appear to be associated with the HiPASS detections. This is in contrast with optically and X-ray-selected groups where the elliptical fraction is 0.4–0.5 (Mulchaey 2000). The discrepancy is probably a consequence of the $H\text{I}$ selection in HiPASS being biased towards younger, $H\text{I}$ -rich groups with fewer ellipticals.

3.5 Group compactness

In this section we compare the size of our Choir groups to Hickson Compact Groups (HCGs; Hickson, Kindl & Auman 1989) and groups in the Garcia (1993) catalogue. These three catalogues all contain groups of four or more members, but have different limiting magnitudes and distance ranges, and different group-finding algorithms.

Ideally, galaxy group size is measured by the virial radius defined as the radius enclosing a luminosity brighter than a specified magnitude (e.g. Tully 1987; Garcia 1993, 1995). This measurement requires radial velocity data, which do not yet exist for most of our Choir group members. It also assumes a relaxed group with a Gaussian distribution of velocities, but our Choir groups are not relaxed and do not have a sufficient number of members to display a Gaussian distribution. We are limited by having only a few members, particularly in the majority of cases where there are only two bright spirals and a number of faint dwarfs. While it may appear possible to use the projected distance between two closest neighbours in the group to compare our groups to other samples, this statistic should only be used to compare catalogues that have consistent limiting magnitudes, which is not the case for Choirs, HCGs and Garcia groups. We therefore use the projected distance between the two *most luminous* galaxies in each group as a measurement of ‘group compactness’. This parameter is not as physical as previously mentioned measurements of group size, but simply allows us to put our groups in context with existing catalogues given the available data. We emphasize that our comparison is not strict because the catalogues are based on different algorithms.

For each of the three catalogues we calculate the compactness parameter and show histograms for the different catalogues in Fig. 9. Mean group compactnesses for Choir groups, Hickson groups and Garcia groups are 190 ± 31 , 87 ± 8 and 961 ± 52 kpc, respectively. The distributions are significantly different; a KS test yields $p < 0.001$ that Choir groups and Garcia groups belong to the same population, and $p < 0.001$ that Choir groups and Hickson groups belong to the same population. Of course, Choir group sizes are limited by the field of view of the CTIO images, causing our distribution to be

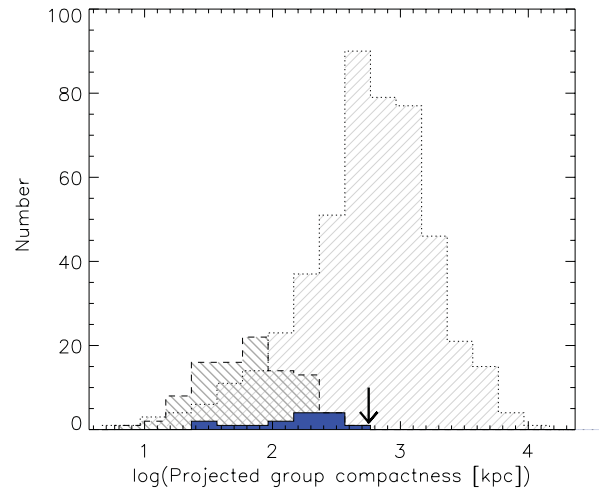


Figure 9. Choir group compactness, estimated by measuring separation between two brightest galaxies in a group. The solid, blue histogram shows our Choir groups; light grey SW–NE cross-hatching with dotted outline denotes Garcia groups; medium grey NW–SE cross-hatching with dashed outline shows Hickson groups. Our groups are more compact than Garcia groups, but not as compact as Hickson groups. The black arrow indicates the compactness of our LG, which is more than 3σ from the mean Choir group compactness.

skewed in favour of smaller groups; at our mean distance of 87 Mpc the maximum size of our groups is only 380 kpc.

For the LG this group compactness statistic is 800 kpc in 3D space. Using the typical $\sqrt{2}$ conversion factor, this corresponds to 565 kpc in 2D space. This is just over 3σ larger than our mean Choir group compactness. In terms of physical separation then, we note that Choirs appear to be a compressed version of the LG, and may represent a later stage of evolution of a system like M31 and the MW with their retinue of dwarfs.

A more sophisticated analysis that includes radial velocity measurements for a stricter definition has recently been conducted for the Galaxy And Mass Assembly sample (Robotham et al. 2012), with the result that LG analogues are rare in that sample. We plan to conduct a similar analysis of the frequency of LG analogues in SINGG.

3.6 Star formation

In Figs 10 and 11 we plot specific star formation rate (sSFR) and total (group) star formation efficiency (SFE_T) as a function of stellar mass M_* , where $\text{sSFR} = \text{SFR}/M_*$ and $\text{SFE}_T = \text{SFR}_T/M_{\text{H I, T}}$. The subscript ‘T’ denotes total quantities for each group. Stellar masses are estimated using the Bell et al. (2003) conversion $\log(M_*/L_g) = -2.61 + 0.298 \log(M_* h^2/M_\odot)$, with $M_{R\odot} = 4.61$, $M_{g\odot} = 5.45$ and $(g-r) = 0.5$ mag for late-type galaxies (Blanton et al. 2003). This gives $\log(M_*) = -3.66 + 1.425 \log L_R$. We note that West et al. (2009) found the Bell et al. (2003) conversion to be biased by emission lines within the Sloan Digital Sky Survey (SDSS; Abazajian et al. 2003) broad-band filters, particularly for the bluest galaxies. However, the EWs in our sample are low (Fig. 5) compared with the $\sim 1000 \text{ \AA}$ R -band filter, so the corrections are small and the conversion is adequate for our purposes.

In terms of both sSFR and group SFE_T , Choir galaxies fall neatly on the best fits to the control SINGG sample, with KS p -values

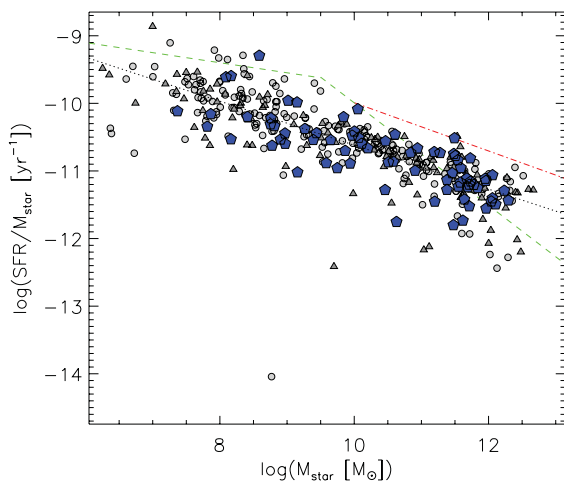


Figure 10. sSFR as a function of stellar mass for individual galaxies in SINGG. The blue pentagons denote Choir member galaxies, mid-grey triangles denote doubles and triples, and mid-grey filled circles denote single galaxies in SINGG. The black, dotted line corresponds to the best fit to single galaxies in SINGG. The red, dot–dashed line corresponds to the best fit to high-sSFR galaxies in Schiminovich et al. (2010). The green, dashed line corresponds to the Huang et al. (2012) relation. Choir galaxies lie on the relation defined by the control SINGG sample ($p = 0.37$). The SINGG sample exhibits a lower sSFR than the Schiminovich sample across all stellar masses ($p < 0.001$). The high-stellar-mass Huang relation is better matched to the SINGG sample but displays a much steeper slope.

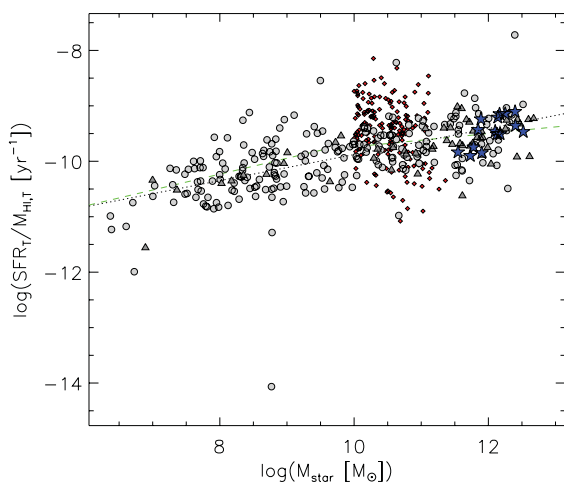


Figure 11. Total SFE as a function of total stellar mass for groups in SINGG. The blue stars denote Choir groups, mid-grey triangles denote doubles and triples, and mid-grey filled circles denote single galaxies in SINGG. The black, dotted line is for single galaxies in SINGG. The small, red diamonds denote the high-sSFR galaxies in Schiminovich et al. (2010). The green, dashed line shows the ridge line of the Huang et al. (2012) sample. Choir groups lie on the relation defined by the control SINGG sample ($p = 0.14$). The SINGG sample has a lower SFE than the high-sSFR Schiminovich sample within the corresponding stellar mass range ($p < 0.001$).

of 0.37 and 0.14, respectively.² This seems in contrast to previous findings that star formation is suppressed at group densities (Lewis

² In this section, we perform the KS test on the distribution of $\{y - (a + bx)\}$, where y is the sSFR or SFE, x is the stellar mass of the Choir (SINGG) galaxies, and a and b are parameters from the fit to single galaxies in SINGG [galaxies in Schiminovich et al. (2010)]. For the SINGG–Schiminovich

et al. 2002; Gómez et al. 2003). However, our selection is different in that typical group catalogues have at least four similarly large galaxies, and are insensitive to the dwarf members. Moreover, our control sample does not consist solely of isolated galaxies; as discussed earlier, at least 20 per cent of the sample detections are likely to be in similarly dense groups of four or more member galaxies.

We therefore compare the star formation activity for our control sample to the work by Schiminovich et al. (2010, *GALEX* Arecibo SDSS Survey, GASS) and Huang et al. (2012, Arecibo Legacy Fast ALFA (ALFALFA) survey with SDSS and *GALEX* photometry).

First, our control sample exhibits a lower sSFR (by ~ 1 dex across the corresponding stellar mass range) than the high-sSFR trend of Schiminovich et al. (2010), with a KS test p -value < 0.001 . This agrees with our suggestion that many of the galaxies in SINGG are not field galaxies but instead exist in Choir-like groups. Our SINGG sample is more consistent with the ($M_* > 9.5$) sSFR trend in Huang et al. (2012), although their sample shows a much steeper slope than ours. The SINGG data also hint at a transition to lower sSFR above a turnover stellar mass as seen in Bothwell, Kennicutt & Lee (2009), but not convincingly so.

Next, our SFE_T plot (Fig. 11) is for groups, not for individual galaxies, but according to Rownd & Young (1999) there should be no variation in SFE with environment. On this basis we compare our SFE data in Fig. 11 to Schiminovich et al. (2010) and Huang et al. (2012). Our SFE for all of SINGG is lower than the high-sSFR ($\log SFR/M_{\text{star}} > -11.5$) Schiminovich et al. (2010) data within the corresponding stellar mass range, with a KS test p -value < 0.001 . Our sample shows an increase in SFE with stellar mass, in contrast with the Schiminovich et al. (2010) data, which do not seem to show any trend. We note that SINGG covers a much wider stellar mass range than the Schiminovich et al. (2010) sample, which may make the small trend more apparent in our work. Our results are more consistent with Bothwell et al. (2009), who found that gas cycling time ($\propto SFE^{-1}$) decreases shallowly with luminosity (that is, SFE increases slowly with luminosity) for H I-selected galaxies. Similarly, the SFE work by Huang et al. (2012) is also consistent with our SINGG sample.

We consider the source of discrepancy between our results and those of Schiminovich et al. (2010) and Huang et al. (2012). Neither we nor Schiminovich et al. (2010) correct for helium content when calculating sSFR or SFE but both correct for dust absorption. Both assume a Chabrier (2003) IMF. We point out that our SFRs are calculated from H α emission, while the Schiminovich et al. (2010) SFRs are calculated from UV measurements. These indicators for star formation are sensitive to different types of stars; H α probes the formation of the most massive stars ($M_* > 20 M_\odot$) which have lifetimes < 7 Myr, while UV traces the formation of stars down to $\sim 3 M_\odot$ which have lifetimes up to 300 Myr (Meurer et al. 2009). We converted the NUV-based SFR calibration used by Schiminovich et al. (2010) into the H α -based calibration of Meurer et al. (2009) and found that our calibration should yield SFRs 0.2 dex lower than Schiminovich et al. (2010) – that is, in the opposite direction to the displayed discrepancy.

While our sample is selected by H I mass, the Schiminovich et al. (2010) sample has a UV flux-limited selection, biasing their sample towards higher UV SFRs. The higher redshift range ($z < 0.05$) and consequent larger volume of their sample also allow a higher average H I mass and SFR. Similarly, the Huang et al. (2012)

comparison, we perform the KS test on the subset of stellar masses within the domain of the Schiminovich et al. (2010) sample.

sample is also a flux-limited, H I-selected sample with a higher redshift than SINGG. The brighter and highest redshift bins have a steep sSFR slope due to the flux limit, while nearby, volume-limited bins have a shallower slope. The combination of these two extremes results in the apparent turnover in their relation (Drinkwater et al., in preparation). The difference between our sample and Huang et al. (2012) also includes different algorithms for calculating M_* and SFR to those we use. They use spectral energy density fitting to get both these quantities, and note that the M_* estimates are primarily dependent on the reddest fluxes while the SFR estimates come primarily from UV fluxes. We conclude that the differences between our results and those of Huang et al. (2012) and Schiminovich et al. (2010) are due to differences in sample selection and the calibration of the quantities involved.

3.7 H I deficiency

In general, galaxies in high-density environments such as galaxy clusters and groups have less H I than galaxies of the same size and luminosity residing in the field (Haynes & Giovanelli 1983; Solanes et al. 2001; Kilborn et al. 2009). This deficiency in H I is quantified by the H I deficiency parameter, defined as the difference between the logarithms of the expected ($M_{\text{H I exp}}$) and observed H I mass ($M_{\text{H I obs}}$) of a galaxy (Haynes & Giovanelli 1983):

$$\text{DEF}_{\text{H I}} = \log[M_{\text{H I exp}}] - \log[M_{\text{H I obs}}].$$

An H I deficiency parameter of 0.3 dex translates into half the H I mass that we would expect a galaxy to have based on its optical luminosity or size. We consider an H I deficiency between -0.3 and 0.3 as normal H I content, as per Kilborn et al. (2009). In this section we exclude HIPASS J0205–55 due to the two HIPASS detections (see Appendix A), and HIPASS J2318–42a because one member is not completely within our field of view.

We used two independent methods to calculate the expected H I content for the Choir group galaxies. Our first method is to use the H I scaling relation in Dénes et al. (in preparation). This relation is found from an analysis of the HiPASS optical catalogue (HOPCAT; Doyle et al. 2005) and gives H I mass ($M_{\text{H I}}$) as a function of SuperCosmos R -band magnitude ($\text{Mag}_{R_{\text{SC}}}$):

$$\log(M_{\text{H I}}) = 3.82 - 0.3\text{Mag}_{R_{\text{SC}}}.$$

We compared the SuperCosmos R -band magnitudes in HOPCAT to our SINGG R -band (AB) magnitudes ($\text{Mag}_{R_{\text{AB}}}$) and found them to scale by $\text{Mag}_{R_{\text{SC}}} = 8.7 + 1.36\text{Mag}_{R_{\text{AB}}}$.

The inherent scatter in this relation is ± 0.3 dex. We then summed over all the members in each group and compared this to the measured H I content to calculate the total H I deficiency for each group. Our results are presented in Fig. 12 (upper panel).

Our second method for calculating the expected H I content is to use equation (2) from this paper, which gives H I mass based on H α luminosity and R -band surface brightness. This is shown in the lower panel of Fig. 12. Again, nearly all of our groups have normal H I content, with the exception of HIPASS J1059–09 and J1403–06, the two groups with the highest H α luminosity in our sample. The members of these two groups also have a high surface brightness, resulting in the highest total predicted H I mass in our sample. In fact, the two to three brightest members in both groups all have a higher predicted H I mass than the corresponding groups themselves (see Fig. 1). The uncertainty in the H I mass measurements of ~ 10 per cent (Koribalski et al. 2004) or 0.04 dex is negligible compared with the inherent scatter in equation (2) of 0.48, so we

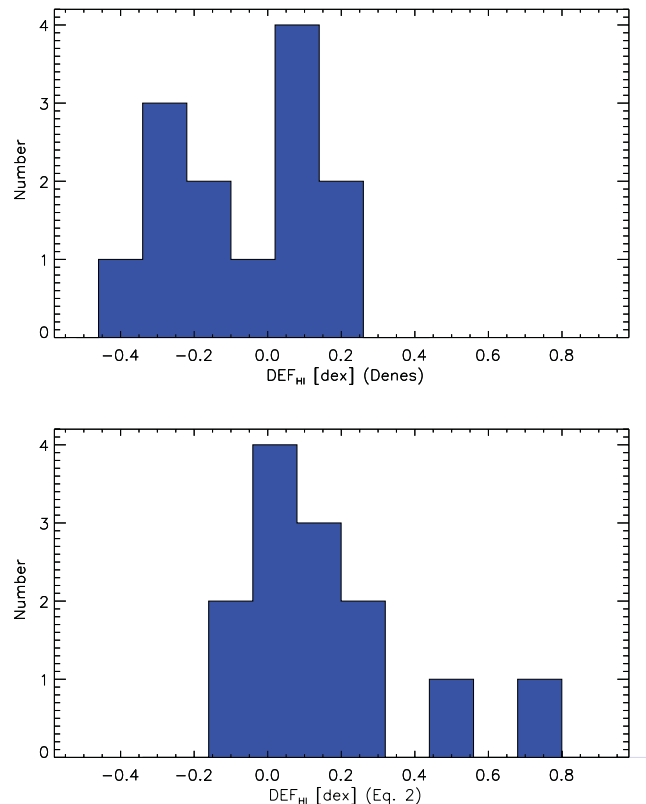


Figure 12. Distribution of H I deficiency parameter $\text{DEF}_{\text{H I}}$ for each Choir group, defined as the logarithmic difference between observed group H I mass and predicted group H I mass (determined by summing the predicted H I masses of the individual group galaxies). Our groups are on average not significantly H I deficient. Upper panel: expected H I mass based on R -band magnitude. Lower panel: expected H I masses based on equation (2). Two very H α luminous groups, HIPASS J1059–09 and J1403–06, are not significantly H I deficient in this definition.

adopt 0.48 dex as the uncertainty in H I deficiency. Hence, the deficiency of these two groups is not statistically significant in our definition.

The two different methods produce slightly different results because the scaling is based on different physical properties. That is, method (1) identifies groups as H I deficient when their stellar luminosity is high compared to their H I mass, while deficient groups in method (2) have a high SFR for their H I mass. The implication is that the two groups that are deficient by method (2) and not (1) are dominated by high-H α -EW starbursting galaxies.

The fact that the Choir groups show no significant H I deficiency is a similar result to Kilborn et al. (2009), who showed an average lack of H I deficiency for their sample of optically selected loose galaxy groups. The situation is less clear for compact groups, with Stevens et al. (2004) finding no significant H I deficiency, while Borthakur, Yun & Verdes-Montenegro (2010) found the typical H I deficiency of their sample of HCGs to be between 0.2 and 0.4 dex; in several cases the deficiency exceeded 0.5 dex.

We also compare the Choir groups to the gas-rich M81 group, as modelled by Nichols & Bland-Hawthorn (2011) in order to explain the H I deficiency of the LG (Grcevich & Putman 2009). They found that the M81 group must have commenced assembly at $z \sim 2$, in contrast to the LG which must have started by $z \sim 10$. The overall lack of H I deficiency of the Choir groups suggests that the group environment has not yet removed substantial amounts of H I gas

from these groups. Hence, the Choir groups are at an early stage of assembly. In the local context, this would make them more like the M81 group than the LG. Consequently we expect that, like the M81 group, the Choir groups have a larger system of H I clouds than the LG does. The fact that the Choir groups are gas rich and less evolved than the LG indicates that they may provide important information about how gas enters groups and galaxies.

4 CONCLUSIONS

In this paper we have presented the Choirs: fields of four or more H α -emitting galaxies found in the SINGG. We found 15 such groups in SINGG.

We make the following points.

(i) Due to selection effects, Choir groups are at the large distance, high-mass end of the parent SINGG sample of H I sources.

(ii) Choir member galaxies are not significantly different from the control SINGG sample in any of our measures of radius, H α EW, R-band surface brightness, sSFR or SFE.

(iii) The dwarf galaxies in our Choir groups are not detectable on their own in HiPASS, but are detected in SINGG because the entire group has sufficient H I to be selected in HiPASS.

(iv) Within the limitations of the SINGG imaging field of view, there are no giant elliptical galaxies in the Choir groups.

(v) Eight of the fifteen Choir groups are characterized by having two giant spiral galaxies and a number of smaller galaxies. In terms of *morphology* they can be considered to be LG analogues.

(vi) The mean group projected size is very compact at 190 kpc, much smaller than groups in the Garcia (1993) catalogue at 961 kpc, although not as compact as Hickson et al. (1989) Compact Groups at 87 kpc. The mean Choir compactness is also more than 3σ smaller than the same statistic for the LG. We note that our group size is limited by the field of view, with a maximum size of 380 kpc at the mean distance of 87 Mpc.

(vii) The sSFR ($=\text{SFR}/M_*$) of Choir member galaxies falls on the same M_* scaling relation as the rest of SINGG. This scaling relation is similar to what is found by for the ALFALFA H I-selected survey (Huang et al. 2012). However, galaxies from the M_* -selected GASS survey (Schiminovich et al. 2010) have sSFR 0.5 dex higher than our sample. Differences in the selection of the different samples, the depth of the observations and the SFR calibrations are likely to account for the differences between these surveys.

(viii) The SFE ($=\text{SFR}/M_{\text{HI}}$) of the Choir groups matches the sample of remaining SINGG members, which in turn is lower than the portion of the Schiminovich et al. (2010) sample with high sSFR. Our SINGG sample shows an increasing trend in SFE with stellar mass, consistent with Bothwell et al. (2009) and Huang et al. (2012).

(ix) On average our groups are not significantly H I deficient, unlike typical groups of galaxies. This suggests an earlier stage of assembly than the LG, and more like the M81 group (Nichols & Bland-Hawthorn 2011).

(x) Our results indicate that emission line selection is an efficient way to pick out candidate galaxy groups in blind H I surveys. This can be very important when the beam size is large compared to the separations of galaxies within groups. Here, it is the H α imaging that allows the small ELGs to be identified as likely dwarf group members. In comparison, astronomers using UV imaging alone to identify ELGs (e.g. Huang et al. 2012) may be reluctant to identify the smaller sources as dwarf members without follow-up spectroscopy.

In summary, H I combined with H α selection can result in the selection of H I-rich groups. These are fairly compact and typically contain sources with strong signs of interaction, although global properties appear fairly normal. In approximately half of the cases, the groups are similar to the LG in containing two bright large spirals and numerous dwarf galaxies, although the compactness suggests that the groups are at a more advanced stage of interaction than the LG. The lack of H I deficiency suggests that the groups are at an earlier stage of group assembly, more like the M81 group.

ACKNOWLEDGEMENTS

We wish to thank the anonymous referees for their helpful comments, David Schiminovich for making his data available to us and Aaron Robotham for useful discussions.

We acknowledge funding support from the University of Queensland–University of Western Australia Bilateral Research Collaboration Award and the Australian Research Council (grant DP110102608).

This research has made use of the NASA's Astrophysics Data System.

We also made use of the NASA/IPAC Extragalactic Database (NED) which is operated by the Jet Propulsion Laboratory, California Institute of Technology, under contract with the National Aeronautics and Space Administration.

This research used the facilities of the Canadian Astronomy Data Centre operated by the National Research Council of Canada with the support of the Canadian Space Agency.

JHK is supported by Korean Research Foundation (KRF) grant funded by the Korean government (MEST), No. 2010-0000712.

REFERENCES

- Abazajian et al., 2003, AJ, 126, 2081
 Barnes D. G. et al., 2001, MNRAS, 322, 486
 Bell E. F., McIntosh D. H., Katz N., Weinberg M. D., 2003, ApJS, 149, 289
 Bergvall N., 2012, Star Forming Dwarf Galaxies. Springer-Verlag, Berlin, p. 175
 Blanton M. R. et al., 2003, ApJ, 592, 819
 Borthakur S., Yun M. S., Verdes-Montenegro L., 2010, ApJ, 710, 385
 Bothwell M. S., Kennicutt R. C., Jr, Lee J. C., 2009, MNRAS, 400, 154
 Bournaud F. et al., 2007, Sci, 316, 1166
 Brinchmann J., Charlot S., White S. D. M., Tremonti C., Kauffmann G., Heckman T., Brinkmann J., 2004, MNRAS, 351, 1151
 Chabrier G., 2003, ApJ, 586, L133
 da Costa L. N., Pellegrini P. S., Davis M., Meiksin A., Sargent W. L. W., Tonry J. L., 1991, ApJS, 75, 935
 Doyle M. T. et al., 2005, MNRAS, 361, 34
 Gallego J., Zamorano J., Aragon-Salamanca A., Rego M., 1995, ApJ, 455, L1
 Garcia A., 1993, A&AS, 100, 47
 Garcia A. M., 1995, A&A, 297, 56
 Gómez P. L. et al., 2003, ApJ, 584, 210
 Grevech J., Putman M. E., 2009, ApJ, 696, 385
 Haynes M. P., Giovanelli R., 1983, ApJ, 275, 472
 Hickson P., Kindl E., Auman J. R., 1989, ApJS, 70, 687
 Huang S., Haynes M. P., Giovanelli R., Brinchmann J., 2012, ApJ, 756, 113
 Kennicutt R. C., Jr, 1989, ApJ, 344, 685
 Kennicutt R. C., Jr, 1998, ApJ, 498, 541
 Kilborn V. A., Forbes D. A., Barnes D. G., Koribalski B. S., Brough S., Kern K., 2009, MNRAS, 400, 1962
 Koribalski B. S. et al., 2004, AJ, 128, 16
 Lewis I. et al., 2002, MNRAS, 334, 673

- Meurer G. R. et al., 2006, *ApJS*, 165, 307
 Meurer G. R. et al., 2009, *ApJ*, 695, 765
 Meyer M. J. et al., 2004, *MNRAS*, 350, 1195
 Mould J. R. et al., 2000, *ApJ*, 529, 786
 Mulchaey J. S., 2000, *ARA&A*, 38, 289
 Mulchaey J. S., Zabludoff A. I., 1998, *ApJ*, 496, 73
 Nichols M., Bland-Hawthorn J., 2011, *ApJ*, 732, 17
 Pisano D. J., Barnes D. G., Staveley-Smith L., Gibson B. K., Kilborn V. A., Freeman K. C., 2011, *ApJS*, 197, 28
 Robotham A. S. G. et al., 2012, *MNRAS*, 424, 1448
 Rownd B. K., Young J. S., 1999, *AJ*, 118, 670
 Ryan-Weber E. V. et al., 2004, *AJ*, 127, 1431
 Salpeter E. E., 1955, *ApJ*, 121, 161
 Salzer J. J. et al., 2000, *AJ*, 120, 80
 Schiminovich D. et al., 2010, *MNRAS*, 408, 919
 Solanes J. M., Manrique A., García-Gómez C., González-Casado G., Giovanelli R., Haynes M. P., 2001, *ApJ*, 548, 97
 Stevens J. B., Webster R. L., Barnes D. G., Pisano D. J., Drinkwater M. J., 2004, *Publ. Astron. Soc. Aust.*, 21, 318
 Tody D., 1993, in Hanisch R. J., Brissenden R. J. V., Barnes J., eds, *ASP Conf. Ser. Vol. 52, Astronomical Data Analysis Software and Systems II*. Astron. Soc. Pac., San Francisco, p. 173
 Tully R. B., 1987, *ApJ*, 321, 280
 Tully R. B. et al., 2006, *AJ*, 132, 729
 Werk J. K. et al., 2010, *AJ*, 139, 279
 West A. A., Garcia-Appadoo D. A., Dalcanton J. J., Disney M. J., Rockosi C. M., Ivezić Ž., 2009, *AJ*, 138, 796
 Wijesinghe D. B. et al., 2012, *MNRAS*, 423, 3679
 Zwaan M. A. et al., 2004, *MNRAS*, 350, 1210

APPENDIX A: NOTES ON INDIVIDUAL CHOIR GROUPS

By ‘member’ we refer to objects with apparent $H\alpha$ emission in the filter used for the SINGG images. We note that these are likely groups; spectroscopic redshifts are needed to confirm membership, especially for the small, faint galaxies. We also searched larger 40 arcmin photographic survey images³ centred on the brightest member of each group (named ‘S1’) to check for any bright galaxies that could be group members.

HIPASS J0205–55. The field *HiPASS J0205–55* covers two sources: *HiPASS J0205–55a* at $V_{\text{hel}} = 6524 \text{ km s}^{-1}$ and *HiPASS J0205–55b* at $V_{\text{hel}} = 5964 \text{ km s}^{-1}$ (Meyer et al. 2004). We note that *HiPASS J0205–55a* is included in the SINGG sample selection while *HiPASS J0205–55b* is not (Meurer et al. 2006). Our observations show a total of nine galaxies in this rich field: four giant spirals and five dwarfs of varying sizes. The smallest (S8, S9) are almost in the ELdot category. The galaxies S1, S2, S3, S4 and S6 have published velocities of 6528, 5927, 6131, 5864 and 5756 km s^{-1} , respectively (da Costa et al. 1991). Hence, S1 is associated with *HiPASS J0205–55a*; S2, S4 and S6 are associated with *HiPASS J0205–55b*; while S3 is at an intermediate velocity. The existence of galaxies at velocities between the a and b components suggests that the two component systems are merging. The extended optical image of this group reveals one additional large galaxy, ESO 153–G020 (velocity 5197 km s^{-1}) associated with *HiPASS J0205–55b* (Doyle et al. 2005).

HIPASS J0209–10. The galaxies of this group show strong signs of interactions, all being classified as ‘pec’ and most having extensive extraplanar gas in the $H\alpha$ images. The group appears in

several group catalogues, and most notably it is HCG 16. We found no new $H\alpha$ -emitting galaxies compared to Meurer et al. (2006) which has a more detailed description of the members in its appendix. (There is a fainter galaxy 1.5 arcmin to the NE of S3 = NGC 0835, SDSS J020928.18–100653.6 but it is a background object, velocity = $25\,706 \text{ km s}^{-1}$.) The extended optical image of this group reveals one additional large galaxy, NGC 0848 (velocity 3989 km s^{-1}) also likely to be associated with the group (Garcia 1993).

HIPASS J0258–74. A typical small group with three spirals and one tiny dwarf irregular galaxy.

HIPASS J0400–52. Part of an extensive cluster (Abell 3193) with a total of nine members identified: four spirals and five dwarfs of varying sizes; two of these are very small companions to the giant S4 and S6 galaxies. The extended optical image of this group reveals two additional large galaxies, NGC 1506 ($10\,271 \text{ km s}^{-1}$) and ESO 156–G031 ($10\,467 \text{ km s}^{-1}$) at 10 and 15 arcmin from the central galaxy S1, respectively. These are both classified as S0 galaxies, so although associated with the group they are unlikely to contain large amounts of $H\text{I}$.

HIPASS J0443–05. An extended group of three large spirals, two with companions. The line emission of S5, an apparent companion to S1, is weak and needs to be confirmed.

HIPASS J1026–19. This group is dominated by a single face-on giant spiral (S1) which is connected to S2 by a tidal tail. The four other members are small and well separated, notably S3 which is on the very edge of the image.

HIPASS J1051–17. This extensive group has nine members distributed over much of the image. The galaxy S9 is notable for being an apparent dE,N galaxy with weak nuclear $H\alpha$ emission. The extended images reveal one additional large Sa galaxy, MCG-03-28-016 (6220 km s^{-1} , 9 arcmin from S1) which may possibly be associated with the group (5491 km s^{-1}).

HIPASS J1059–09. This group features a strongly interacting galaxy pair (S1 and S3) as well as several other spirals. The two newly measured galaxies are S9, a small, lopsided dwarf with one $H\text{II}$ region, and S10, an edge-on disc galaxy with faint apparent residual $H\alpha$ in the central region as well as weak, very low surface brightness $H\alpha$ along the NW minor axis. S10 is a confirmed group member (2MASX J10590262–0953197 at velocity 8229 km s^{-1}) and there are signs of interaction between it and S8, a possible low-surface-brightness group member. The extended image reveals a bright galaxy, MCG-01-28-020, at 15 arcmin from S1 but its velocity ($11\,779 \text{ km s}^{-1}$) makes it a background object.

HIPASS J1159–19. This compact group of four galaxies features a nearly face-on late-type spiral with bright $H\alpha$ emission, and three dwarfs to the S and SE. The field is also known as Arp 022 and is near to the well-known Antennae group, Arp 244.

HIPASS J1250–20. This is a typical group with two large spirals and three dwarf companions, but we also note the detection of two very compact $H\alpha$ emitters (S6 and S7) that may be on a tidal tail extending from S1. These are strong candidates for tidal dwarf galaxies in formation.

HIPASS J1403–06. This small group (four members) is dominated by two strongly interacting spirals catalogued as Arp 271, and also contains two faint ELdot-like dwarfs.

HIPASS J1408–21. The central galaxy of this group, S1, shows extended emission. The arm pointing south to S3 shows possible tidal distortion in the $H\alpha$ emission. There are two new galaxies in the field: S5 and S6. S5 is barely resolved with a single faint $H\text{II}$ region and located to the SW of S3, possibly at the extreme end of

³ Digitized Sky Survey images in the blue (B_J) band from the Canadian Astronomy Data Centre.

the tidal arm extending from S1. S6 appears to have weak residual $H\alpha$ in the nuclear region of a small, high-inclination disc, but may be due to bad continuum subtraction in a background galaxy. The extended image reveals a bright galaxy, ESO 578–G030, 11 arcmin from S1 but its velocity ($10\,891\text{ km s}^{-1}$) makes it a background object.

HIPASS J1956–50. This group consists of a large spiral, S1, to the east, a late-type spiral or irregular, S2, to the west, a nearly ELdot-like BCD, S3, projected between them and a new, faint compact dwarf S4 near the W edge of the frame which is difficult to spot due to nearby bad columns in the data. The large velocity spread of these objects (see Table B1) indicates that group membership needs to be confirmed for this group.

HIPASS J2027–51. This group contains two large distorted spirals, S1 and S2, a dwarf irregular, S3, and a compact near ELdot dwarf, S4. The data are relatively noisy, so may contain faint undetected members in addition to the four listed.

HIPASS J2318–42a. This nearby (1603 km s^{-1}) group consists of four large spiral galaxies: NGC 7582, NGC 7590, NGC 7599, plus NGC 7552 which is not visible in the fields of our optical images. The group is known as the ‘Grus Quartet’ (see Koribalski et al. 2004). We have identified one very faint additional group member in our $H\alpha$ imaging, denoted by S4 in our table: this is one of the faintest group dwarf galaxies in our sample, but follow-up observations have confirmed that it is a group member (Sweet et al., in preparation).

APPENDIX B: IMAGES

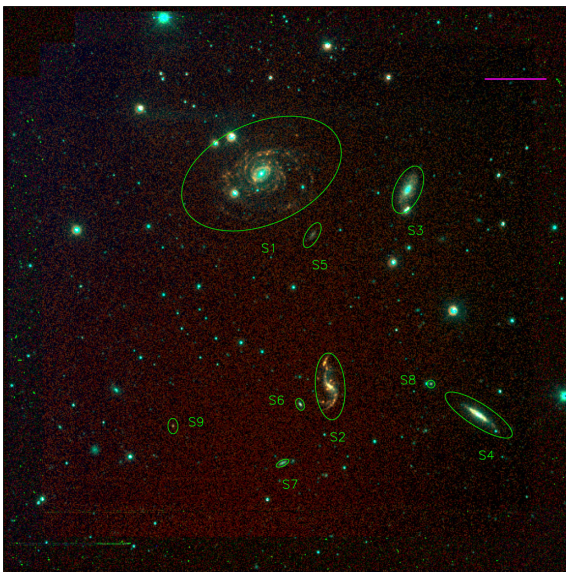


Figure B1. Choir group at HIPASS J0205–55. Colours are assigned as follows: R is displayed in the blue channel, the narrow-band $H\alpha$ in the green channel and the net $H\alpha$ shown in the red channel. ELGs thus appear red. Aperture colours are as follows: green denotes ELGs measured in SINGG, while yellow indicates newly discovered ELGs. Each image is 15.5 arcmin on a side. The magenta scale bars indicate 50 kpc. North is up and east is left. (Figs B1–B15 make use of this colour scheme, scale and orientation.)

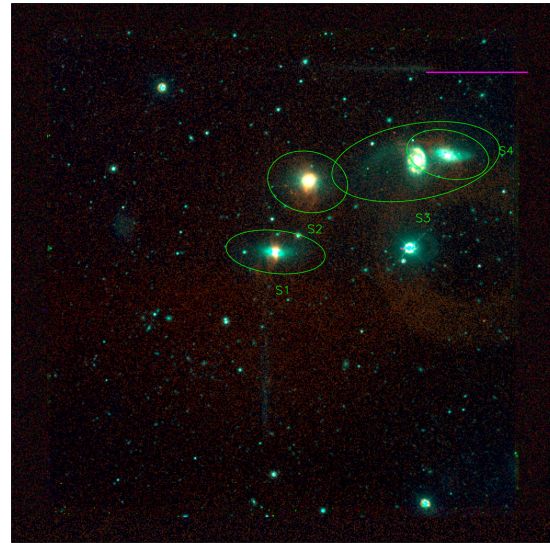


Figure B2. HIPASS J0209–10.

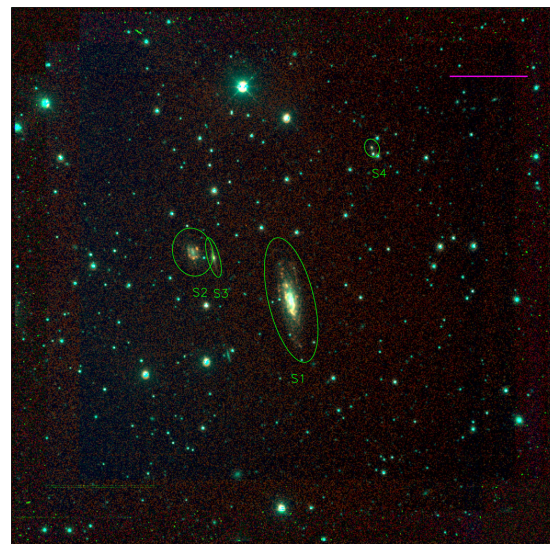


Figure B3. HIPASS J0258–74.

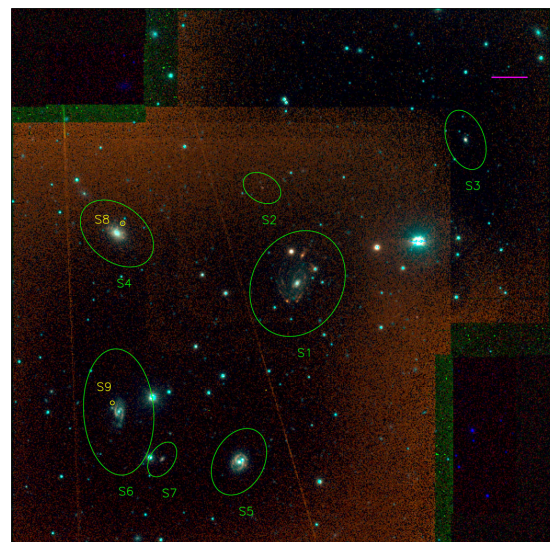
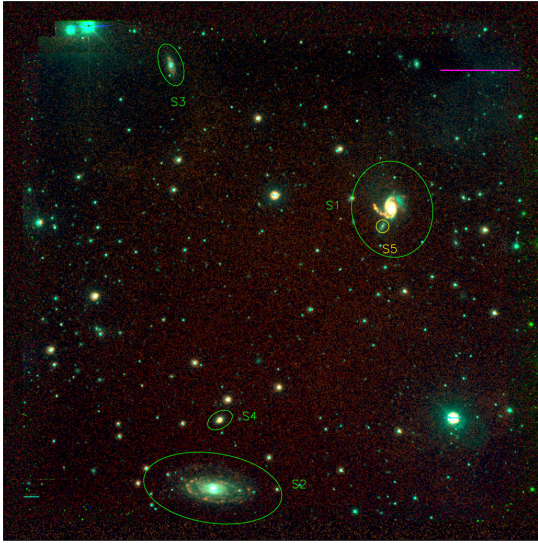
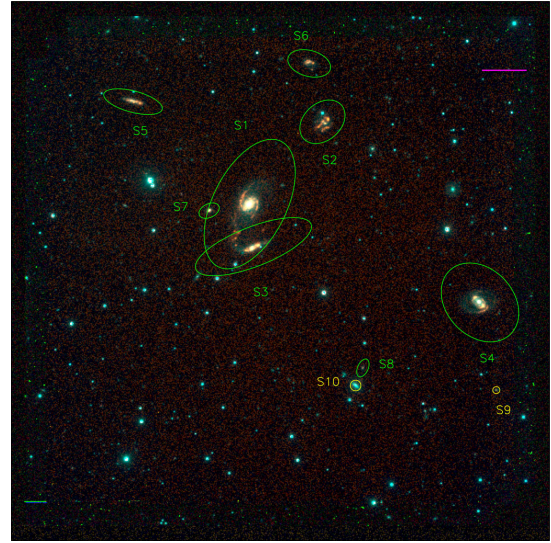
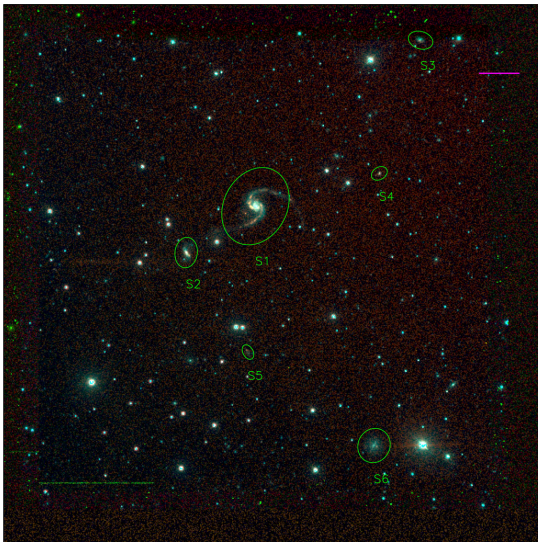
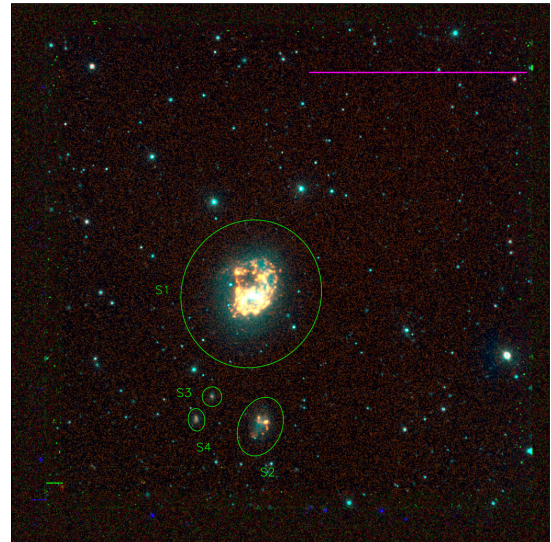
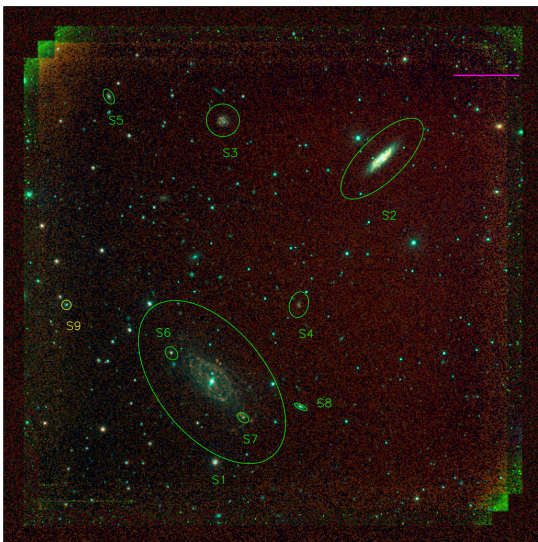
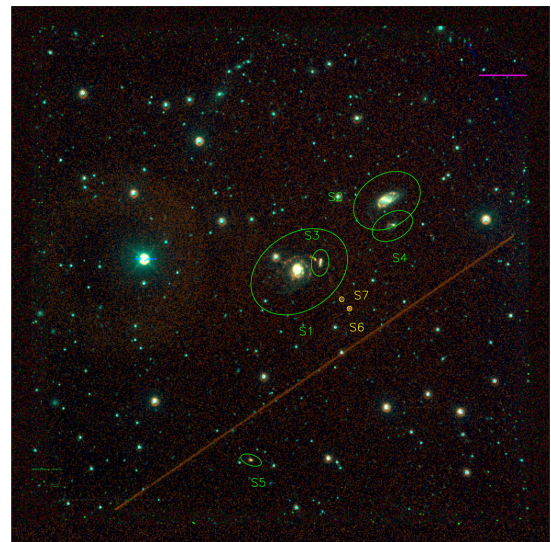


Figure B4. HIPASS J0400–52.

558 *S. M. Sweet et al.***Figure B5.** HiPASS J0443–05.**Figure B8.** HiPASS J1059–09.**Figure B6.** HiPASS J1026–19.**Figure B9.** HiPASS J1159–19.**Figure B7.** HiPASS J1051–17.**Figure B10.** HiPASS J1250–20.

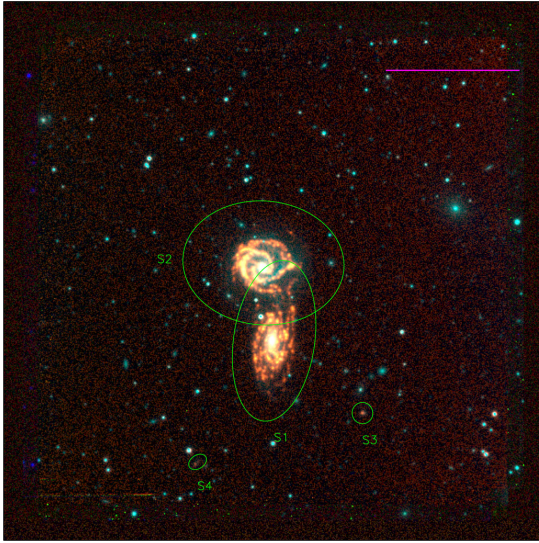


Figure B11. HiPASS J1403–06.

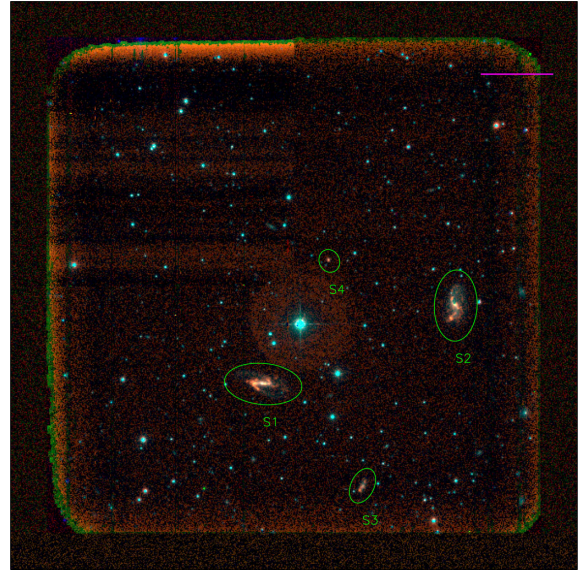


Figure B14. HiPASS J2027–51.

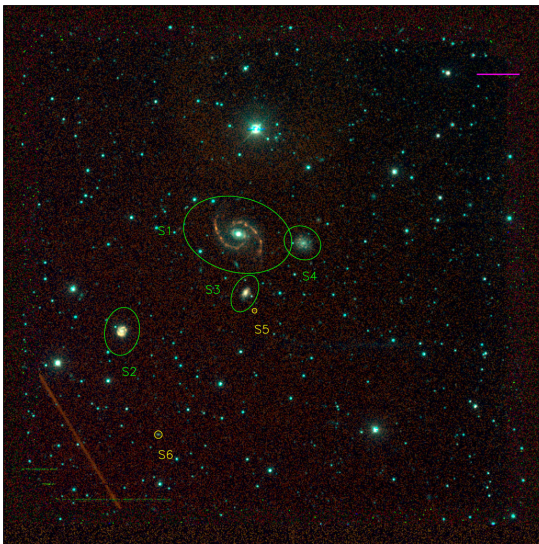


Figure B12. HiPASS J1408–21.

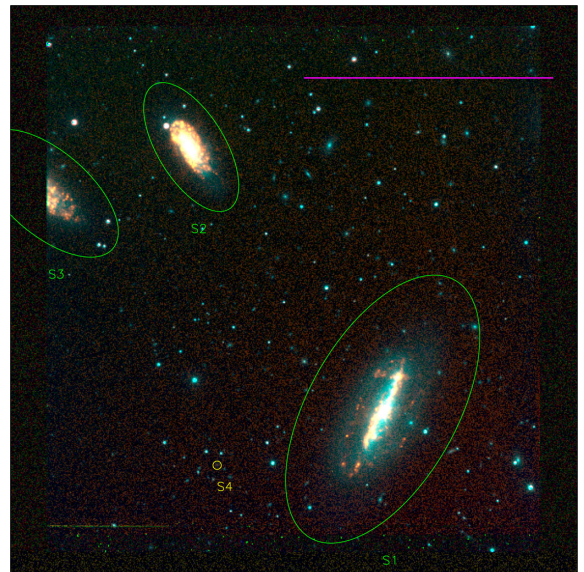


Figure B15. HiPASS J2318–42a.

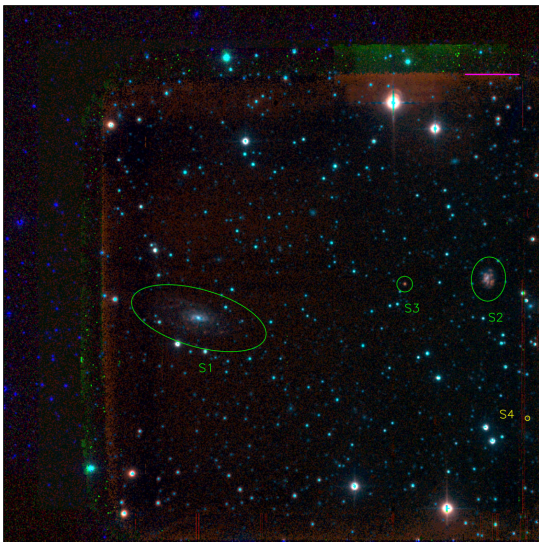


Figure B13. HiPASS J1956–50.

Endnotes to the Chapter

Section 3.7: HI deficiency. The large offset between HOPCAT and SINGG R -band magnitudes arises from the method used by Doyle et al. (2005) to measure magnitudes from the SuperCosmos plates. In that survey, R - and I -band magnitudes were measured within the same elliptical apertures as B -band magnitudes were, leading to a systematic offset from other surveys. The scaling relation is therefore necessary to allow the HOPCAT measurements to be reliably compared with SINGG. Further details can be found in Dénes et al. (2014).

3

The Metallicity of Dwarf Galaxies

In the previous paper I defined the sample for this thesis: star-forming member galaxies located in fairly compact, gas-rich galaxy groups.

In this paper I recalibrate the luminosity-metallicity relation for a control sample of $\sim 100,000$ galaxies and use this to define a diagnostic for selecting TDG candidates from my sample of galaxies. I apply the diagnostic to 53 galaxies within my sample and find three TDG candidates and four very metal poor galaxies.

CHOIRS H I GALAXY GROUPS: THE METALLICITY OF DWARF GALAXIES

SARAH M. SWEET¹, MICHAEL J. DRINKWATER¹, GERHARDT MEURER^{2,3}, KENJI BEKKI^{2,3},
MICHAEL A. DOPITA^{4,5,6}, VIRGINIA KILBORN⁷, AND DAVID C. NICHOLLS⁴¹ School of Mathematics and Physics, University of Queensland, Qld 4072, Australia; sarah@sarahsweet.com.au² School of Physics, University of Western Australia, 35 Stirling Highway, Crawley, WA 6009, Australia³ International Centre for Radio Astronomy Research, ICRAR M468, 35 Stirling Highway, Crawley, WA 6009, Australia⁴ Research School of Astronomy and Astrophysics, Australian National University, Cotter Road, Weston ACT 2611, Australia⁵ Astronomy Department, King Abdulaziz University, P.O. Box 80203 Jeddah, Saudi Arabia⁶ Institute for Astronomy, University of Hawaii, 2680 Woodlawn Drive, Honolulu, HI 96822, USA⁷ Swinburne University of Technology, Mail number H30, PO Box 218, Hawthorn, Victoria 3122, Australia*Received 2013 October 16; accepted 2013 December 20; published 2014 January 23*

ABSTRACT

We present a recalibration of the luminosity–metallicity relation for gas-rich, star-forming dwarfs to magnitudes as faint as $M_R \sim -13$. We use the Dopita et al. metallicity calibrations to calibrate the relation for all the data in this analysis. In metallicity–luminosity space, we find two subpopulations within a sample of high-confidence Sloan Digital Sky Survey (SDSS) DR8 star-forming galaxies: 52% are metal-rich giants and 48% are metal-medium galaxies. Metal-rich dwarfs classified as tidal dwarf galaxy (TDG) candidates in the literature are typically of metallicity $12 + \log(\text{O}/\text{H}) = 8.70 \pm 0.05$, while SDSS dwarfs fainter than $M_R = -16$ have a mean metallicity of $12 + \log(\text{O}/\text{H}) = 8.28 \pm 0.10$, regardless of their luminosity, indicating that there is an approximate floor to the metallicity of low-luminosity galaxies. Our hydrodynamical simulations predict that TDGs should have metallicities elevated above the normal luminosity–metallicity relation. Metallicity can therefore be a useful diagnostic for identifying TDG candidate populations in the absence of tidal tails. At magnitudes brighter than $M_R \sim -16$, our sample of 53 star-forming galaxies in 9 H I gas-rich groups is consistent with the normal relation defined by the SDSS sample. At fainter magnitudes, there is an increase in dispersion of the metallicity of our sample, suggestive of a wide range of H I content and environment. In our sample, we identify three (16% of dwarfs) strong TDG candidates ($12 + \log(\text{O}/\text{H}) > 8.6$) and four (21%) very metal-poor dwarfs ($12 + \log(\text{O}/\text{H}) < 8.0$), which are likely gas-rich dwarfs with recently ignited star formation.

Key words: galaxies: abundances – galaxies: dwarf – galaxies: formation – galaxies: groups: general – galaxies: star formation – techniques: spectroscopic

Online-only material: color figures

1. INTRODUCTION

Over the past few decades, it has been shown that galaxies display an increasing metallicity with luminosity and, more fundamentally, mass (e.g., Lequeux et al. 1979; Garnett & Shields 1987; Skillman et al. 1989; Brodie & Huchra 1991; Zaritsky et al. 1994; Tremonti et al. 2004; Zahid et al. 2012). The general explanation for this relation is that two concurrent processes are at work. The first is that in the lambda cold dark matter framework, most galaxies start at the low-luminosity, low-metallicity end of the trend line, forming out of pristine gas clumping within dark matter (DM) haloes. Over time, DM halos and their respective galaxies merge together to form ever larger haloes and galaxies. The second concurrent process is the self-enrichment of galaxies due to supernovae, with more massive galaxies retaining greater percentages of the ejecta than low-mass galaxies in the face of galactic winds (Gibson & Matteucci 1997; Kauffmann et al. 2003), and/or being more efficient at converting the enriched gas into stars (Dalcanton 2007). These two processes cause galaxies to move diagonally upward along the trend line toward simultaneously higher mass and higher metallicity.

However, not all dwarf galaxies are formed out of metal-poor gas in their own DM halo. Tidal interactions between giant galaxies cause knots of star formation in tidal tails, which can self-gravitate without the need for a DM halo. The dwarf galaxies formed in this way are known as tidal dwarf galaxies

(TDGs), and have high metallicities due to the pre-enriched matter from which they form (e.g., Mirabel et al. 1992; Duc et al. 2000; Weilbacher et al. 2003). There are a number of important implications for the study of TDGs, for example, the DM fraction within TDGs can constrain theories of gravity; the fraction of dwarf galaxies that form tidally and survive to the present day significantly affects the dwarf galaxy mass function (see, e.g., Bournaud 2010).

It is not yet known what fraction of dwarf galaxies are TDGs; between “several” (Bournaud 2010) and 50% (Hunsberger et al. 1996) of dwarf galaxies are predicted to form in a tidal manner. This is still an open question, primarily because two TDG criteria (low DM, high metallicity) are difficult to reliably quantify. First, the presence of tidal streams around currently known TDGs prevents them from reaching the virial equilibrium required for measuring total mass and confirming the presence or absence of DM. Second, the various metallicity calibrations defined in the literature yield inconsistent metallicity measurements (e.g., Kewley & Ellison 2008).

To test what fraction of dwarf galaxies form in a tidal manner, we have identified a sample of H I gas-rich groups of galaxies where there is no obvious optical interaction, but the dwarf galaxies have higher rates of star formation than expected for the group environment. This sample is ideal for locating and measuring TDGs because the past interactions in the group provide the necessary conditions for the TDGs to form, but the lack of current optical interaction means that the TDGs would be

old enough for their progenitor tidal tails to have dissipated since forming them, and the TDGs would be in virial equilibrium. This allows a sound measurement of their dynamical masses and tests of theories of gravity.

Our aim is to determine the importance of tidal processes in forming dwarf galaxies in groups. In this paper, we investigate the trend of metallicity with respect to luminosity of these objects in order to identify a population of candidate TDGs. Here we define “metallicity” as the gas-phase oxygen abundance relative to hydrogen, $12+\log(\text{O}/\text{H})$. The following section covers the sample selection, observations, and data processing. In Section 3, we present the luminosity–metallicity relation and discuss the implications in Section 4. Our conclusions are in Section 5.

2. SAMPLE SELECTION, OBSERVATIONS, DATA PROCESSING, AND MEASUREMENT

Our sample consists of galaxies in small gas-rich groups named Choir groups (Sweet et al. 2013, hereafter Paper 1). The groups were selected from the H I Parkes All-Sky Survey (HIPASS; Barnes et al. 2001), being the H I detections that were revealed by the Survey of Ionization of Neutral Gas Galaxies (SINGG; Meurer et al. 2006) to contain four or more emission-line galaxies. In Paper 1, we presented a catalog of the Choir group members and a discussion of their properties in the context of SINGG. Briefly, the Choir groups are on average more compact than groups in the Garcia (1993) catalogue, but less so than Hickson compact groups (HCGs; Hickson et al. 1989). Eight of them contain two large spirals and a number of dwarf galaxies, and as such are morphological analogs of the Local Group, albeit in a more compact state.

We observed 53 Choir member galaxies in nine groups with the integral field Wide Field Spectrograph (WiFeS; Dopita et al. 2007) on the Australian National University’s 2.3 m telescope. This IFU has a $25'' \times 38''$ field of view with $1''$ square spaxels (spatial pixels). The red R7000 and blue B3000 gratings (resolutions $R = 7000$ and 3000 , respectively) were selected to achieve a maximum velocity resolution of 45 km s^{-1} in the red arm to facilitate redshift measurements with the $\text{H}\alpha$ line and maximum sensitivity in the blue to facilitate measurement of abundance-sensitive spectral lines. The resulting wavelength ranges were 329–558 nm in the blue arm and 529–912 nm in the red. The RT560 dichroic was used to ensure that the overlapping wavelength region did not contain strong features at the expected redshifts of our sample. Table 1 lists the observing log. We found that the nod-and-shuffle observing mode provided the best sky subtraction, as it interleaves sky and object exposures to best account for time-varying sky brightness. For each run, we obtained the usual set of bias frames, and for each night a set of wavelength arc, flat, and “wire” calibration frames. Spectrophotometric standard stars were observed nightly for each galaxy group. The data were processed using the IRAF-based pipeline described by Dopita et al. (2010).

The best-known advantage of integral field unit (IFU) spectroscopy is the acquisition of spatially resolved spectra. However, for this study we integrate over a number of spaxels per galaxy, so instead the advantages are increased signal to noise and an improved sampling over the entire galaxy. We are conducting a full spatially resolved kinematic and metallicity analysis of these targets and will present the results in a future paper (S. M. Sweet et al., in preparation). For the dwarf galaxies, which fit within one pointing of the $25'' \times 38''$ field of view,

we integrated over a grid of spaxels containing those with $\gtrsim 3\sigma$ signal in $\text{H}\alpha$. This corresponds to 25–30 spaxels for a typical dwarf (in angular size) in our sample. For the giant galaxies, which do not fit within a single pointing, we integrated over the bright H II region nearest the center of the galaxy. We tested the effect of different aperture sizes on measured metallicity and found that expanding the aperture to include diffuse regions of the galaxies gave consistent metallicity results with those measured only for the bright central H II region. This corresponds well with previous findings that gas-rich, star-forming dwarfs are well mixed (Kobulnicky & Skillman 1997; Lee & Skillman 2004). We measured redshifts for each integrated spectrum and confirmed that these are not background galaxies.

We measured emission-line fluxes using UHSPECFIT (Rich et al. 2010). This IDL-based program fits a Bruzual & Charlot (2003) stellar population to account for absorption before fitting Gaussian components for each emission line. For most of the galaxies, the integrated emission lines are narrow enough that a single-component Gaussian provides a good fit (see Figure 1); any residuals between the Gaussian fit and the observed spectrum are within the noise of the spectrum. For the giant galaxies that have broad components, we have fit multiple Gaussian components, and again the residuals are within the spectrum noise. Reddening corrections were calculated based on the $\text{H}\alpha/\text{H}\beta$ ratio, assuming that the wavelength-dependent attenuation is due to an isothermal screen of dust, following Vogt et al. (2013; see their Appendix). Errors in flux measurements were estimated with a Monte Carlo simulation: simulated Gaussian distributions were added to random locations in the observed continuum, and the standard deviation of the measured fluxes was calculated.

Example spectra are shown in Figure 1. We present measured fluxes in Table 2.

3. RESULTS

We constructed the luminosity–metallicity relation for our Choir member galaxies and comparison samples using the same metallicity calibration (and, where possible, reddening correction) for all of the measurements. Although the metallicity is more fundamentally related to stellar mass than to luminosity (e.g., Tremonti et al. 2004), we restricted this analysis to luminosity because of the expected large scatter in the (unknown) mass-to-light ratios of our objects, which renders it difficult to make sensible, consistent mass estimates for these galaxies. In this section, we discuss our adopted metallicity calibration and discuss our comparison samples.

3.1. Metallicity Calibration

Calibrations of gas-phase metallicity typically fall into three main categories:

1. the classical electron-temperature and ionization-correction-factor technique (e.g., Peimbert & Costero 1969; Stasińska 1978, 2005),
2. the recombination line method (e.g., Esteban et al. 1998; López-Sánchez et al. 2007), and
3. the strong emission-line (SEL) method (e.g., Pagel et al. 1979; McGaugh 1991; Kewley & Dopita 2002; Dopita et al. 2013).

Measuring electron temperature allows a “direct” measurement of metallicity from strongly temperature-dependent emission lines. As such it is seen as the gold standard, but is difficult in

Table 1
WiFeS Observations

HIPASS+	Optical ID	R.A. (h m s)	Decl. (d m s)	Obs. Date	Int. Time (s)	Mode
(1)	(2)	(3)	(4)	(5)	(6)	(7)
J0205-55:S1b	ESO153-G017	02 05 05.48	-55 06 42.54	2011 Sep 20	3600	N
J0205-55:S2c	ESO153-IG016	02 04 50.78	-55 13 01.55	2011 Sep 21	5400	N
J0205-55:S2d		02 04 50.78	-55 13 01.55	2011 Sep 21	5400	N
J0205-55:S3a	ESO153-G015	02 04 34.92	-55 07 09.65	2012 Oct 06	3600	N
J0205-55:S4a	ESO153-G013	02 04 19.75	-55 13 50.44	2011 Sep 20	2700	N
J0205-55:S5	APMUKS	02 04 54.77	-55 08 31.99	2011 Sep 12	3600	S
J0205-55:S6	APMUKS	02 04 57.07	-55 13 34.10	2011 Sep 22	4500	S
J0205-55:S7	6dF	02 05 00.57	-55 15 19.63	2011 Sep 22	4500	S
J0205-55:S8	APMUKS	02 04 29.71	-55 12 56.09	2012 Oct 06	3600	S
J0205-55:S9	APMUKS	02 05 23.76	-55 14 14.20	2012 Oct 07	4800	S
J0258-74:S1b	ESO031-G005	02 58 06.48	-74 27 22.79	2012 Oct 08	2700	N
J0258-74:S2	MRSS	02 58 52.43	-74 25 53.25	2012 Oct 08	2700	N
J0258-74:S3	2MASX	02 58 42.76	-74 26 03.55	2012 Oct 09	3150	N
J0258-74:S4	MRSS	02 57 29.23	-74 22 34.75	2012 Oct 09	4500	S
J0400-52:S1	ESO156-G029	04 00 40.82	-52 44 02.71	2012 Oct 07	3600	N
J0400-52:S2	APMUKS	04 00 48.07	-52 41 02.81	2012 Oct 07	3600	S
J0400-52:S3	2MASX	04 00 06.03	-52 39 32.63	2012 Oct 07	2400	S
J0400-52:S4	IC2028	04 01 18.23	-52 42 27.08	2012 Jul 08	3150	N
J0400-52:S5	2MASX	04 00 53.00	-52 49 38.43	2012 Jul 08	3150	N
J0400-52:S6	IC2029	04 01 17.84	-52 48 02.81	2012 Oct 09	4500	N
J0400-52:S7	APMUKS	04 01 08.99	-52 49 32.78	2012 Oct 09	4500	S
J0400-52:S8	...	04 01 17.00	-52 42 08.50	2012 Jul 08	3150	N
J0400-52:S9	...	04 01 19.29	-52 47 56.10	2012 Oct 09	4500	N
J1051-17:S1a	2MASX	10 51 37.45	-17 07 29.23	2011 Apr 30	1800	C
J1051-17:S1b		10 51 37.45	-17 07 29.23	2011 Apr 30	2100	C
J1051-17:S1c		10 51 37.45	-17 07 29.23	2011 Apr 30	2700	C
J1051-17:S2a	NGC 3431	10 51 15.11	-17 00 29.44	2011 May 01	1800	C
J1051-17:S2b		10 51 15.11	-17 00 29.44	2011 May 01	1800	C
J1051-17:S3	...	10 51 35.94	-16 59 16.80	2011 Apr 28-29	7200	N
J1051-17:S4	...	10 51 26.01	-17 05 03.61	2011 Apr 29	5400	S
J1051-17:S5	...	10 51 50.91	-16 58 31.64	2011 May 01	5400	S
J1051-17:S6	...	10 51 42.78	-17 06 34.59	2011 Apr 30	3600	C
J1051-17:S7	...	10 51 33.36	-17 08 36.63	2011 Apr 30	3600	C
J1051-17:S8	...	10 51 25.92	-17 08 16.44	2011 Apr 29	5400	S
J1051-17:S9	...	10 51 56.54	-17 05 03.50	2012 May 18	3600	N
J1403-06:S1a	NGC 5426	14 03 24.88	-06 04 09.14	2012 May 21	1650	N
J1403-06:S2a	NGC 5427	14 03 26.09	-06 01 51.20	2012 May 21	1800	N
J1403-06:S2b		14 03 26.09	-06 01 51.20	2012 May 21	1800	N
J1403-06:S3	APMUKS	14 03 13.48	-06 06 24.17	2012 May 21	3600	S
J1403-06:S4	APMUKS	14 03 34.62	-06 07 59.27	2012 May 21	5400	S
J1408-21:S1a	ESO578-G026	14 08 42.04	-21 35 49.82	2012 May 20	2700	N
J1408-21:S1b		14 08 42.04	-21 35 49.82	2012 May 20	5400	N
J1408-21:S1c		14 08 42.04	-21 35 49.82	2012 May 20	4500	N
J1408-21:S1d		14 08 42.04	-21 35 49.82	2012 May 20	4500	N
J1408-21:S2	2MASX	14 08 57.72	-21 38 52.47	2012 May 18	2700	N
J1408-21:S3	2MASX	14 08 41.04	-21 37 40.97	2012 May 19	3600	N
J1408-21:S4	2MASX	14 08 33.28	-21 36 07.18	2012 May 19	3600	N
J1408-21:S5	...	14 08 39.82	-21 38 14.30	2012 May 19	9000	S
J1408-21:S6	...	14 08 52.84	-21 42 07.20	2012 May 18	3000	S/N
J1956-50:S1b		19 56 45.51	-50 03 20.29	2011 Sep 20	3600	N
J1956-50:S1c		19 56 45.51	-50 03 20.29	2011 Sep 20	5400	N
J1956-50:S1d	IC4909	19 56 45.51	-50 03 20.29	2011 Sep 22	5400	N
J1956-50:S1e		19 56 45.51	-50 03 20.29	2011 Sep 22	5400	N
J1956-50:S2	2MASX	19 55 53.21	-50 02 10.82	2011 Sep 21	3600	N
J1956-50:S3	...	19 56 08.20	-50 02 21.56	2011 Sep 21	5400	S
J1956-50:S4	...	19 55 45.92	-50 06 15.50	2011 Sep 22	5400	S
J2027-51:S1a	ESO234-G032	20 28 06.39	-51 41 29.83	2011 Apr 30	3600	C
J2027-51:S1b		20 28 06.39	-51 41 29.83	2011 Apr 29-30	4200	C
J2027-51:S1c		20 28 06.39	-51 41 29.83	2011 Apr 30	3600	C
J2027-51:S2a	ESO234-G028	20 27 31.97	-51 39 20.81	2011 Sep 19	3600	N
J2027-51:S2c		20 27 31.97	-51 39 20.81	2011 Sep 19	3600	N
J2027-51:S3	MRSS	20 27 48.52	-51 44 19.35	2011 Apr 28	6600	N
J2027-51:S4	...	20 27 54.64	-51 38 04.52	2011 Apr 29	5400	S
J2318-42a:S1c	NGC 7582	23 18 23.44	-42 22 11.94	2012 May 21	1350	N

Table 1
(Continued)

HIPASS+	Optical ID	R.A. (h m s)	Decl. (d m s)	Obs. Date	Int. Time (s)	Mode
(1)	(2)	(3)	(4)	(5)	(6)	(7)
J2318-42a:S1d		23 18 23.44	-42 22 11.94	2012 May 21	900	N
J2318-42a:S2a	NGC 7590	23 18 54.78	-42 14 18.94	2012 May 20	1800	N
J2318-42a:S2b		23 18 54.78	-42 14 18.94	2012 May 20	1800	N
J2318-42a:S3a	NGC 7599	23 19 21.14	-42 15 24.6	2012 May 21	1800	N
J2318-42a:S3b		23 19 21.14	-42 15 24.6	2012 May 21	1800	N
J2318-42a:S4	APMUKS	23 18 50.44	-42 23 50.30	2012 May 19	5400	S

Notes. Columns: (1): SINGG name with (a–e) appended for pointing where applicable; (2): name assigned to group as found in NASA/IPAC Extragalactic Database (NED; <http://ned.ipac.caltech.edu/>); (3): J2000 right ascension of brightest source in field; (4): J2000 declination of brightest source in field; and (5): date of observations; (6): total integration time; (7): Mode of observation. N denotes nod and shuffle, S denotes sub-aperture nod and shuffle, C denotes classical observation.

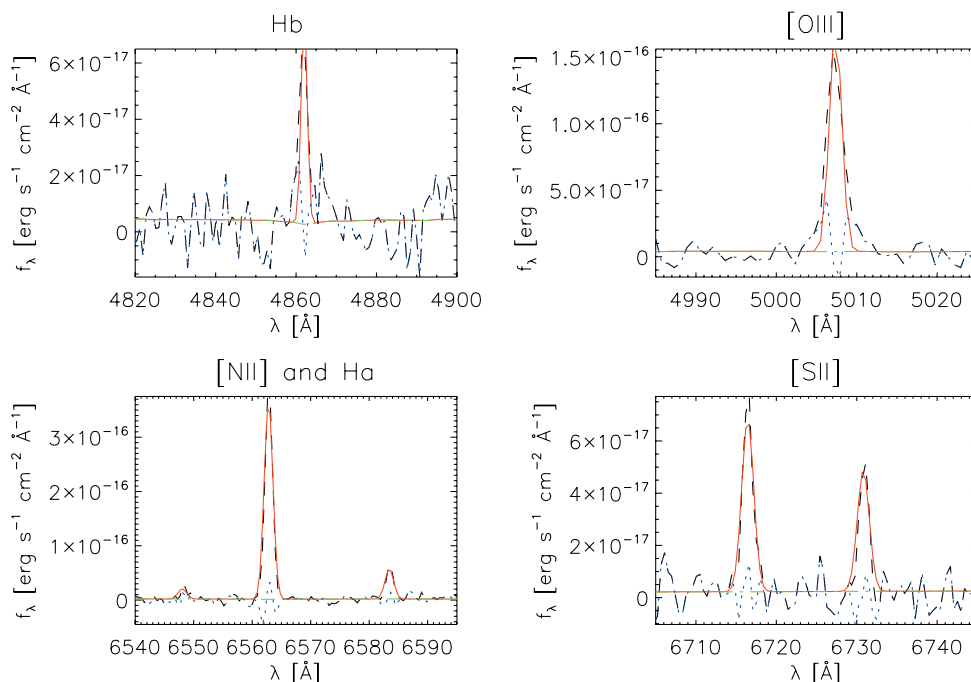


Figure 1. Example of emission-line fitting process. We show cutouts of one WiFeS spectrum (black) in the regions of interest with the best fit from UHSPECFIT (red), the fitted continuum (green dashed), and residuals (blue). This spectrum is from HIPASS J1408-21:S5, the faintest dwarf in our sample. (A color version of this figure is available in the online journal.)

practice because the required auroral lines (e.g., [O III] λ 4363) are weak. Further, the auroral line strengths are anticorrelated to metallicity, so are only measurable for low-metallicity galaxies. The recombination line method is also difficult, because the recombination lines are intrinsically weak. These methods are therefore reserved for bright and/or nearby galaxies. The galaxies in our sample are mostly high-metallicity, faint, and not very nearby, so most do not display the required lines for either the electron-temperature or recombination-line methods. Although the SEL method has limitations, which are discussed in the following paragraph, it is better suited to our sample than the other two methods. We therefore adopt the SEL method for this work.

Unfortunately, the three categories of methods give different results, so it is difficult to compare metallicities that have been calibrated with different methods. There is even wide variation within the various SEL methods, as seen in Figure 4 of Kewley & Ellison (2008). In part, this is because the models are

often degenerate: many, such as the often-used R_{23} calibration (Pagel et al. 1979), have high- and low-abundance branches, determined by differences in the ionization parameter q . This leads to an undefined region below the degeneracy in metallicity (López-Sánchez et al. 2012). The other major cause of discrepancy between the models is their failure to account for known physics. For instance, the models assume a Maxwellian photon-energy distribution. Nicholls et al. (2012, 2013) suggested that a high-energy excess of ionizing photons could be characterized as a “ κ -distribution” (generalized Lorentzian distribution). Dopita et al. (2013) have since developed an SEL model that accounts for this distribution and encouragingly gives much more consistent results with recombination-line and electron-temperature methods.

Furthermore, when analyzing metallicities by the SEL method, it is important to choose (1) a single metallicity calibration (so that the sample is self-consistent) that (2) is as free of degeneracy as possible. For these reasons, we adopt the

Table 2
Measured Emission-line Fluxes and Other Quantities

HIPASS+	H β 4861.3	[O III] 5006.9	H α 6562.8	[N II] 6583.4	[S II] 6716.4	[S II] 6730.8	12+log(O/H)	M_R (mag)	V_{hel} (km s $^{-1}$)
(1)	(2)	(3)	(4)	(5)	(6)	(7)	(8)	(9)	(10)
J0205-55:S1	1560 ± 140	337 ± 85	6000 ± 378	3110 ± 200	531 ± 51	371 ± 23	9.35 ± ^{0.03} _{0.03}	-22.57 ± 0.22	6490
J0205-55:S2	9110 ± 810	13500 ± 1200	29300 ± 3000	4590 ± 490	5120 ± 490	3630 ± 340	8.61 ± ^{0.07} _{0.07}	-19.22 ± 0.00	5941
J0205-55:S3	423 ± 119	436 ± 116	2680 ± 340	1390 ± 190	348 ± 80	243 ± 30	9.20 ± ^{0.05} _{0.06}	-22.00 ± 0.09	6074
J0205-55:S4	417 ± 64	425 ± 53	1740 ± 113	943 ± 62	665 ± 46	465 ± 24	8.94 ± ^{0.04} _{0.04}	-17.32 ± 0.18	5941
J0205-55:S5 ^c	1100 ± 390	873 ± 369	1220 ± 290	154 ± 348	0 ± 0	0 ± 0	0.00 ± ^{0.00} _{0.00}	-18.40 ± 0.06	6216
J0205-55:S6	629 ± 88	1470 ± 180	2220 ± 240	339 ± 42	563 ± 55	394 ± 35	8.41 ± ^{0.09} _{0.09}	-15.78 ± 1.08	5758
J0205-55:S7 ^a	186 ± 139	951 ± 170	855 ± 141	413 ± 108	206 ± 87	144 ± 16	8.93 ± ^{0.14} _{0.19}	-17.65 ± 0.05	5758
J0205-55:S8	1420 ± 190	738 ± 190	1750 ± 270	369 ± 129	327 ± 61	229 ± 32	8.78 ± ^{0.19} _{0.20}	-15.37 ± 0.12	5891
J0205-55:S9	399 ± 28	1520 ± 140	1330 ± 200	93 ± 12	167 ± 23	117 ± 16	8.28 ± ^{0.22} _{0.26}	-21.55 ± 0.12	6120
J0258-74:S1	1290 ± 130	789 ± 75	5760 ± 610	1880 ± 220	815 ± 84	596 ± 56	9.08 ± ^{0.05} _{0.06}	-19.48 ± 0.29	4883
J0258-74:S2	864 ± 99	2560 ± 290	2920 ± 440	250 ± 41	371 ± 58	260 ± 40	8.40 ± ^{0.12} _{0.13}	-18.51 ± 0.56	4883
J0258-74:S3	451 ± 45	226 ± 24	2620 ± 230	983 ± 89	668 ± 61	505 ± 46	8.98 ± ^{0.05} _{0.05}	-17.32 ± 0.85	4655
J0258-74:S4	1020 ± 100	3700 ± 340	3490 ± 510	175 ± 29	403 ± 59	303 ± 42	8.11 ± ^{0.14} _{0.14}	-21.90 ± 0.06	4838
J0400-52:S1 ^c	280 ± 31	4720 ± 520	0 ± 0	0 ± 0	0 ± 0	0 ± 0	0.00 ± ^{0.00} _{0.00}	-15.91 ± 0.02	10424
J0400-52:S2 ^b	271 ± 31	815 ± 85	1150 ± 120	16 ± 9	90 ± 13	63 ± 6	7.27 ± ^{0.70} _{1.60}	-20.02 ± 0.01	11659
J0400-52:S3	1900 ± 620	315 ± 177	7570 ± 830	3020 ± 290	1140 ± 150	794 ± 59	9.23 ± ^{0.07} _{0.07}	-22.82 ± 0.01	11384
J0400-52:S4	305 ± 31	159 ± 33	1430 ± 94	698 ± 53	204 ± 28	154 ± 7	9.21 ± ^{0.04} _{0.04}	-22.71 ± 0.05	9967
J0400-52:S5	1350 ± 120	420 ± 68	6740 ± 300	3100 ± 140	905 ± 60	904 ± 34	9.22 ± ^{0.02} _{0.02}	-22.13 ± 0.06	10790
J0400-52:S6	171 ± 29	81 ± 24	1240 ± 130	476 ± 49	189 ± 22	132 ± 1	9.15 ± ^{0.05} _{0.05}	-18.89 ± 0.13	10287
J0400-52:S7	526 ± 105	456 ± 114	1740 ± 180	423 ± 47	463 ± 63	337 ± 27	9.08 ± ^{0.11} _{0.11}	-17.36 ± 0.08	10607
J0400-52:S8 ^a	51 ± 22	52 ± 32	252 ± 38	119 ± 31	72 ± 13	51 ± 8	8.70 ± ^{0.08} _{0.08}	-17.56 ± 0.07	9921
J0400-52:S9 ^a	89 ± 19	53 ± 48	728 ± 72	365 ± 49	193 ± 34	135 ± 9	8.98 ± ^{0.13} _{0.16}	-22.16 ± 0.21	10287
J1051-17:S1	16 ± 11	31 ± 11	46 ± 11	8 ± 8	4 ± 7	3 ± 0	8.96 ± ^{0.02} _{0.03}	-21.55 ± 0.27	5465
J1051-17:S2	11 ± 2	14 ± 2	139 ± 11	135 ± 10	40 ± 3	30 ± 2	9.21 ± ^{0.03} _{0.03}	-21.85 ± 0.05	5288
J1051-17:S3	167 ± 72	255 ± 82	273 ± 75	101 ± 49	29 ± 16	48 ± 10	9.00 ± ^{0.19} _{0.28}	-16.34 ± 0.09	5969
J1051-17:S4 ^b	94 ± 17	196 ± 29	394 ± 54	15 ± 8	67 ± 11	47 ± 6	7.50 ± ^{0.41} _{0.74}	-17.20 ± 0.06	5465
J1051-17:S5	35 ± 26	60 ± 30	1540 ± 220	176 ± 33	373 ± 51	261 ± 30	8.40 ± ^{0.14} _{0.15}	-16.95 ± 0.04	5465
J1051-17:S6	30 ± 4	55 ± 7	121 ± 15	17 ± 2	19 ± 2	13 ± 2	8.60 ± ^{0.09} _{0.09}	-16.94 ± 0.12	5648
J1051-17:S7	9 ± 1	11 ± 1	32 ± 4	3 ± 0	5 ± 1	4 ± 0	8.42 ± ^{0.10} _{0.11}	-17.48 ± 0.04	5374
J1051-17:S8	28 ± 9	73 ± 17	374 ± 44	200 ± 24	166 ± 20	134 ± 15	8.80 ± ^{0.08} _{0.08}	-16.68 ± 0.05	5294
J1051-17:S9	99 ± 29	109 ± 26	507 ± 70	131 ± 27	176 ± 27	123 ± 15	8.63 ± ^{0.13} _{0.13}	-23.05 ± 0.20	5582
J1403-06:S1	1290 ± 90	301 ± 37	3110 ± 210	1350 ± 90	489 ± 39	359 ± 24	9.20 ± ^{0.03} _{0.03}	-22.74 ± 0.09	2498
J1403-06:S2	1780 ± 160	12900 ± 900	4820 ± 460	5470 ± 500	1310 ± 120	1340 ± 120	9.10 ± ^{0.03} _{0.04}	-22.74 ± 0.10	2727
J1403-06:S3 ^b	600 ± 51	1460 ± 130	1200 ± 170	64 ± 12	209 ± 31	146 ± 21	7.93 ± ^{0.17} _{0.20}	-14.51 ± 0.86	2753
J1403-06:S4 ^b	208 ± 28	233 ± 27	520 ± 86	13 ± 7	78 ± 21	55 ± 9	7.40 ± ^{0.58} _{1.39}	-23.15 ± 0.26	2671
J1408-21:S1	2160 ± 290	878 ± 130	9140 ± 540	4600 ± 280	1080 ± 90	966 ± 75	9.25 ± ^{0.03} _{0.03}	-23.15 ± 0.27	8694
J1408-21:S2	661 ± 76	212 ± 46	2780 ± 189	1050 ± 70	404 ± 37	352 ± 19	9.15 ± ^{0.04} _{0.04}	-20.72 ± 0.10	8821
J1408-21:S3	887 ± 86	258 ± 34	3770 ± 310	1330 ± 120	637 ± 62	505 ± 30	9.10 ± ^{0.04} _{0.05}	-21.23 ± 0.08	8782
J1408-21:S4	202 ± 25	104 ± 31	998 ± 104	393 ± 41	237 ± 27	165 ± 14	9.02 ± ^{0.06} _{0.07}	-13.31 ± 0.52	9126
J1408-21:S5	204 ± 402	428 ± 601	654 ± 284	101 ± 228	119 ± 94	83 ± 13	8.57 ± ^{0.13} _{0.14}	-17.12 ± 0.07	8778
J1408-21:S6 ^c	336 ± 155	15 ± 124	329 ± 127	0 ± 0	0 ± 0	0 ± 0	0.00 ± ^{0.00} _{0.00}	-22.35 ± 0.19	8672
J1956-50:S1	262 ± 61	218 ± 56	1570 ± 180	631 ± 83	172 ± 34	126 ± 15	9.18 ± ^{0.05} _{0.06}	-22.35 ± 0.20	7610
J1956-50:S2	2170 ± 2300	1710 ± 190	7670 ± 720	2110 ± 200	1510 ± 150	1080 ± 100	8.89 ± ^{0.06} _{0.06}	-16.65 ± 0.22	7015
J1956-50:S3	1590 ± 160	10700 ± 900	5070 ± 610	110 ± 20	198 ± 31	139 ± 20	8.24 ± ^{0.16} _{0.15}	-15.15 ± 0.23	6375
J1956-50:S4	242 ± 31	413 ± 55	610 ± 82	59 ± 14	94 ± 14	70 ± 9	8.40 ± ^{0.16} _{0.18}	-21.73 ± 0.29	7472
J2027-51:S1	51 ± 5	47 ± 4	621 ± 33	321 ± 16	134 ± 8	226 ± 14	8.99 ± ^{0.03} _{0.03}	-21.73 ± 0.30	5830
J2027-51:S2	42 ± 3	29 ± 2	980 ± 64	306 ± 20	155 ± 10	166 ± 11	9.01 ± ^{0.04} _{0.04}	-21.91 ± 0.17	5783
J2027-51:S3	1300 ± 140	2740 ± 280	4240 ± 550	623 ± 75	997 ± 121	708 ± 86	8.43 ± ^{0.09} _{0.10}	-17.40 ± 0.15	5830
J2027-51:S4	1740 ± 140	3080 ± 260	5770 ± 660	815 ± 99	1130 ± 130	792 ± 86	8.50 ± ^{0.08} _{0.09}	-22.25 ± 0.26	6013
J2318-42a:S1	8610 ± 500	25400 ± 1000	61900 ± 2100	45100 ± 1400	10300 ± 300	9670 ± 290	9.16 ± ^{0.01} _{0.01}	-22.25 ± 0.27	1461
J2318-42a:S2	583 ± 81	2300 ± 230	5780 ± 480	5170 ± 390	2450 ± 190	2110 ± 130	8.99 ± ^{0.04} _{0.04}	-21.22 ± 0.06	1481
J2318-42a:S3	2890 ± 220	1490 ± 130	13700 ± 1500	3280 ± 430	1800 ± 220	1270 ± 150	9.01 ± ^{0.07} _{0.07}	-20.15 ± 0.29	1777
J2318-42a:S4 ^c	88 ± 24	29 ± 21	213 ± 30	222 ± 15	16 ± 7	34 ± 4	0.00 ± ^{0.00} _{0.00}		1685

Notes. Columns: 1: SINGG name; 2–7: observed (and extinction-corrected fluxes only in electronic version) for various emission lines, in units of 10^{-17} erg s $^{-1}$ cm $^{-2}$; 8: metallicity calibrated using Dopita et al. (2013); 9 SINGG R -band absolute magnitude; and 10: WiFeS heliocentric velocity.

^a TDG candidates.

^b Very metal-poor dwarfs.

^c Metallicity not measurable due to poor signal in one or more lines.

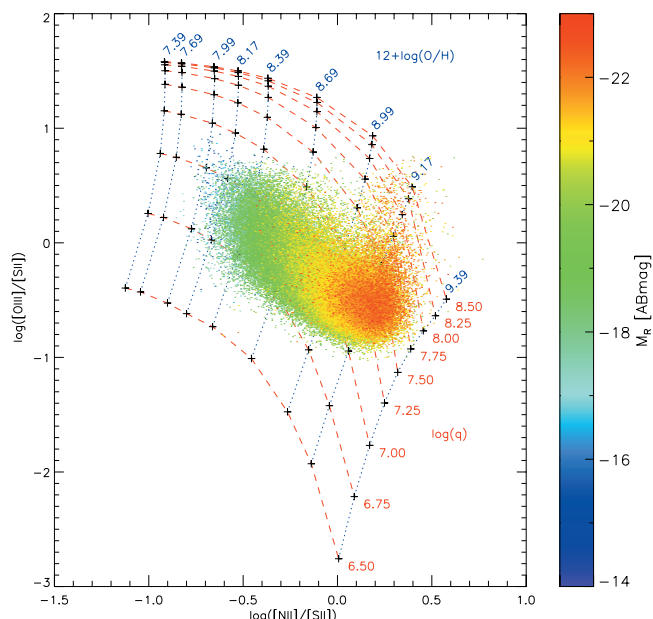


Figure 2. Dopita et al. (2013) metallicity calibration grid for $[\text{O III}]/[\text{S II}]$ vs. $[\text{N II}]/[\text{S II}]$, which illustrates the metallicity calibration for our sample. The red, dashed model curve labels depict $\log(\text{ionization parameter})$, while the blue, dotted model curve labels denote the metallicity. Here we show the galaxies in our SDSS (Aihara et al. 2011) sample, color-coded by magnitude.

(A color version of this figure is available in the online journal.)

$\log [\text{O III}]/[\text{S II}]$ versus $\log [\text{N II}]/[\text{S II}]$ diagnostic given in Dopita et al. (2013, their Figure 21 and our Figures 2 and 3). The diagnostic is useful because it provides a clear separation of the ionization parameter q and metallicity $12+\log(\text{O}/\text{H})$ and is not highly dependent on the value of κ . Following Dopita et al. (2013), we adopt $\kappa = 20$. We use a bivariate polynomial interpolation to convert the diagnostic grid from line-ratio to ionization-parameter–metallicity space using `RMODEL` (Cardiel et al. 2003).⁸ Errors in metallicity for the Choir member galaxies are estimated by `RMODEL` with a Monte Carlo simulation based on errors in the emission-line ratios. The nonregular shape of the calibration model means that the errors are asymmetric. As expected, the errors are generally larger for fainter galaxies and where the metallicity is low (because the low-metallicity region of the grid is the most sensitive to $[\text{N II}]/[\text{S II}]$).

Figure 2 illustrates our nondegenerate metallicity diagnostic with our SDSS control sample, which is presented in the following section. On that control sample, the Dopita et al. (2013) calibration is higher than the hybrid calibration method used in Tremonti et al. (2004) by 0.1–0.2 dex over the relevant magnitude range (see Figure 4). This difference was previously noted in López-Sánchez et al. (2012). Figure 3 also illustrates our metallicity diagnostic, but for our sample of galaxies.

3.2. Control Samples

3.2.1. SDSS

Due to the availability of quality photometry and spectroscopy for 860,000 galaxies, the Sloan Digital Sky Survey Eighth Data Release (SDSS DR8; Aihara et al. 2011) is an ideal catalog from which to draw our bright-galaxy comparison sample. Following Tremonti et al. (2004), we restrict our SDSS sample to a selection of high-confidence detections. The selection limits

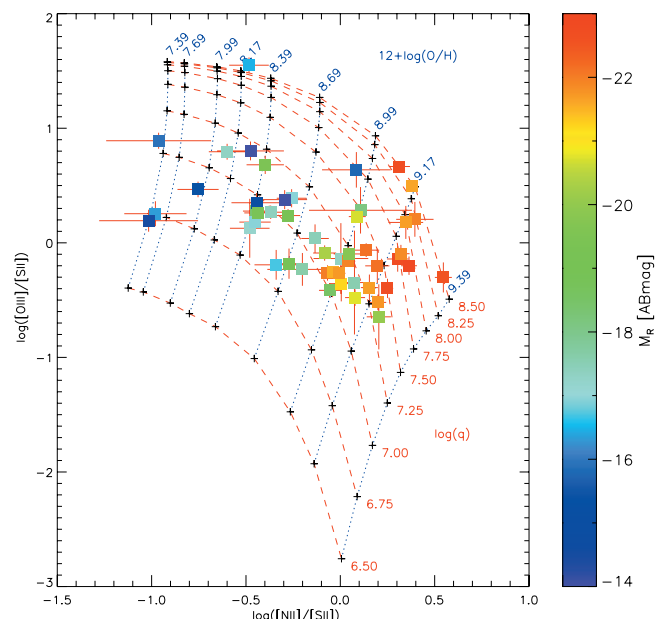


Figure 3. As above, for our sample of galaxies in gas-rich Choir groups. (A color version of this figure is available in the online journal.)

are as follows: $0.005 < z < 0.25$; $>5\sigma$ detection in each of $\text{H}\beta$, $[\text{O III}]$, $\text{H}\alpha$, $[\text{N II}]$, and $[\text{S II}]$; $\log([\text{O III}]/\text{H}\beta) < 0.61/(\log([\text{N II}]/\text{H}\alpha) - 0.05) + 1.3$ (to exclude active galactic nucleus, following Kauffmann et al. 2003); classified as a galaxy; $\sigma_z < 0.15$; $\sigma_{H\delta} < 2.5$; $\sigma_{Dn(4000)} < 0.1$. These parameters ensure that our SDSS sample is consistent with the Tremonti sample and clean of most spurious detections. Further, we visually inspected the 300 faintest ($M_R > -16$ mag) galaxies and excluded 30 H II regions which were incorrectly classified as galaxies. Most of these have high metallicity (~ 8.6 – 9.0) corresponding to the parent galaxy, but all of them have faint magnitudes corresponding to the local H II region, so cannot be included in the luminosity–metallicity relation. Our resulting SDSS sample contains 94,863 sources.

We then converted SDSS r -band absolute magnitudes to SINGG R -band AB absolute magnitudes using the r_{SDSS} to R_{Vega} transformation by Robert Lupton⁹ and the R_{Vega} to R_{AB} Deep Lens Survey transformation.¹⁰ We consider that the r -band SDSS to AB magnitude correction is small compared with the scatter in the r_{SDSS} to R_{Vega} conversion,¹¹ so we adopt the final conversion $M_{R(\text{AB})} = M_{r(\text{SDSS})} - 0.1837(g_{\text{SDSS}} - r_{\text{SDSS}}) + 0.0829$.

Using the methods described above, we performed reddening corrections and metallicity calibrations for this sample.

We plot the luminosity–metallicity relation for our SDSS sample in Figure 4. We attempt to model the luminosity–metallicity relation for SDSS using some common approaches in the literature: linear, piece-wise linear, polynomial, and asymptotic fits (Tremonti et al. 2004; Kewley & Ellison 2008; Mannucci et al. 2010; Sanchez et al. 2013). It is qualitatively evident that none of these models fit the data very well, particularly at faint and/or very bright magnitudes.

Moreover, a clear turnover, or knee, can be seen in the luminosity–metallicity relation. The poorness of the traditional fits together with the hint of multiple populations motivate us to

⁹ <http://www.sdss.org/dr5/algorithms/sdssUBVRITransform.html>

¹⁰ <http://dls.physics.ucdavis.edu/calib/vegaab.html>

¹¹ <http://www.sdss.org/dr5/algorithms/fluxcal.html#sdss2ab>

⁸ <http://www.ucm.es/info/Astrof/software/rmodel/rmodel.html>

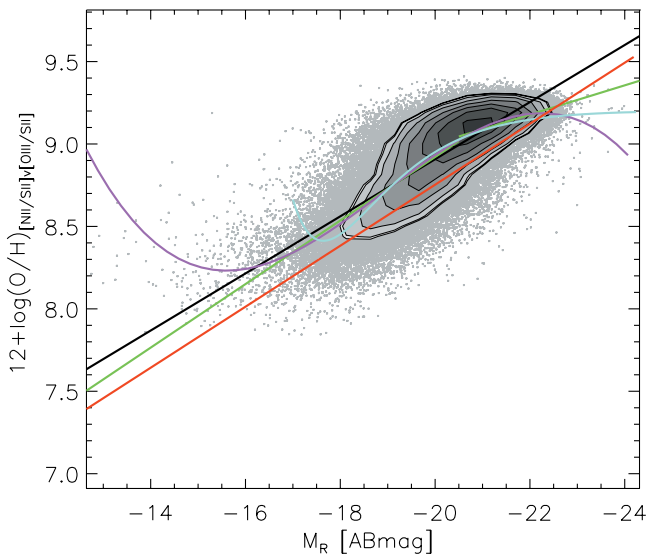


Figure 4. Luminosity–metallicity relation for our SDSS control sample—gray points and grayscale contours. We overlay various fits: linear = black, piecewise linear = green, cubic = magenta, asymptotic = cyan, Tremonti linear = red. The linear fit using the Dopita et al. (2013) calibration is 0.1–0.2 dex above the Tremonti et al. (2004) fit.

(A color version of this figure is available in the online journal.)

perform Gaussian mixture modeling, which identifies subpopulations (“clusters”) in multidimensional data with a maximum likelihood approach. In particular, we use the unsupervised, optimal, fuzzy-clustering algorithm described by Gath & Geva (1989), varying the number of clusters, k . It is common to measure the goodness of fit by the density of each cluster (number of members near the center of a cluster divided by its total number of members), but as k increases toward the sample size, the density of each cluster increases, so the fit becomes increasingly good. Instead, to avoid overfitting, we calculate the “average partition density” as defined by Gath & Geva (1989), where cluster density is normalized to the number of clusters, k . We plot this as our figure of merit in Figure 5; a larger average partition density represents a better fit. Clearly, the optimum number of clusters is $k = 2$. We plot the 1σ , 2σ , and 3σ ellipses for these two subpopulations in Figure 6. There is a metal-rich ($12 + \log(\text{O}/\text{H}) = 9.1$), “giant” ($M_R = -20.7$) subpopulation, containing 52% of the sample, and a metal-medium ($12 + \log(\text{O}/\text{H}) = 8.5$), “medium+dwarf” ($M_R = -19.5$) subpopulation with the remaining 48%. The overlap in luminosity–metallicity space suggests that there are other dimensions that may distinguish between the subpopulations, such as the ionization parameter q . The fact that the knee is also seen in the calibration grid in Figure 2 lends support to this idea. Here, low-luminosity galaxies (blue-green; $M_R \lesssim -21$) have increasing metallicities but fairly constant ionization parameters ($\log q \sim 6.7\text{--}7$), whereas brighter galaxies (yellow-red; $M_R \gtrsim -21$) have increasing metallicities and increasing ionization parameters (up to $\log q = 8$). This combination of increasing metallicity and ionization parameter was also found in a spaxel analysis of a sample of luminous infrared galaxies by Dopita et al. (2014).

At magnitudes brighter than $M_R \sim -16$, SDSS is an ideal control sample due to the volume and quality of the data (see Figure 6). At magnitudes fainter than $M_R \sim -16$, there are two possible concerns with the SDSS control sample, which we address here. (1) There is an apparent metallicity

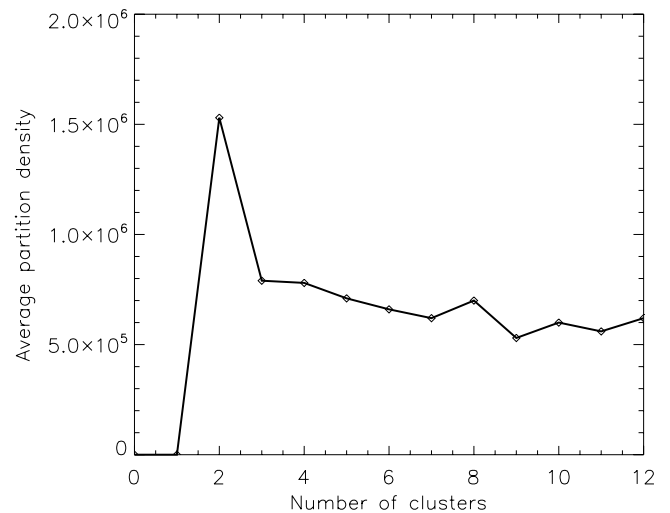


Figure 5. Figure of merit showing goodness of fit as a function of number of subpopulations (“clusters”) fitted for in our SDSS control sample. The goodness of fit is measured by average partition density, which is defined as the sum of memberships near centers divided by the volume of clusters, normalized to the number of clusters. The optimum number of clusters is clearly two.

floor to the SDSS population, with no metallicities lower than approximately $12 + \log(\text{O}/\text{H}) = 7.9$. For SDSS dwarfs fainter than $M_R \sim -16$, metallicity is constant with luminosity, with a mean of $12 + \log(\text{O}/\text{H}) = 8.28 \pm 0.10$. We note that this floor is also seen (albeit less obviously, due to different figure scales and limits) in Tremonti et al. (2004) and Figure 21 of Dopita et al. (2013). This floor is not an artifact of the metallicity calibration, because the calibration is well defined down to $12 + \log(\text{O}/\text{H}) = 7.39$ and is not degenerate. Moreover, the floor is not absolute since we observe Choir (and other) galaxies below this metallicity, and these are calibrated using the same method. Finally, the metallicity floor cannot be explained by selection effects. Although one may consider low-surface-brightness dwarfs, with few H II regions and low metallicities, to be selected against in our sample due to low signal-to-noise ratios, we see the same floor even without signal-to-noise cuts. We point out that the floor could be an artifact of the aperture effect in SDSS, whereby faint, nearby objects are large in angular size compared with the fibers. The SDSS measurements are consequently of nuclear spectra for these galaxies, which are higher than the mean galaxy abundance due to galactic abundance gradients. We therefore consider for this analysis that it is probably a true lower limit for the nuclei of typical galaxies, and we will investigate the floor further in a future work. The exceptions to this limit are discussed in Section 4. (2) There is an increased dispersion in metallicity at magnitudes fainter than $M_R \sim -16$. The SDSS sample is selected to only contain high-confidence detections, so the dispersion is a physical dispersion in the galaxies, rather than caused by measurement error. We conclude that the SDSS sample is therefore of sufficient quality to act as a control sample for our population of dwarfs fainter than $M_R \sim -16$.

3.2.2. Additional Dwarf Galaxy Control Samples

We now turn to a number of other samples for which [O III], [N II], and [S II] data are available. Where $\text{H}\alpha$ and $\text{H}\beta$ are also available and the observed fluxes are given, we apply the same reddening correction as for the Choirs and SDSS samples. Where these are unavailable, we adopt the dereddened fluxes

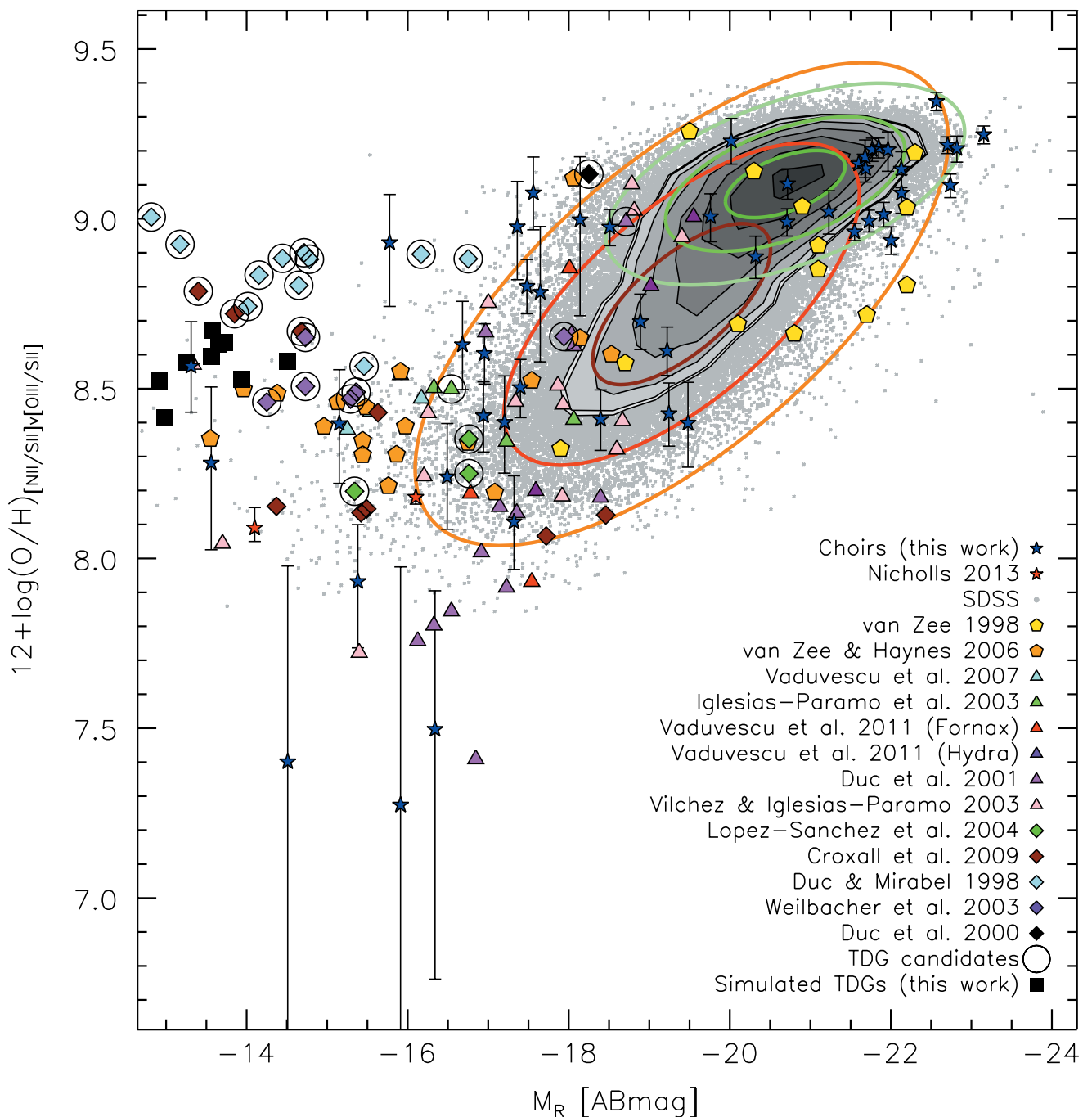


Figure 6. Luminosity–metallicity relation for our SDSS control sample, with Gaussian mixture modeling overlaid; the two subpopulations are shown in red and green 1σ , 2σ , and 3σ ellipses. Choir galaxies are shown in blue stars. Other dwarf galaxies in the literature are also shown: pentagons denote isolated galaxies, triangles denote gas-rich galaxies, and diamonds denote dwarf galaxies very near a host. TDG candidates are circled; on average, these are elevated above the normal relation defined by the SDSS sample. We also show our TDGs from our hydrodynamical simulations as black squares. Our Choir galaxies have a wide range in metallicity; three of these are significantly above the normal SDSS relation and are therefore strong TDG candidates.

(A color version of this figure is available in the online journal.)

given by the authors. Where necessary, we convert from B - or K -band magnitudes, assuming typical colors $B - R \approx 1$ and $R - K \approx 2$ (Binney & Merrifield 1998).

We include two dwarfs from the small, isolated, gas-rich, irregular dwarf-galaxy sample (SIGRID, Nicholls et al. 2011), which have also been measured with the WiFeS integral field spectrograph. Full details are presented in Nicholls et al. (2014). We include additional H II regions and isolated dwarfs from van

Zee et al. (1998) and van Zee & Haynes (2006). For each galaxy in these three samples, we sum over the emission-line fluxes measured in all of the H II regions within that galaxy before calculating line ratios and interpolating to metallicity as before. Our tests show that this gives the same result as averaging the metallicities for each H II region, consistent to within ± 0.05 dex. The integrated metallicities are then plotted against total galaxy luminosities.

The SIGRID dwarfs are plotted as red stars in Figure 6. Both of these (KK[98] 246 and HIPASS J1609-04) are consistent with the SDSS sample.

The van Zee et al. (1998) and van Zee & Haynes (2006) galaxies are shown as pentagons in Figure 6. The bright galaxies are consistent with the SDSS sample, but the faint end is elevated in metallicity above SDSS at a constant metallicity with luminosity ($12 + \log(\text{O}/\text{H}) = 8.46 \pm 0.04$). We note that Figure 21 of Dopita et al. (2013) also indicates a similar discrepancy between SDSS and the van Zee & Haynes (2006) sample. At the low-metallicity end of the diagnostic, the metallicity is almost entirely determined by the $[\text{N II}]/[\text{S II}]$ ratio. This means that metallicities are dependent on the assumed relationship between N/O and $12 + \log(\text{O}/\text{H})$. The N/O relationship has been recalibrated for the Dopita et al. (2013) model grids, so metallicities measured with these models will be offset from metallicities measured with earlier models. However, we have used the recalibrated model for all of the samples in this analysis, so this recalibration of N/O does not cause the elevation of the van Zee et al. (1998) and van Zee & Haynes (2006) samples over SDSS.

We plot dwarf galaxies belonging to various local clusters as triangles in Figure 6: Virgo (Vaduvescu et al. 2007; Vílchez & Iglesias-Páramo 2003), Hercules (Iglesias-Páramo et al. 2003), Fornax (Vaduvescu et al. 2011), and Hydra (Vaduvescu et al. 2011; Duc et al. 2001). In general, these objects tend toward lower metallicity with faint luminosity. Vaduvescu et al. (2007) found that the H I-gas richness of dwarfs has an effect on their metallicity. This is borne out by the general trend of these gas-rich cluster dwarfs (particularly the Hydra dwarfs in Duc et al. 2001) toward very low metallicities, compared with the isolated samples, which are not gas rich.

Finally, we also include a selection of dwarfs in groups, plotted as diamonds: NGC 5291 (Duc & Mirabel 1998) and Arp245N (Duc et al. 2000) (both in pairs), the compact group HCG31 (López-Sánchez et al. 2004), the larger ~ 30 member group M81 (Croxall et al. 2009), and various other interacting systems (Weilbacher et al. 2003).

4. DISCUSSION

4.1. Tidal Dwarf Galaxies

TDGs are expected to have high metallicities corresponding to the pre-enriched material from which they form. They should also be formed within a tidal tail (which may or may not be sufficiently bright to observe), without a DM halo, and may be located near their parent giant galaxy (depending on the time since formation, e.g., Duc et al. 2000; Weilbacher et al. 2003). Here, we use the luminosity–metallicity relation to identify candidate TDG galaxies for later follow-up.

A number of the galaxies from the existing literature shown in Figure 6 are claimed by their authors to be TDG candidates (circled points). As for the isolated dwarf sample, these TDG candidates do not display an increasing metallicity with luminosity, but they differ from the isolated dwarf sample by showing an enhanced average metallicity ($12 + \log(\text{O}/\text{H}) = 8.70 \pm 0.05$). While some of them are clearly elevated above the luminosity–metallicity relation of SDSS bright galaxies and van Zee & Haynes (2006) isolated dwarfs (e.g., Arp245N, black diamond, Duc et al. 2000), many are consistent with the SDSS control sample (e.g., HCG31 TDG candidates, dark green diamonds, López-Sánchez et al. 2004). The overlap between isolated dwarfs (non-TDGs) and previously identified TDG

candidates is partly due to the fact that some of those TDG candidates were identified because they have a higher metallicity than normal/isolated dwarfs using different metallicity calibrations. This overlap therefore simply confirms that using different methods to measure metallicity will give different results.

4.2. Simulations

We have conducted hydrodynamical simulations of TDG candidates, the full details of which will be given in K. Bekki et al. (2013, in preparation); brief details follow. We model a Milky Way type disk galaxy with a total dark-halo mass of $10^{12} M_{\odot}$, a stellar mass of $6 \times 10^{10} M_{\odot}$, bulge mass of $10^{10} M_{\odot}$, and gas mass of $3 \times 10^{10} M_{\odot}$. The adopted initial (stellar and gas-phase) metallicity gradient is $-0.08 \text{ dex kpc}^{-1}$, with nuclear stellar metallicity of $[\text{Fe}/\text{H}] = 0.34 \text{ dex}$ and gas-phase metallicity $12 + \log(\text{O}/\text{H}) = 9.04$. The Milky Way type disk galaxy is assumed to interact with a companion galaxy with the same total mass represented by a point-mass particle. The orbit of the two interacting galaxies is assumed to be hyperbolic with an initial distance of 280 kpc, orbital eccentricity of 1.1, and pericenter distance of 70 kpc. We select TDG candidates from the remnants of the interacting Milky Way type disks as follows. We identify the newly formed stars in our simulation. For each new star, we determine the number of additional new stars within 1 kpc, N_{ns} . For a region with $N_{\text{ns}} > 100$, the total mass of the region is $M \geq 3 \times 10^7 M_{\odot}$, so the stars in that region are considered to belong to a TDG candidate. For each selected TDG candidate, the center of mass is estimated by using all new stars within 1 kpc of the new star. The total mass and the mean gas-phase metallicity within 1 kpc from the center of mass are then calculated for the TDG candidate. We assumed an *R*-band mass-to-light ratio of $M/L_R = 0.86$ for a stellar population of mean age 1 Gyr and solar metallicity, using the MILES code by Vazdekis et al. (2010). Our simulated data are shown in Figure 6 as black, filled squares. The mean simulated metallicity is 8.57 ± 0.03 , within 3σ of the mean observed TDG candidate metallicity of 8.70 ± 0.05 .

4.3. Choir Dwarf Galaxies: Tidal Dwarf Candidates, Normal Dwarfs, and Very-metal-poor Dwarfs

The Choir giants ($M_R \lesssim -20$) are in reasonable agreement with the SDSS giant subpopulation, having the same metallicity, though being around one magnitude more luminous. The medium–luminosity Choir dwarfs ($-16 \lesssim M_R \lesssim -20$) are also mostly consistent with the SDSS medium-dwarf subpopulation. The contours provide a simple diagnostic of the significance of any outlying results. For example, we consider that the two most metal-rich dwarfs at $M_R \sim -17.5$, being more than 3σ from the mean SDSS medium-dwarf population, are bonafide TDG candidates.

Compared with each of the additional samples of dwarfs listed above, Choir galaxies have an increased scatter at the low-luminosity end, spanning the full 1.5 dex metallicity range observed for all types of dwarfs. Some groups (e.g., HIPASS J0400-52) even span this range. The size of the error bars compared with the scatter suggests that this is not a measurement error, but either due to the calibration model or a true dispersion in the population. Figure 3 of Dopita et al. (2013) illustrates with van Zee et al. (1998) H II regions an increased scatter in metallicities between $8.0 \lesssim 12 + \log(\text{O}/\text{H}) \lesssim 8.5$ measured using this model. The metallicity calibration for these galaxies

depends very strongly on the calibration between $\log(N/O)$ and $\log(O/H)$, as demonstrated in that figure. However, the observed dispersion is much greater in the Choir sample than in the van Zee et al. (1998) and other comparison samples, so we consider that the Choir dwarf galaxy population is inherently dispersed. We expect that this is due to a wide variation in gas content and environment (distance to host) of the Choir member galaxies.

We consider that (1) the three Choir dwarfs (J0205-55:S7, J0400-52:S8, J0400-52:S9) with metallicity above $12 + \log(O/H) = 8.6$ (3σ above the SDSS dwarfs) and above the SDSS 3σ medium-dwarf ellipse are strong TDG candidates (these candidates represent 16% of the Choir dwarfs fainter than $M_R = -18$); (2) the dwarfs between $8.0 \lesssim 12 + \log(O/H) \lesssim 8.6$ and within the SDSS 3σ dwarf ellipse are most likely normal galaxies but still are possible TDGs; and (3) the dwarfs (J0400-52:S2, J1051-17:S4, J1403-06:S3, J1403-06:S4) with metallicity less than 8.0 are probably the most gas rich in our sample due to their similarity (in metallicity–luminosity space) to the gas-rich Hydra dwarfs in Duc et al. (2001) and the gas-rich HIPASS J1609-04. The very-metal-poor sample represents 21% of the Choir dwarfs fainter than $M_R = -18$. It could be that these very-metal-poor dwarfs in our sample have acquired large amounts of relatively pristine H I gas and have had star formation reignited, due to recent interactions with the nearby giant galaxies (e.g., Kannappan et al. 2013). We note that Skillman et al. (2013) suggest the most metal-poor dwarfs may become metal poor due to H I gas inflowing to their central star-forming regions. Our TDG candidates and metal-poor dwarfs are noted in Table 2.

We are conducting a follow-up analysis of the kinematics and masses of our TDG candidates to determine which are bonafide TDGs, and a further analysis of the importance of environmental location and gas content (S. M. Sweet et al., in preparation).

5. CONCLUSIONS AND FUTURE WORK

In this paper, we have used the new Dopita et al. (2013) metallicity calibrations to calibrate the luminosity–metallicity relation for a range of galaxy types. Importantly, we used the same calibration for our population of galaxies in H I-rich groups as for our control samples.

We make the following points.

1. In metallicity–luminosity space, we find two subpopulations, or clusters, within the SDSS sample. The cluster of metal-rich giants represents 52% of the sample, while the remaining 48% are metal-poor dwarfs.
2. There is an apparent floor to the metallicity of SDSS dwarfs at $12 + \log(O/H) = 7.9$; the mean metallicity for SDSS dwarfs fainter than $M_R = -16$ is $12 + \log(O/H) = 8.28 \pm 0.10$.
3. Isolated dwarf galaxies appear to have a constant metallicity with magnitude of $12 + \log(O/H) = 8.46 \pm 0.04$, similar to the SDSS dwarf sample.
4. On average, TDG candidates from the literature have a metallicity of $12 + \log(O/H) = 8.70 \pm 0.05$, significantly elevated above SDSS galaxies. Our simulated TDGs are slightly less metal rich than TDG candidates in the literature at $12 + \log(O/H) = 8.57 \pm 0.03$, but still significantly more metal rich than typical dwarfs.
5. Gas-rich cluster dwarfs trend toward lower metallicity than their isolated counterparts, where Hydra dwarfs from Duc et al. (2001) have the lowest metallicity of our

comparison samples, suggesting that dwarf metallicity is highly dependent on group membership.

6. At medium-bright magnitudes, our sample of star-forming galaxies in groups is consistent with SDSS.
7. At faint luminosity, there is an increased dispersion in the metallicity of our sample, indicating a wide range of H I content and environmental location.
8. Based on metallicity, we identify three (16% of dwarfs) strong TDG candidates ($12 + \log(O/H) > 8.6$), which have metallicities consistent with both other TDG candidates in the literature and our simulations, and significantly above the SDSS control sample at $12 + \log(O/H) = 8.28 \pm 0.10$. These galaxies are J0205-55:S7, J0400-52:S8, and J0400-52:S9 and are discussed very briefly in Appendix A.1.
9. We also identify four (21%) very-metal-poor galaxies ($12 + \log(O/H) < 8.0$), consistent with gas-rich cluster dwarfs whose star formation has been ignited due to interactions with nearby giant galaxies. These galaxies are J0400-52:S2, J1051-17:S4, J1403-06:S3, and J1403-06:S4 and are discussed very briefly in Appendix A.2.

To conclude, metallicity can be an important diagnostic for identifying preliminary populations of candidate TDGs. Other factors such as environment, as noted by Vaduvescu et al. (2007), may also influence metallicity, so careful follow-up is required before declaring the candidates to be bonafide TDGs.

The authors thank the anonymous referee for a constructive report which improved the clarity of this paper.

We thank David Rohde for helpful discussions about Gaussian mixture modeling, and Jeff Rich, Mort Canty, and James R. A. Davenport for providing IDL routines. We acknowledge funding support from the UQ-UWA Bilateral Research Collaboration Award.

This research has made use of NASA’s Astrophysics Data System.

This research has made use of the NASA/IPAC Extragalactic Database (NED), which is operated by the Jet Propulsion Laboratory, California Institute of Technology, under contract with the National Aeronautics and Space Administration.

APPENDIX

NOTES ON STRONG TDG CANDIDATES AND VERY-METAL-POOR DWARFS

A.1. Strong Tidal Dwarf Galaxy Candidates

A.1.1. HIPASS J0205-55:S7

This dwarf is located in Choir group HIPASS J0205-55, which appears to be comprised of two merging systems (Sweet et al. 2013). The nearest bright neighbor to S7 is S2, approximately 50 kpc away in projection. S7 has the morphology of a symmetric, edge-on disk galaxy with a half-light radius of 0.85 kpc.

A.1.2. HIPASS J0400-52:S8 and S9

These dwarfs are very compact with half-light radii of 1.5 and 2.5 kpc, respectively. They are very close companions to S4 and S6, at only 20 kpc away in projection from their respective nearest giant galaxies. This Choir group is part of A3193.

A.2. Very-metal-poor dwarfs

A.2.1. HIPASS J0400-52:S2

This dwarf, approximately 100 kpc from its nearest neighbor, S1, has a half-light radius of 1.3 kpc and is comprised of two abutting low-surface-brightness knots.

A.2.2. HIPASS J1051-17:S4

S4 is located about 100 kpc from giant galaxy S1 in the direction of the second-brightest spiral in the group, S2. It may have gained some H I gas and had star formation reignited during a recent encounter with S1 (V. Kilborn et al., in preparation). It consists of two faint H II regions in a low-surface-brightness host with a half-light radius of 1.4 kpc.

A.2.3. HIPASS J1403-06:S3 and S4

These two quite compact dwarfs are the two faintest members in this Choir group. Both are located about 50 kpc from the nearby giant S1, which itself is currently interacting with the other giant in the group, S2. The interacting pair S1 and S2 is known as Arp 271. The two dwarfs each consist of a single H II region in a low-surface-brightness host, with half-light radii of 0.7 and 1.2 kpc for S3 and S4, respectively.

REFERENCES

- Aihara, H., Allende Prieto, C., An, D., et al. 2011, *ApJS*, 193, 29
 Barnes, D. G., Staveley-Smith, L., de Blok, W. J. G., et al. 2001, *MNRAS*, 322, 486
 Binney, J., & Merrifield, M. 1998, *Galactic Astronomy* (Princeton, NJ: Princeton Univ. Press)
 Bournaud, F. 2010, *AdAst*, 2010, 1
 Brodie, J. P., & Huchra, J. P. 1991, *ApJ*, 379, 157
 Bruzual, G., & Charlot, S. 2003, *MNRAS*, 344, 1000
 Cardiel, N., Gorgas, J., Sánchez Blázquez, P., et al. 2003, *A&A*, 409, 511
 Croxall, K. V., van Zee, L., Lee, H., et al. 2009, *ApJ*, 705, 723
 Dalcanton, J. J. 2007, *ApJ*, 658, 941
 Dopita, M., Hart, J., McGregor, P., et al. 2007, *Ap&SS*, 310, 255
 Dopita, M., Rhee, J., Farage, C., et al. 2010, *Ap&SS*, 327, 245
 Dopita, M. A., Rich, J., Vogt, F. P. A., et al. 2014, *Ap&SS*, in press (arXiv:1312.4633D)
 Dopita, M. A., Sutherland, R. S., Nicholls, D. C., Kewley, L. J., & Vogt, F. P. A. 2013, *ApJS*, 208, 10
 Duc, P. A., Brinks, E., Springel, V., et al. 2000, *AJ*, 120, 1238
 Duc, P. A., Cayatte, V., Balkowski, C., et al. 2001, *A&A*, 369, 763
 Duc, P.-A., & Mirabel, I. F. 1998, *A&A*, 333, 813
 Esteban, C., Peimbert, M., Torres-Peimbert, S., & Escalante, V. 1998, *MNRAS*, 295, 401
 Garcia, A. 1993, *A&AS*, 100, 47
 Garnett, D. R., & Shields, G. A. 1987, *ApJ*, 317, 82
 Gath, I., & Geva, A. B. 1989, *ITPAM*, 11, 773
 Gibson, B. K., & Matteucci, F. 1997, *ApJ*, 475, 47
 Hickson, P., Kindl, E., & Auman, J. R. 1989, *ApJS*, 70, 687
 Hunsberger, S. D., Charlton, J. C., & Zaritsky, D. 1996, *ApJ*, 462, 50
 Iglesias-Páramo, J., van Driel, W., Duc, P. A., et al. 2003, *A&A*, 406, 453
 Kannappan, S. J., Stark, D. V., Eckert, K. D., et al. 2013, *ApJ*, 777, 42
 Kauffmann, G., Heckman, T. M., Tremonti, C., et al. 2003, *MNRAS*, 346, 1055
 Kewley, L. J., & Dopita, M. A. 2002, *ApJS*, 142, 35
 Kewley, L. J., & Ellison, S. L. 2008, *ApJ*, 681, 1183
 Kobulnicky, H. A., & Skillman, E. D. 1997, *ApJ*, 489, 636
 Lee, H., & Skillman, E. D. 2004, *ApJ*, 614, 698
 Lequeux, J., Peimbert, M., Rayo, J. F., Serrano, A., & Torres-Peimbert, S. 1979, *A&A*, 80, 155
 López-Sánchez, Á. R., Dopita, M. A., Kewley, L. J., et al. 2012, *MNRAS*, 426, 2630
 López-Sánchez, Á. R., Esteban, C., García-Rojas, J., Peimbert, M., & Rodríguez, M. 2007, *ApJ*, 656, 168
 López-Sánchez, Á. R., Esteban, C., & Rodríguez, M. 2004, *ApJS*, 153, 243
 Mannucci, F., Cresci, G., Maiolino, R., Marconi, A., & Gnerucci, A. 2010, *MNRAS*, 408, 2115
 McGaugh, S. S. 1991, *ApJ*, 380, 140
 Meurer, G. R., Hanish, D. J., Ferguson, H. C., et al. 2006, *ApJS*, 165, 307
 Mirabel, I. F., Dottori, H., & Lutz, D. 1992, *A&A*, 256, L19
 Nicholls, D., Jerjen, H., Dopita, M., & Basurah, H. 2014, *ApJ*, 780, 88
 Nicholls, D. C., Dopita, M. A., Jerjen, H., & Meurer, G. R. 2011, *AJ*, 142, 83
 Nicholls, D. C., Dopita, M. A., & Sutherland, R. S. 2012, *ApJ*, 752, 148
 Nicholls, D. C., Dopita, M. A., Sutherland, R. S., Kewley, L. J., & Palay, E. 2013, *ApJS*, 207, 21
 Pagel, B. E. J., Edmunds, M. G., Blackwell, D. E., Chun, M. S., & Smith, G. 1979, *MNRAS*, 189, 95
 Peimbert, M., & Costero, R. 1969, *BAAS*, 1, 256
 Rich, J. A., Dopita, M. A., Kewley, L. J., & Rupke, D. S. N. 2010, *ApJ*, 721, 505
 Sanchez, S. F., Rosales-Ortega, F. F., Jungwiert, B., et al. 2013, *A&A*, 554, 58
 Skillman, E. D., Kennicutt, R. C., & Hodge, P. W. 1989, *ApJ*, 347, 875
 Skillman, E. D., Salzer, J. J., Berg, D. A., et al. 2013, *AJ*, 146, 3
 Stasińska, G. 1978, *A&A*, 66, 257
 Stasińska, G. 2005, *A&A*, 434, 507
 Sweet, S. M., Meurer, G., Drinkwater, M. J., et al. 2013, *MNRAS*, 433, 543
 Tremonti, C. A., Heckman, T. M., Kauffmann, G., et al. 2004, *ApJ*, 613, 898
 Vaduvescu, O., Kehrig, C., Vilchez, J. M., & Unda-Sanzana, E. 2011, *A&A*, 533, 65
 Vaduvescu, O., McCall, M. L., & Richer, M. G. 2007, *AJ*, 134, 604
 van Zee, L., & Haynes, M. P. 2006, *ApJ*, 636, 214
 van Zee, L., Salzer, J. J., Haynes, M. P., O'Donoghue, A. A., & Balonek, T. J. 1998, *AJ*, 116, 2805
 Vazdekis, A., Sánchez-Blázquez, P., Falcón-Barroso, J., et al. 2010, *MNRAS*, 404, 1639
 Vilchez, J. M., & Iglesias-Páramo, J. 2003, *ApJS*, 145, 225
 Vogt, F. P. A., Dopita, M. A., & Kewley, L. J. 2013, *ApJ*, 768, 151
 Weillbacher, P. M., Duc, P.-A., & Fritze-v. Alvensleben, U. 2003, *A&A*, 397, 545
 Zahid, H. J., Bresolin, F., Kewley, L. J., Coil, A. L., & Davé, R. 2012, *ApJ*, 750, 120
 Zaritsky, D., Kennicutt, R. C. J., & Huchra, J. P. 1994, *ApJ*, 420, 87

ERRATUM: “CHOIRS H I GALAXY GROUPS: THE METALLICITY OF DWARF GALAXIES” (2014, *ApJ*, 782, 35)

SARAH M. SWEET¹, MICHAEL J. DRINKWATER¹, GERHARDT MEURER^{2,3}, KENJI BEKKI^{2,3},
MICHAEL A. DOPITA^{4,5,6}, VIRGINIA KILBORN⁷, AND DAVID C. NICHOLLS⁴

¹ School of Mathematics and Physics, University of Queensland, QLD 4072, Australia; sarah@sarahsweet.com.au

² School of Physics, University of Western Australia, 35 Stirling Highway, Crawley, WA 6009, Australia

³ International Centre for Radio Astronomy Research, ICRAR M468, 35 Stirling Highway, Crawley, WA 6009, Australia

⁴ Research School of Astronomy and Astrophysics, Australian National University, Cotter Road, Weston ACT 2611, Australia

⁵ Astronomy Department, King Abdulaziz University, P.O. Box 80203, Jeddah, Saudi Arabia

⁶ Institute for Astronomy, University of Hawaii, 2680 Woodlawn Drive, Honolulu, HI 96822, USA

⁷ Swinburne University of Technology, Mail number H30, P.O. Box 218, Hawthorn, Victoria 3122, Australia

Received 2014 March 9; published 2014 April 16

Column 9 of Table 2 (R -band magnitude) has been updated to reflect the correct values. Note that the analysis is based on the correct values, so remains unchanged.

Table 2
Measured Emission Line Fluxes and Other Quantities

HIPASS+	H β	[O III]	H α	[N II]	[S II]	[S II]	12+log(O/H)	M_R	V_{hel}
(1)	(2)	(3)	(4)	(5)	(6)	(7)	(8)	(9)	(10)
J0205–55:S1	1560 ± 140	337 ± 85	6000 ± 378	3110 ± 200	531 ± 51	371 ± 23	9.35 $^{+0.03}_{-0.03}$	–22.57 ± 0.22	6490
J0205–55:S2	9110 ± 810	13500 ± 1200	29300 ± 3000	4590 ± 490	5120 ± 490	3630 ± 340	8.61 $^{+0.07}_{-0.07}$	–19.22 ± 0.00	5941
J0205–55:S3	423 ± 119	436 ± 116	2680 ± 340	1390 ± 190	348 ± 80	243 ± 30	9.20 $^{+0.05}_{-0.06}$	–21.96 ± 0.02	6074
J0205–55:S4	417 ± 64	425 ± 53	1740 ± 113	943 ± 62	665 ± 46	465 ± 24	8.94 $^{+0.04}_{-0.04}$	–22.00 ± 0.09	5941
J0205–55:S5 ^a	1100 ± 390	873 ± 369	1220 ± 290	154 ± 348	0 ± 0	0 ± 0	0.00 $^{+0.00}_{-0.00}$	–17.32 ± 0.18	6216
J0205–55:S6	629 ± 88	1470 ± 180	2220 ± 240	339 ± 42	563 ± 55	394 ± 35	8.41 $^{+0.09}_{-0.09}$	–18.40 ± 0.06	5758
J0205–55:S7 ^b	186 ± 139	951 ± 170	855 ± 141	413 ± 108	206 ± 87	144 ± 16	8.93 $^{+0.14}_{-0.19}$	–15.78 ± 1.08	5758
J0205–55:S8	1420 ± 190	738 ± 190	1750 ± 270	369 ± 129	327 ± 61	229 ± 32	8.78 $^{+0.19}_{-0.20}$	–17.65 ± 0.05	5891
J0205–55:S9	399 ± 28	1520 ± 140	1330 ± 200	93 ± 12	167 ± 23	117 ± 16	8.28 $^{+0.22}_{-0.26}$	–15.37 ± 0.12	6120
J0258–74:S1	1290 ± 130	789 ± 75	5760 ± 610	1880 ± 220	815 ± 84	596 ± 56	9.08 $^{+0.05}_{-0.06}$	–22.13 ± 0.26	4883
J0258–74:S2	864 ± 99	2560 ± 290	2920 ± 440	250 ± 41	371 ± 58	260 ± 40	8.40 $^{+0.12}_{-0.13}$	–19.48 ± 0.29	4883
J0258–74:S3	451 ± 45	226 ± 24	2620 ± 230	983 ± 89	668 ± 61	505 ± 46	8.98 $^{+0.05}_{-0.05}$	–18.51 ± 0.56	4655
J0258–74:S4	1020 ± 100	3700 ± 340	3490 ± 510	175 ± 29	403 ± 59	303 ± 42	8.11 $^{+0.14}_{-0.14}$	–17.32 ± 0.85	4838
J0400–52:S1 ^a	280 ± 31	4720 ± 520	0 ± 0	0 ± 0	0 ± 0	0 ± 0	0.00 $^{+0.00}_{-0.00}$	–21.90 ± 0.06	10424
J0400–52:S2 ^c	271 ± 31	815 ± 85	1150 ± 120	16 ± 9	90 ± 13	63 ± 6	7.27 $^{+0.70}_{-1.60}$	–15.91 ± 0.02	11659
J0400–52:S3	1900 ± 620	315 ± 177	7570 ± 830	3020 ± 290	1140 ± 150	794 ± 59	9.23 $^{+0.07}_{-0.07}$	–20.02 ± 0.01	11384
J0400–52:S4	305 ± 31	159 ± 33	1430 ± 94	698 ± 53	204 ± 28	154 ± 7	9.21 $^{+0.04}_{-0.04}$	–22.82 ± 0.01	9967
J0400–52:S5	1350 ± 120	420 ± 68	6740 ± 300	3100 ± 140	905 ± 60	904 ± 34	9.22 $^{+0.02}_{-0.02}$	–22.71 ± 0.05	10790
J0400–52:S6	171 ± 29	81 ± 24	1240 ± 130	476 ± 49	189 ± 22	132 ± 1	9.15 $^{+0.05}_{-0.05}$	–22.13 ± 0.06	10287
J0400–52:S7	526 ± 105	456 ± 114	1740 ± 180	423 ± 47	463 ± 63	337 ± 27	9.08 $^{+0.11}_{-0.11}$	–18.89 ± 0.13	10607
J0400–52:S8 ^b	51 ± 22	52 ± 32	252 ± 38	119 ± 31	72 ± 13	51 ± 8	8.70 $^{+0.08}_{-0.08}$	–17.36 ± 0.08	9921
J0400–52:S9 ^b	89 ± 19	53 ± 48	728 ± 72	365 ± 49	193 ± 34	135 ± 9	8.98 $^{+0.13}_{-0.16}$	–17.56 ± 0.07	10287
J1051–17:S1	16 ± 11	31 ± 11	46 ± 11	8 ± 8	4 ± 7	3 ± 0	8.96 $^{+0.02}_{-0.03}$	–21.55 ± 0.26	5465
J1051–17:S2	11 ± 2	14 ± 2	139 ± 11	135 ± 10	40 ± 3	30 ± 2	9.21 $^{+0.03}_{-0.03}$	–21.85 ± 0.04	5288
J1051–17:S3	167 ± 72	255 ± 82	273 ± 75	101 ± 49	29 ± 16	48 ± 10	9.00 $^{+0.19}_{-0.28}$	–18.14 ± 0.05	5969
J1051–17:S4 ^c	94 ± 17	196 ± 29	394 ± 54	15 ± 8	67 ± 11	47 ± 6	7.50 $^{+0.41}_{-0.74}$	–16.34 ± 0.09	5465
J1051–17:S5	35 ± 26	60 ± 30	1540 ± 220	176 ± 33	373 ± 51	261 ± 30	8.40 $^{+0.14}_{-0.15}$	–17.20 ± 0.06	5465
J1051–17:S6	30 ± 4	55 ± 7	121 ± 15	17 ± 2	19 ± 2	13 ± 2	8.60 $^{+0.09}_{-0.09}$	–16.95 ± 0.04	5648
J1051–17:S7	9 ± 1	11 ± 1	32 ± 4	3 ± 0	5 ± 1	4 ± 0	8.42 $^{+0.10}_{-0.11}$	–16.94 ± 0.12	5374
J1051–17:S8	28 ± 9	73 ± 17	374 ± 44	200 ± 24	166 ± 20	134 ± 15	8.80 $^{+0.08}_{-0.08}$	–17.48 ± 0.04	5294
J1051–17:S9	99 ± 29	109 ± 26	507 ± 70	131 ± 27	176 ± 27	123 ± 15	8.63 $^{+0.13}_{-0.13}$	–16.68 ± 0.05	5582
J1403–06:S1	1290 ± 90	301 ± 37	3110 ± 210	1350 ± 90	489 ± 39	359 ± 24	9.20 $^{+0.03}_{-0.03}$	–21.77 ± 0.35	2498
J1403–06:S2	1780 ± 160	12900 ± 900	4820 ± 460	5470 ± 500	1310 ± 120	1340 ± 120	9.10 $^{+0.03}_{-0.04}$	–22.74 ± 0.09	2727
J1403–06:S3 ^c	600 ± 51	1460 ± 130	1200 ± 170	64 ± 12	209 ± 31	146 ± 21	7.93 $^{+0.17}_{-0.20}$	–15.38 ± 0.85	2753
J1403–06:S4 ^c	208 ± 28	233 ± 27	520 ± 86	13 ± 7	78 ± 21	55 ± 9	7.40 $^{+0.58}_{-1.39}$	–14.51 ± 0.86	2671

Table 2
(Continued)

HIPASS+	H β	[O III]	H α	[N II]	[S II]	[S II]	12+log(O/H)	M_R	V_{hel}
(1)	4861.3	5006.9	6562.8	6583.4	6716.4	6730.8	(8)	(mag)	(km s $^{-1}$)
(1)	(2)	(3)	(4)	(5)	(6)	(7)	(8)	(9)	(10)
J1408–21:S1	2160 \pm 290	878 \pm 130	9140 \pm 540	4600 \pm 280	1080 \pm 90	966 \pm 75	9.25 $^{+0.03}_{-0.03}$	–23.15 \pm 0.26	8694
J1408–21:S2	661 \pm 76	212 \pm 46	2780 \pm 189	1050 \pm 70	404 \pm 37	352 \pm 19	9.15 $^{+0.04}_{-0.04}$	–21.69 \pm 0.06	8821
J1408–21:S3	887 \pm 86	258 \pm 34	3770 \pm 310	1330 \pm 120	637 \pm 62	505 \pm 30	9.10 $^{+0.04}_{-0.05}$	–20.72 \pm 0.10	8782
J1408–21:S4	202 \pm 25	104 \pm 31	998 \pm 104	393 \pm 41	237 \pm 27	165 \pm 14	9.02 $^{+0.06}_{-0.07}$	–21.23 \pm 0.08	9126
J1408–21:S5	204 \pm 402	428 \pm 601	654 \pm 284	101 \pm 228	119 \pm 94	83 \pm 13	8.57 $^{+0.13}_{-0.14}$	–13.31 \pm 0.52	8778
J1408–21:S6 ^a	336 \pm 155	15 \pm 124	329 \pm 127	0 \pm 0	0 \pm 0	0 \pm 0	0.00 $^{+0.00}_{-0.00}$	–17.12 \pm 0.07	8672
J1956–50:S1	262 \pm 61	218 \pm 56	1570 \pm 180	631 \pm 83	172 \pm 34	126 \pm 15	9.18 $^{+0.05}_{-0.06}$	–22.35 \pm 0.19	7610
J1956–50:S2	2170 \pm 2300	1710 \pm 190	7670 \pm 720	2110 \pm 200	1510 \pm 150	1080 \pm 100	8.89 $^{+0.06}_{-0.06}$	–20.78 \pm 0.11	7015
J1956–50:S3	1590 \pm 160	10700 \pm 900	5070 \pm 610	110 \pm 20	198 \pm 31	139 \pm 20	8.24 $^{+0.16}_{-0.15}$	–16.65 \pm 0.22	6375
J1956–50:S4	242 \pm 31	413 \pm 55	610 \pm 82	59 \pm 14	94 \pm 14	70 \pm 9	8.40 $^{+0.16}_{-0.18}$	–15.15 \pm 0.23	7472
J2027–51:S1	51 \pm 5	47 \pm 4	621 \pm 33	321 \pm 16	134 \pm 8	226 \pm 14	8.99 $^{+0.03}_{-0.03}$	–21.73 \pm 0.29	5830
J2027–51:S2	42 \pm 3	29 \pm 2	980 \pm 64	306 \pm 20	155 \pm 10	166 \pm 11	9.01 $^{+0.04}_{-0.04}$	–21.91 \pm 0.16	5783
J2027–51:S3	1300 \pm 140	2740 \pm 280	4240 \pm 550	623 \pm 75	997 \pm 121	708 \pm 86	8.43 $^{+0.09}_{-0.10}$	–19.24 \pm 0.12	5830
J2027–51:S4	1740 \pm 140	3080 \pm 260	5770 \pm 660	815 \pm 99	1130 \pm 130	792 \pm 86	8.50 $^{+0.08}_{-0.09}$	–17.40 \pm 0.15	6013
J2318–42a:S1	8610 \pm 500	25400 \pm 1000	61900 \pm 2100	45100 \pm 1400	10300 \pm 300	9670 \pm 290	9.16 $^{+0.01}_{-0.01}$	–22.25 \pm 0.26	1461
J2318–42a:S2	583 \pm 81	2300 \pm 230	5780 \pm 480	5170 \pm 390	2450 \pm 190	2110 \pm 130	8.99 $^{+0.04}_{-0.04}$	–21.22 \pm 0.05	1481
J2318–42a:S3	2890 \pm 220	1490 \pm 130	13700 \pm 1500	3280 \pm 430	1800 \pm 220	1270 \pm 150	9.01 $^{+0.07}_{-0.07}$	–20.15 \pm 0.28	1777
J2318–42a:S4 ^a	88 \pm 24	29 \pm 21	213 \pm 30	222 \pm 15	16 \pm 7	34 \pm 4	0.00 $^{+0.00}_{-0.00}$	–11.45 \pm 0.17	1685

Notes. Columns: (1) SINGG name; ((2)–(7)) observed fluxes for various emission lines, in units of 10^{-17} erg s $^{-1}$ cm $^{-2}$; (8) metallicity calibrated using Dopita et al. 2013; (9) SINGG R -band absolute magnitude; (10) WiFeS heliocentric velocity.

^a Metallicity not measurable due to poor signal in one or more lines.

^b Very metal-poor dwarfs.

^c TDG candidates.

REFERENCE

Dopita, M. A., Sutherland, R. S., Nicholls, D. C., Kewley, L. J., & Vogt, F. P. A. 2013, *ApJS*, 208, 10

Endnotes to the Chapter

Conclusions:

4. The simulated TDG metallicities are sensitive to the assumed initial central metallicity and metallicity gradient of the simulated host galaxy.
5. The finding that gas-rich cluster dwarfs have lower metallicity than isolated dwarfs is in contrast to other authors who found that some dwarfs in clusters have high metallicity (Duc et al., 2001; Vílchez & Iglesias-Páramo, 2003).

4

The Kinematics of Gas-Rich Dwarf Galaxies

Having developed the luminosity-metallicity relation diagnostic for identifying a sample of tidal dwarf galaxy (TDG) candidates, I now aim to measure the dark matter content of dwarf galaxies in order to confirm which tidal dwarf galaxy candidates have no dark matter and are therefore bonafide tidal dwarf galaxies.

4.1 Chapter Outline

In this chapter I present Keck/DEIMOS (DEep Imaging Multi-Object Spectrograph) observations of 22 star-forming dwarf galaxies located in four gas-rich groups, including six newly-discovered dwarfs. I give a brief background and outline the chapter aims in Section 4.2. Section 4.3 outlines my sample selection, observations and data processing. In Section 4.4 I present and discuss my results. Section 4.5 summarises the chapter.

4.2 Background and Aims

Most TDGs discovered to date have been detected due to their location in the tidal streams in which they form (e.g. Mirabel et al., 1992; Duc et al., 2000; Weilbacher et al., 2003; Duc et al., 2011, 2014). However, the same streams that identify these objects as TDGs also cause tidal distortion of their velocity fields, so that dynamical masses cannot be reliably measured, nor can the presence or absence of DM be determined (Casas et al., 2012). For example, dwarf galaxies in obviously interacting systems such as the Perseus Cluster have comparable M/L ratios ($\sim 120 M_{\odot}/L_{\odot}$) to the CDM dwarf satellites of the Milky Way (Penny et al., 2009). The exception to this problem is where tidal streams are old and faded, as in Duc et al. (2014), and the TDG has had time to reach dynamical equilibrium.

The aim of this chapter is to overcome the above problems by measuring dwarf galaxies in the Choir groups, many of which do not have obvious optical tidal tails. I select TDG candidates by their location above the luminosity-metallicity relation, and model the rotation curves of my sample of dwarf galaxies, accounting for rotational velocity and a pressure support component. In doing so I measure the M/L ratio in order to determine the absence of DM and confirm the tidal nature of these dwarfs.

4.3 Sample Selection, Observations and Data Processing

My sample consists of dwarf galaxies within the star-forming, gas-rich groups known as Choirs, as described in Chapter 2 (Sweet et al., 2013). These fifteen groups of four or more narrow-band H α emission line galaxies were detected in the Survey for Ionisation in Neutral Gas Galaxies (SINGG Meurer et al., 2006), a survey of HI detections from the HI Parkes All Sky Survey (HIPASS Barnes et al., 2001).

I obtained Keck DEIMOS (Faber et al., 2003) spectroscopy for four of these groups on 2013 Feb 11, using the 1200L grating with central wavelength 5950 Å and the GG400 order-blocking filter. Each group was observed for six 1200-s exposures. The groups with the highest metallicity TDG candidates were not observed with Keck as they are too far south to be accessible by the telescope. Mask and slit placements are shown in Figures 4.1 to 4.4. The slit width was 0.75 arcseconds to approximately match the seeing, with a corresponding FWHM velocity resolution

of 1.1 Å. I chose the mask position angle to facilitate observing as many of my Choir member galaxies as possible. Some of the giant galaxies have multiple slits due to their extended size on the mask, multiple SF regions, and/or position angle of the major axis with respect to the mask. I then assigned priorities to various objects in the field of view, with the highest priorities going to Choir member galaxies and ELdots (unresolved narrow-band sources; Ryan-Weber et al., 2004). The remaining spare mask area was allocated to other potential members in the field as detected in the SINGG imaging, with astrometry matched to the USNOB catalogue: firstly to objects suggestive of some net H α emission, and secondly to any remaining objects classified by SExtractor¹ to be galaxy-like. This selection expanded my sample to ~ 100 objects per mask.

Data processing was conducted using the DEIMOS DEEP2 IDL-based data reduction pipeline². This pipeline is optimised for compact sources observed with a central wavelength of around 7700 Å, so I employed Evan Kirby's modification³ to enable processing of the bluer wavelengths in my data. I also modified the sky subtraction routines to give more flexibility for extended sources, as most of my galaxies are sufficiently extended to fill their slits. In these cases I select a section of another slit that contains some sky to perform a non-local sky subtraction. While there is some residual sky emission due to spatial variation in the observed sky spectrum and path through the optics and detector, the residual sky emission does not overlap with the H α for the redshifts of my groups, so the result is adequate for velocity measurements.

I wrote IDL routines to extract a portion of the spectrum at the expected H α wavelength for each row of binned pixels, and fit a single Gaussian profile to the peak to measure redshift. There is no evidence for multiple components at the resolution of my data. The peak location error from the χ^2 -minimisation fit is used to derive the 1- σ velocity errors and error bars quoted herein. The H α width and flux and continuum flux were also measured for each bin. In order to measure the true profile width, the spectrum cutout was deconvolved with a point spread function (PSF) measured from a nearby bright sky line. Importantly, I noticed that the PSF varied significantly with the tilt and location of the slit on the mask, so I chose a sky line in each slit for the PSF measurement. Heliocentric velocity corrections were calculated using the IRAF package RVCORRECT. My measurements confirm that six of the potential member galaxies in two groups lie at the group redshift; these are included in Table 4.1.

¹<http://www.astromatic.net/software/sextractor>

²<http://www2.keck.hawaii.edu/inst/deimos/pipeline.html>

³http://www2.keck.hawaii.edu/inst/deimos/calib_blue.html

I observed one spectrophotometric standard star for each mask and performed flux calibration in the standard manner. I measured integrated metallicity for each galaxy by collapsing spectra in the spatial direction and fitting a Gaussian profile to these integrated spectra to measure strong emission line fluxes. For the giant galaxies spanning multiple slits I measured metallicity for the central slit, for direct comparison with the sample in Chapter 3 (Sweet et al., 2014). The wavelength range of DEIMOS 1200L grating with my central wavelength covers most of the necessary strong emission lines for using the Dopita et al. (2013) $[\text{NII}]/[\text{SII}]$ vs. $[\text{OIII}]/[\text{SII}]$ diagnostic. This is the same calibration as used in Chapter 3 (Sweet et al., 2014); I give a discussion of my reasons for choosing it in that chapter. Briefly, this diagnostic gives consistent results with recombination and electron temperature methods; is not degenerate, clearly separating ionization parameter and metallicity; and, the necessary lines are available in most of my sample. The DEIMOS metallicities are generally not dereddened, because most do not have measurable $\text{H}\beta$, with the line either lost in the noise of the blue end, or fallen off of the chip. In any case the diagnostic is not very dependent on reddening: because the $[\text{NII}]$ and $[\text{SII}]$ lines are nearby in wavelength, the $[\text{NII}]/[\text{SII}]$ ratio will not vary much with reddening; further, the metallicity is sensitive to the $[\text{NII}]/[\text{SII}]$ ratio and not the $[\text{OIII}]/[\text{SII}]$ ratio in the diagnostic. For the galaxies with all three strong emission lines available, I use the methods described in Chapter 3 (Sweet et al., 2014) to interpolate for metallicity and ionization parameter $\log(q)$.

The remainder of the sample only has $[\text{NII}]$ and $[\text{SII}]$ available. While this ratio is sensitive to metallicity, the missing $[\text{OIII}]/[\text{SII}]$ ratio tells the dependence on ionization parameter. For these galaxies I roughly estimated ionization parameter $\log(q)$ based on the fit to $\log(q)$ as a function of M_R of the DEIMOS galaxies for which all three strong lines are available. I then used $[\text{NII}]/[\text{SII}]$ and $\log(q)$ to estimate $12 + \log(\text{O}/\text{H})$ by inspection of the same diagnostic. These measurements are therefore less reliable and have a nominal 0.5 dex error bar to show this. While the $[\text{NII}]/[\text{SII}]$ ratio alone has a similar scatter to the $[\text{NII}]/\text{H}\alpha$ calibration (e.g. Marino et al., 2013), the method just described has the added benefit of $\log(q)$, which gives a better constraint on the metallicity. The new metallicity measurements are catalogued in Table 4.1.

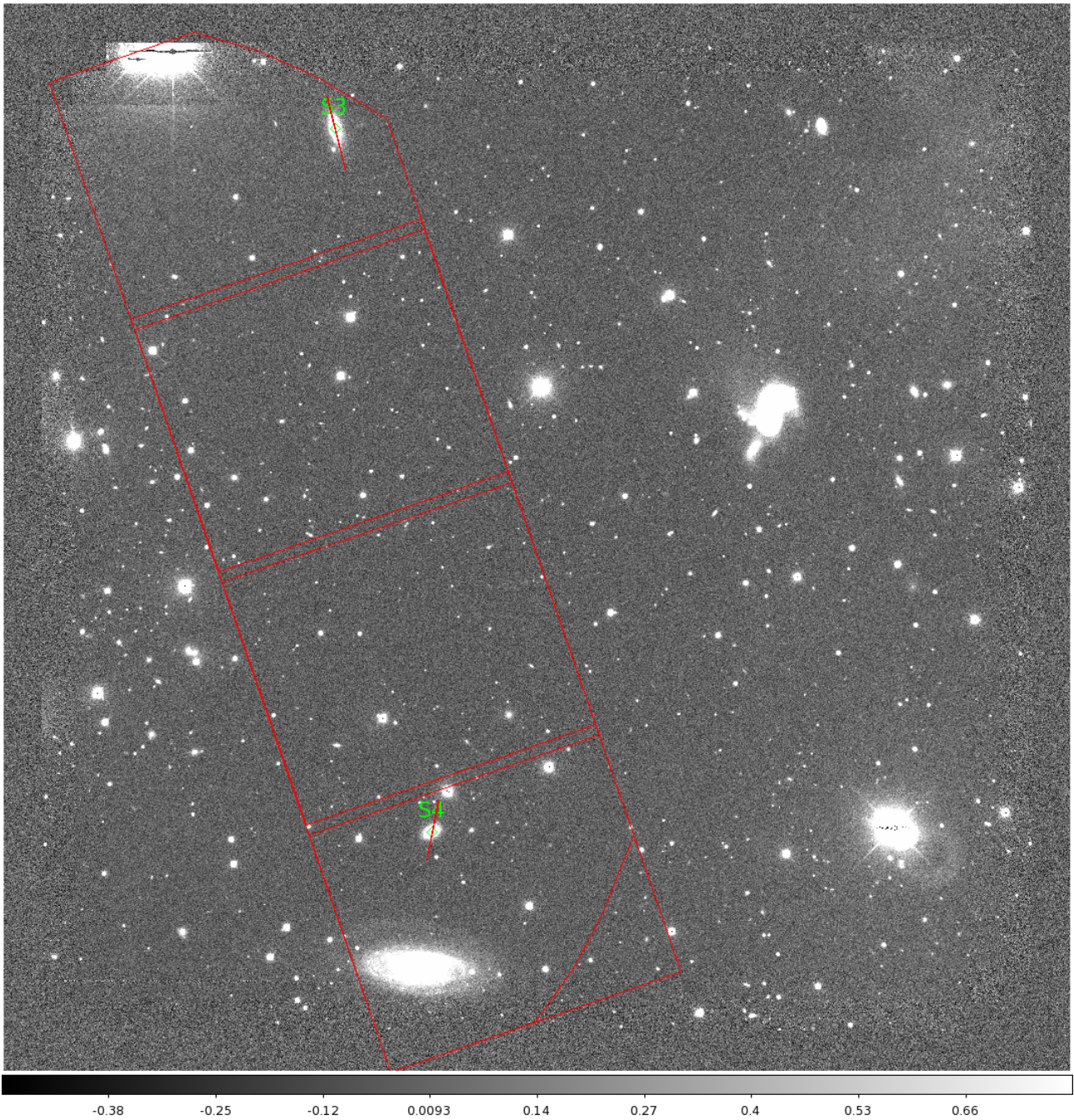


FIGURE 4.1: SINGG image of HIPASS J0443-05 showing locations of slits (red) for measured group member dwarf galaxies (green labels). The approximate location of the DEIMOS mask is given by the red polygon. Other slits are not shown for clarity.

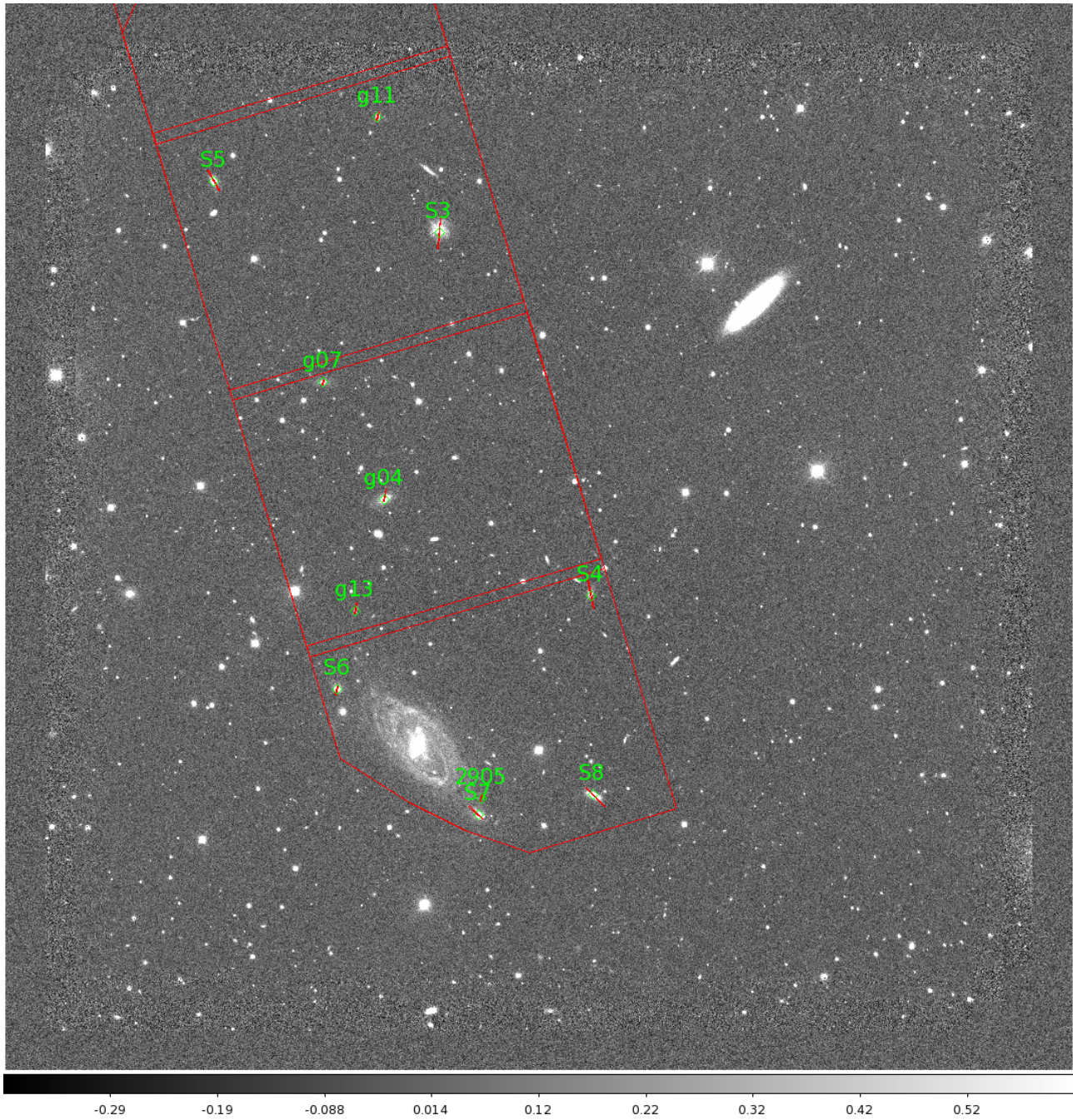


FIGURE 4.2: As for Figure 4.1; HIPASS J1051-17.

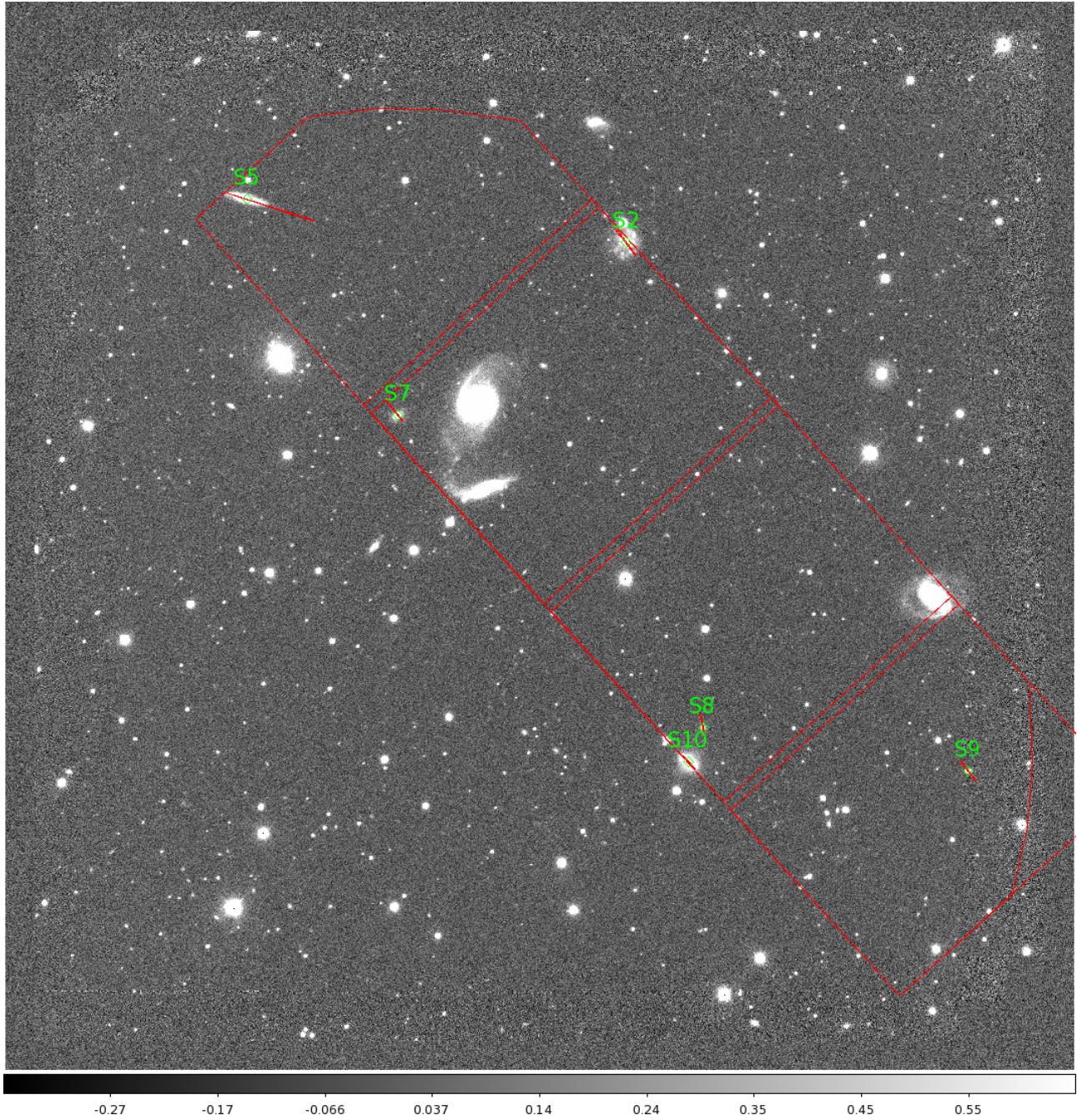


FIGURE 4.3: As for Figure 4.1; HIPASS J1059-09.

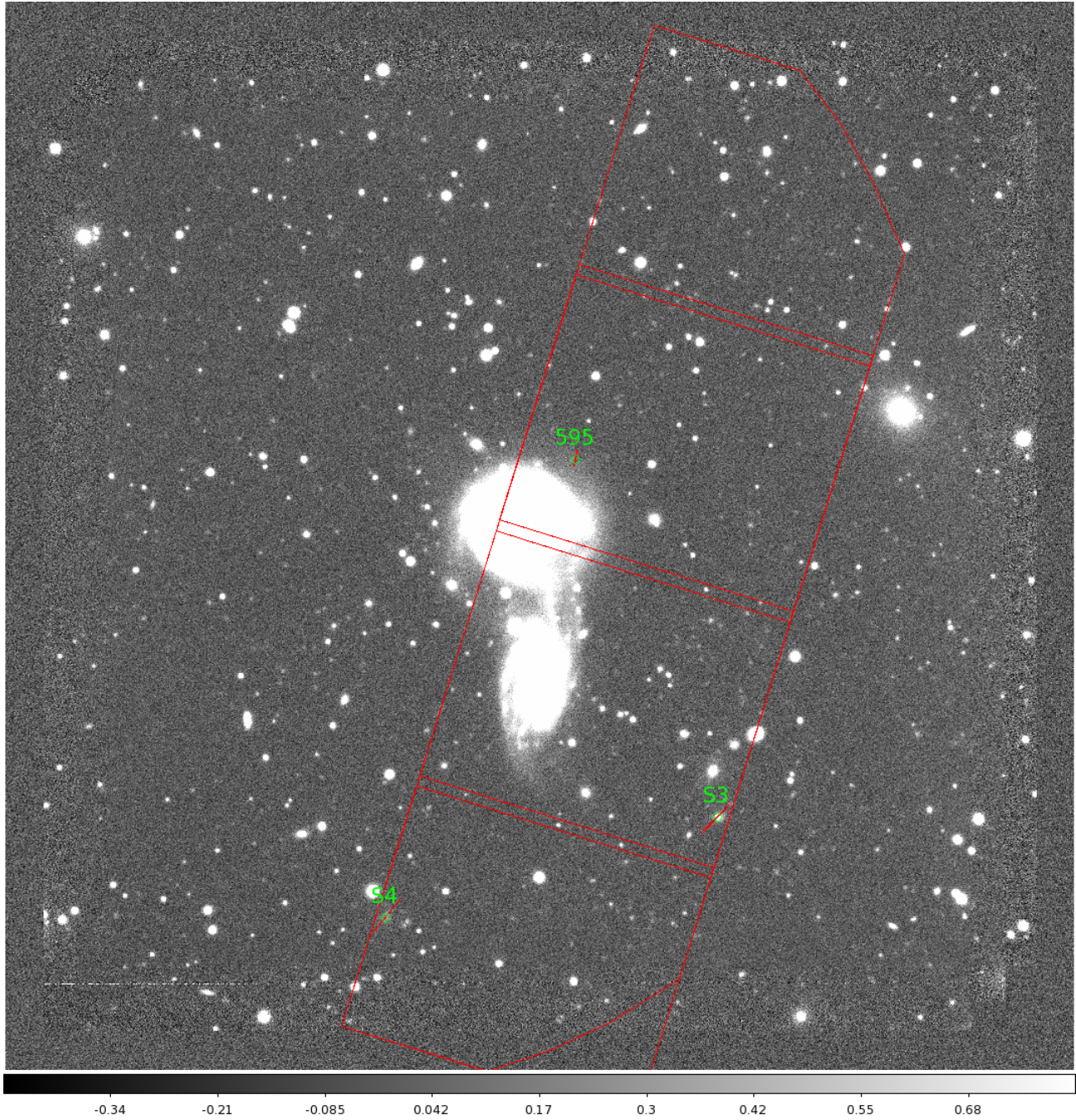


FIGURE 4.4: As for Figure 4.1; HIPASS J1403-06.

TABLE 4.1: Measured quantities for group member galaxies, including new group members. Columns (1) to (11).

(1) HIPASS+	(2) RA [h m s]	(3) Dec [d m s]	(4) reff [$''$]	(5) a/b	(6) PA [$^{\circ}$]	(7) corr.	(8) M_R [mag]	(9) r_0 [kpc]	(10) I_0 [L_{\odot} /kpc]	(11) V_{hel} [km/s]
J0443-05:S3	04 44 11.67	-05 14 38.31	04.79 \pm 0.19	1.86	19	0.883	-19.93 \pm 0.19	1.809	2.3E+8	4591
J0443-05:S4	04 44 05.54	-05 25 46.50	04.95 \pm 0.12	1.6	120	0.537	-19.07 \pm 0.12	1.048	5.9E+8	4774
J1051-17:S3	10 51 35.94	-16 59 16.80	06.61 \pm 0.05	1.02	74	0.048	-18.14 \pm 0.05	2.232	4.7E+7	5969
J1051-17:S4	10 51 26.01	-17 05 03.61	03.48 \pm 0.09	1.4	164	0.661	-16.34 \pm 0.09	0.837	7.5E+7	5465
J1051-17:S5	10 51 50.91	-16 58 31.64	03.58 \pm 0.06	1.75	29	0.865	-17.20 \pm 0.06	0.842	1.9E+8	5465
J1051-17:S6	10 51 42.78	-17 06 34.59	02.11 \pm 0.04	1.29	40	0.422	-16.95 \pm 0.04	0.492	3.0E+8	5648
J1051-17:S7	10 51 33.36	-17 08 36.63	04.18 \pm 0.12	1.53	49	0.802	-16.94 \pm 0.12	0.799	1.2E+8	5374
J1051-17:S8	10 51 25.92	-17 08 16.44	01.52 \pm 0.67	3.07	63	0.927	-17.48 \pm 0.04	0.804	7.5E+8	5294
J1051-17:g04	10 51 39.679	-17 03 34.16	02.97 \pm 0.14	1.06	43	0.21	-17.49 \pm 0.05	1.45	5.0E+7	5535
J1051-17:g07	10 51 43.698	-17 01 42.99	03.34 \pm 0.09	1.12	42	0.3	-15.69 \pm 0.08	0.95	4.0E+7	6166
J1051-17:g11	10 51 40.051	-16 57 30.94	01.95 \pm 0.13	1.62	47	0.027	-15.84 \pm 0.11	0.28	1.3E+9	5371
J1051-17:g13	10 51 41.602	-17 05 20.16	01.52 \pm 0.16	1.05	42	0.21	-14.46 \pm 0.21	0.685	8.0E+6	5577
J1051-17:2905	10 51 33.286	-17 08 19.17	05.26 \pm 0.85	1.05	42	0.21	-14.69 \pm 0.81	2.63	4.0E+6	5225
J1059-09:S2	10 59 06.77	-09 45 04.38	11.72 \pm 0.24	1.36	131	0.056	-20.19 \pm 0.24	5.271	4.7E+7	8013
J1059-09:S5	10 59 30.98	-09 44 25.26	09.11 \pm 0.13	2.84	75	0.968	-19.94 \pm 0.13	2.973	2.4E+8	7926
J1059-09:S7	10 59 21.31	-09 47 50.49	02.50 \pm 0.15	1.59	115	0.167	-19.13 \pm 0.15	0.761	1.2E+9	7862

Continued on next page

TABLE 4.1: Measured quantities for group member galaxies, including new group members. Columns (1) to (11).

(1) HIPASS+	(2) RA [h m s]	(3) Dec [d m s]	(4) r _{eff} [\prime]	(5) a/b	(6) PA [$^\circ$]	(7) corr.	(8) M _R [mag]	(9) r ₀ [kpc]	(10) I ₀ [L _⊙ /kpc]	(11) V _{hel} [km/s]
J1059-09:S8	10 59 01.73	-09 52 46.76	03.47±0.40	1.81	155	0.702	-16.98±0.40	1.028	9.4E+7	8260
J1059-09:S9	10 58 44.69	-09 53 28.60	01.99±0.08	1.39	45	0.604	-13.43±0.08	0.63	2.0E+8	8475
J1059-09:S10	10 59 02.64	-09 53 19.90	03.49±0.01	1.2	40	0.746	-17.43±0.01	4.11	5.0E+7	8219
J1403-06:S3	14 03 13.48	-06 06 24.17	04.18±0.85	1.03	14	0.158	-15.38±0.85	0.448	7.5E+7	2753
J1403-06:S4	14 03 34.62	-06 07 59.27	05.96±0.86	1.43	123	0.731	-14.51±0.86	0.961	1.4E+7	2671
J1403-06:595	14 03 22.475	-06 00 44.24	03.57±0.36	2.04	46	0.76	-13.14±1.39	2.51	6.3E+6	2692

Columns: (1) SINGG name; (2) right ascension; (3) declination; (4) effective radius; (5) ratio of major to minor axes; (6) position angle; (7) velocity correction $\sin(i)\cos(\phi)$; (8) *R*-band magnitude; (9) scale length; (10) central surface luminosity; (11) heliocentric velocity.

TABLE 4.1: Measured quantities for group member galaxies, including new group members. Columns (12) to (23).

(1)	(12)	(13)	(14)	(15)	(16)	(17)	(18)	(19)	(20)	(21)	(22)	(23)
HIPASS+	H β	[O III]	H α	[N II]	[S II]	log(q)	12+log(O/H)	A	M/L	V_{rot}	σ_D	r_{tidal}
									[M_{\odot}/L_{\odot}]	[km/s]	[km/s]	[$''$]
J0443-05:S3			10.5 \pm 2.1	0.8 \pm 0.4	3.4 \pm 1.5	7	8.5 \pm ^{0.5} _{0.5}	A	4.15	120	8.1	89
J0443-05:S4		28.2 \pm 8.8	174.8 \pm 1.0	46.9 \pm 0.4	69.6 \pm 1.5	6.89	8.86 \pm ^{0.07} _{0.07}	A	0.55	31.6	6.4	16
J1051-17:S3		7.2 \pm 0.7	19.0 \pm 0.2	2.8 \pm 0.2	8.6 \pm 1.0	6.8	8.48 \pm ^{0.27} _{0.22}			3.8	0	37
J1051-17:S4		5.0 \pm 0.6	9.8 \pm 0.1	0.4 \pm 0.1	3.8 \pm 1.3	6.91	8.3 \pm ^{0.78} _{0.54}	A	0.58	12.2	6.6	16
J1051-17:S5			32.4 \pm 0.4	2.9 \pm 0.3	12.4 \pm 0.7	7.13	8.15 \pm ^{0.5} _{0.5}	A	0.51	24.9	15.4	47
J1051-17:S6			162.2 \pm 2.1	22.5 \pm 0.6	49.3 \pm 2.0	7.15	8.55 \pm ^{0.5} _{0.5}	A	0.25	8.1	13	8
J1051-17:S7						0	0 \pm ₀	A	0.03	3.8	14.3	8
J1051-17:S8			4.7 \pm 0.1	3.9 \pm 0.2		0	0 \pm ₀	A	0.14	27.4	19.4	18
J1051-17:g04			19.3 \pm 0.4	6.7 \pm 0.4	15.0 \pm 0.6	7.58	8.45 \pm ^{0.5} _{0.5}			14.3	0	24
J1051-17:g07			15.0 \pm 0.4	2.4 \pm 0.4	5.1 \pm 1.6	7.82	8.2 \pm ^{0.5} _{0.5}			13.8	1.1	21
J1051-17:g11			0.7 \pm 0.1	0.5 \pm 0.2	1.5 \pm 0.2	7.85	8.65 \pm ^{0.5} _{0.5}			20.1	0.1	23
J1051-17:g13		13.0 \pm 2.3	11.9 \pm 0.2	0.7 \pm 0.2	3.4 \pm 0.6	6.99	8.12 \pm ^{0.44} _{0.44}			12	1.8	6
J1051-17:2905		134.6 \pm 48.8	12.4 \pm 0.2	1.7 \pm 0.2	7.8 \pm 1.4	6.82	8.19 \pm ^{0.58} _{0.99}			0	0	3
J1059-09:S2		41.9 \pm 6.9	43.3 \pm 0.7	6.3 \pm 0.4	17.6 \pm 1.1	6.99	8.41 \pm ^{0.11} _{0.11}			33.1	0.1	31
J1059-09:S5						0	0 \pm ₀	A	0.28	41.4	22.7	40
J1059-09:S7	10.4 \pm 0.2	13.0 \pm 2.0	65.9 \pm 1.0	14.8 \pm 0.3	23.8 \pm 0.9	6.9	8.79 \pm ^{0.05} _{0.05}			7.4	4.2	8

Continued on next page

TABLE 4.1: Measured quantities for group member galaxies, including new group members. Columns (12) to (23).

(1)	(12)	(13)	(14)	(15)	(16)	(17)	(18)	(19)	(20)	(21)	(22)	(23)
HIPASS+	H β	[O III]	H α	[N II]	[S II]	log(q)	12+log(O/H)	A	M/L	V_{rot}	σ_D	r_{tidal}
									[M_{\odot}/L_{\odot}]	[km/s]	[km/s]	[$''$]
J1059-09:S8	1.3 \pm 0.3	3.2 \pm 1.5	6.5 \pm 0.3	1.2 \pm 0.1	2.6 \pm 0.4	7.02	8.67 $\pm^{0.28}_{0.26}$	A	0.4	14.1	6.7	29
J1059-09:S9	1.4 \pm 0.1	7.5 \pm 1.4	9.0 \pm 0.3	0.7 \pm 0.1	4.0 \pm 0.4	6.91	8.33 $\pm^{0.4}_{0.32}$	A	0.43	14.1	18.5	17
J1059-09:S10		4.7 \pm 0.7		9.3 \pm 1.3	2.0 \pm 1.1	9.49	9.3 $\pm^{0.26}_{0.09}$			0.4	0	35
J1403-06:S3			9.9 \pm 0.1	0.6 \pm 0.1	2.4 \pm 0.1	7.29	8.05 $\pm^{0.5}_{0.5}$			4.7	0	11
J1403-06:S4			2.4 \pm 0.1	0.2 \pm 0.1	0.6 \pm 0.1	7.38	7.4 $\pm^{0.5}_{0.5}$			4.8	10.9	10
J1403-06:595	3.3 \pm 0.1		21.5 \pm 0.2	5.7 \pm 0.2	6.9 \pm 0.1	7.56	8.8 $\pm^{0.5}_{0.5}$			32.5	0.2	2

(12-16) observed flux for various emission lines in units of 10^{-22} erg s^{-1} cm^{-2} ; [O III] 5006.9, [N II] λ 6583.4, [S II] λ 6717.0+6731.3; (17) estimated ionization parameter based on Dopita et al. (2013) interpolation if [OIII] available, or on M_R -log(q) relation of other galaxies in this sample otherwise; (18) 12+log(O/H) using Dopita et al. (2013) calibration; (19) Membership of Sample A (based on quality of rotation curve) is indicated here by the letter 'A'; (20) mass-to-light ratio; (21) modelled rotational velocity at r_{turn} ; (22) modelled pressure support component at r_{turn} ; (23) tidal radius.

4.4 Results and Discussion

In this section I present the results of my DEIMOS observations. I identify new strong TDG candidates based on my luminosity-metallicity diagnostic in Subsection 4.4.1. In Subsection 4.4.2 and Subsection 4.4.3 I model the rotation curves of all of the dwarf galaxies for which I have DEIMOS observations. Those results are presented in Figure 4.6 and Figures 4.9 to 4.29. In Subsection 4.4.4 I discuss the quality of the rotation curves and narrow down a sample for further analysis: M/L ratios in Subsection 4.4.5. Next, in Subsection 4.4.6 I consider whether or not the falling rotation curves expected for TDGs can in fact be detected. Lastly, I discuss the strongly-falling rotation curve of J0443-05:S4 in Subsection 4.4.7.

4.4.1 Luminosity-metallicity relation

In Figure 4.5 I plot the luminosity-metallicity relation for my full sample of WiFeS and DEIMOS measurements. In general, the galaxies with DEIMOS measurements are consistent with the portion of my sample for which I have WiFeS measurements, and with the SDSS relation defined in Chapter 3 (Sweet et al., 2014). In that chapter I identified a metallicity floor for low luminosity galaxies in SDSS; there is a suggestion of the metallicity floor being continued to fainter magnitudes by the new measurements.

Based solely on my definition from Chapter 3 (Sweet et al., 2014), my three additional very strong TDG candidates ($12+\log(\text{O}/\text{H})>8.6$ and more than 3σ above SDSS) are J1051-17:g11, J1403-06:595, J1059-09:S10. However, J1403-06:595 lies in the halo of its host spiral, and is probably experiencing strong tidal interactions, so is not detectable as a TDG based on its velocity field (see Section 4.4.6). Also, the very high metallicity ($12+\log(\text{O}/\text{H})=9.3$) of J1059-09:S10 would require a host galaxy with even higher metallicity, which is unlikely.

Some of the galaxies in my sample have both WiFeS and DEIMOS metallicity measurements. In the J1403-06 group these metallicities happily agree to within quoted errors even without [OIII] for the DEIMOS measurements. However, the J1051-17 group members where we can compare the data generally do not have consistent metallicities between DEIMOS and WiFeS, separated by up to 2σ . This is partly due to the missing [OIII] line for some of the DEIMOS measurements, but more so because bright sky lines fall on the [SII] lines at the distance of this group. There is some unavoidable sky residual for both instruments due to the non-local sky subtraction employed. The sky residuals therefore contribute to the [SII] flux measurements

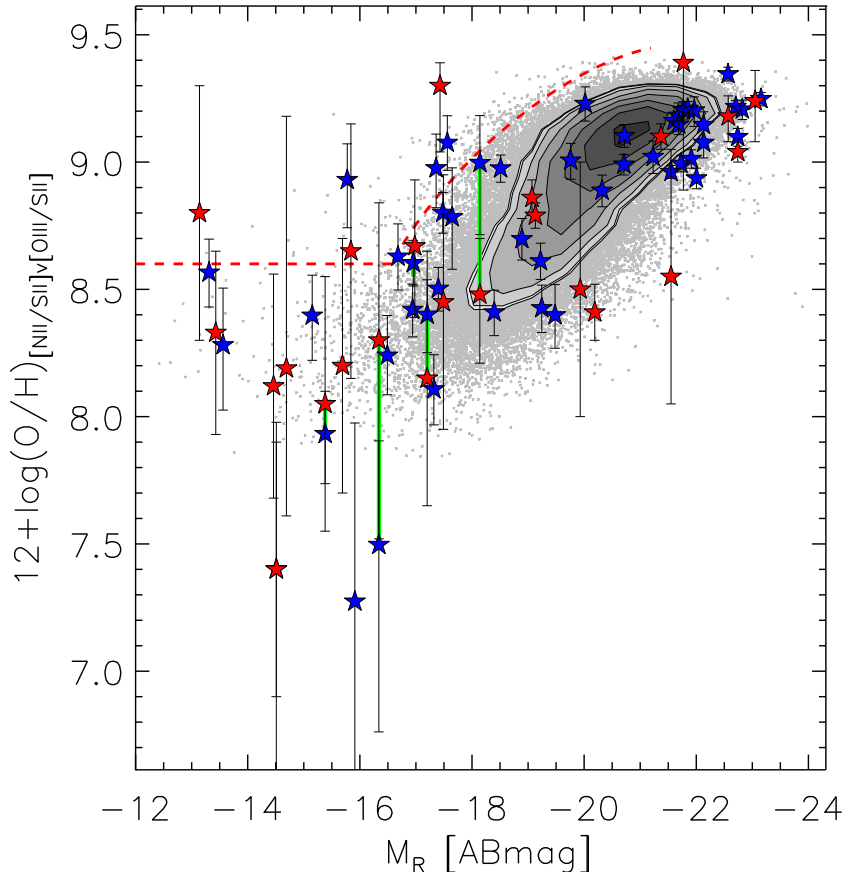


FIGURE 4.5: Luminosity-metallicity relation for full sample of galaxies. Blue stars are existing WiFeS measurements from Chapter 3 (Sweet et al., 2014). Red stars are DEIMOS measurements. Green bars connect WiFeS and DEIMOS metallicities for five of the six galaxies that have measurements from both instruments; both measurements for J1403-06:S4 at $M_R = -14.51$ are equal. Grey points and contours depict SDSS star-forming galaxies, while the red, dashed line indicates my strong TDG candidate diagnostic.

and skew the metallicities for this group. I expect that the DEIMOS sky subtraction discussed above may be worse than for the WiFeS observations, where I used a nod-and-shuffle technique which minimised systematics related to optics and detector position.

4.4.2 Rotation curve modelling

For the dwarf galaxies in my sample I constructed rotation curve diagrams, defining zero velocity at the bin containing the peak continuum flux centre. This centre is a reasonable match to optical SINGG isophotal measurement of centre for most of the galaxies in the sample. For J0443-05:S3 there are bad rows very near the centre of the galaxy, so for this galaxy I fit the centre by eye, assuming a symmetrical mass distribution. The rotation curve for the (subjectively) most interesting in my sample, J0443-05:S4, is shown in Figure 4.6. Rotation

curves for the other galaxies in my sample, along with notes on each, are shown in Figures 4.9 to 4.29. For giant galaxies that have multiple slits, rotation curves are not constructed here. As giant galaxies, they are too big to be TDG candidates, so they are not the focus of this analysis.

I test for the absence of DM by modelling the rotation curves of these galaxies. If the observed rotation curve is consistent with a mass-follows-light profile instead of flat, then DM is not required to explain the rotational velocity⁴. I assume an exponential disk and use the analytical prescriptions of Freeman (1970) for this modelling: the predicted rotational velocity for a mass-follows-light system is given by $v_{rot}^2 = \pi G \mu_0 r^2 (I_0 K_0 - I_1 K_1)$. Here, $\mu_0 = M/L \times I$ is the central surface density, M/L is the mass-to-light ratio and I is the central surface luminosity. $I_{0(1)}$ and $K_{0(1)}$ are modified Bessel functions of the zeroth (first) kind evaluated at $\frac{r}{2r_0}$ where r_0 is the scale length. This mass-follows-light profile is akin to a Keplerian falloff beyond the turnover radius $r_{turn} = 2r_0 = 1.2r_e$, where r_e is the R -band effective radius. (This is for a purely exponential galaxy; for a bulge-dominated galaxy the turnover will be at a smaller multiple of r_e .) My measurements of μ_0 and r_0 come from fitting surface brightness profiles to SINGG photometry as described in Meurer et al. (2006).

I corrected for inclination using the optical axial ratio b/a from SINGG photometry, where b is the semi-minor axis and a is the semi-major axis, and the angle of inclination i is given by $\cos(i - 3^\circ) = \sqrt{((b/a)^2 - 0.2^2)/(1 - 0.2^2)}$, the factor of 0.2 is a correction for disk thickness and 3° is an empirical correction for optical vs. radio inclinations (Tully, 1988). I also corrected for the angle of misalignment ϕ between slit position angle and SINGG optical position angle. The misalignment is a function of the chosen slit mask position angle and the constraints of the instrument; the slit position angle must be $5^\circ < |PA| < 30^\circ$ with respect to the mask, limiting the choice of position angle. The total correction of dividing by $\sin(i)\cos(\phi)$ is made to the model curve after fitting to the optical data.

⁴The simplifying assumption that the ionised gas, neutral gas and stars within these systems have the same distribution is necessary for this work due to lack of additional observational data, as discussed in Section 4.4.3. Similarly, the data in hand do not allow me to separately account for a dark baryonic component, as expected from Bournaud et al. (2007).

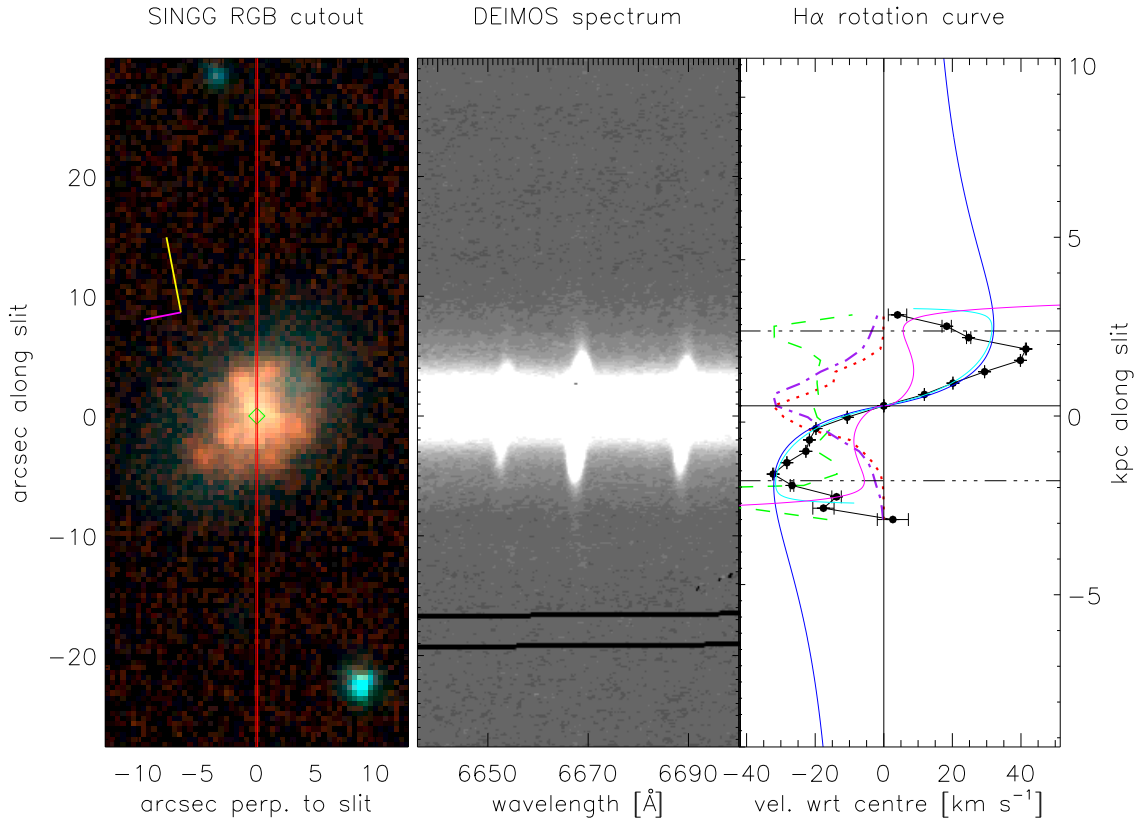


FIGURE 4.6: SINGG image, DEIMOS spectrum and rotation curve for HIPASS J0443-05:S4. (a) The left-most panel is the SINGG RGB image (R = R-band, G = narrow-band H α , B = net H α). Stars appear cyan and HII regions appear orange-red in this colour scheme. The red, vertical lines indicate the edges of the slit, which runs the length of this panel. The compass shows N in yellow and E in magenta. The green diamond shows the optical (SINGG) centre of the object, corresponding to (0,0) on this plot. (b) The central panel is a cutout from the DEIMOS spectrum, showing H α and [NII] emission lines. This is the same height in arcseconds as the left-hand panel. (c) The right-hand panel is also the same height in arcseconds as the other two panels, with a matching kiloparsec scale on the right-hand axis. It contains the observed (uncorrected) rotation curve in black dots. The H α flux and continuum flux in arbitrary units are shown as a red, dotted line and purple, dot-dash line respectively. Gaussian sigma H α width is depicted by the green dashed line, in the same km/s scale as the rotation curve. The crosshairs are centred on the continuum flux peak centre, which is not necessarily the same as the optical centre in the left-hand panel. The dash-dot-dot-dot lines show turnover radius $2r_0 = 1.2r_e$, assuming an exponential disk. The blue, solid curve is a mass-follows-light rotational velocity prediction based on SINGG photometry and fitted to the observed rotation curve within the turnover radius. The magenta, solid curve represents the pressure-supported component based on the velocity dispersion measurement. The cyan, solid curve is the total circular velocity given by the quadrature sum of the rotational and dispersion velocities. See text for details.

4.4.3 Pressure support

I also include modelling of the pressure-supported, velocity dispersion component, making the correction for asymmetric drift as in Meurer et al. (1996). In this case I model the dispersion of the HII regions instead of HI gas because resolved HI observations are not yet available for these galaxies. I note that the HII regions may have higher velocity dispersion than the neutral (and molecular) gas component; this is due to heating processes such as ionisation, supernovae and stellar winds, which happen on short ($\lesssim 10$ Myr) time-scales. The caveat associated with this treatment is therefore that the velocity dispersion may well be overestimated. Nonetheless, in the absence of resolved HI or CO observations, the HII region dispersion is the best available proxy for pressure support in the inter-stellar medium, so is adopted here.

The velocity dispersion σ_D as a function of radius r is given by $\sigma_D^2 = -r\sigma^2[\partial\ln(\Sigma_g)/\partial r + 2\partial\ln(\sigma)/\partial r - \partial\ln(h_z)/\partial r]$, where σ is the Gaussian sigma of the 1D H α velocity profile measured as described in the previous section, h_z is the vertical scale height of the disk and Σ_g is the gas surface density (Meurer et al., 1996). I notice that for most of the galaxies in my sample there is no obvious dependence of σ on the radius⁵, so I adopt a single median value for each galaxy. I also assume that h_z is constant with radius, so the dispersion component becomes simply $\sigma_D^2 = -r\sigma^2[\partial\ln(\Sigma_g)/\partial r]$. The H α light profile is clumpy for my sample of galaxies and difficult to fit for when modelling the Σ_g term. This necessitates the assumption that the ionised gas distribution is similar to the neutral gas and star distributions when compared to the usual dark matter component⁶ (Ryder & Dopita, 1994; Dopita & Ryder, 1994). On that basis I fit an exponential profile to the natural log-scaled continuum flux as a function of r , checking each case to confirm the fit.

The total circular velocity is then $v_c^2 = v_{rot}^2 + \sigma_D^2$. The three model components (rotational, dispersion, circular velocity) are overlaid on the observed rotation curve in Figure 4.6 and Figures 4.9 to 4.29. These values measured at r_{turn} are tabulated in Table 4.1. Mayer et al. (2001) measured pressure support contributions for hydrodynamical simulations of tidally-stirred dwarf galaxies (galaxies experiencing expansion due to weak tidal encounters, as in Aguilar & White, 1986). They found a high pressure support component $8 < \sigma_D < 30$ km s⁻¹, with a low total

⁵Except in the case of J0443-05:S4, which is accordingly modelled and discussed in greater detail in Subsection 4.4.7. In other galaxies, the peaks in dispersion (e.g. between SF regions) are not contributing to the pressure support as they are contaminated by background light, so I claim that a constant dispersion is adequate for this analysis.

⁶This assumption does not necessarily hold if there is no DM.

velocity contribution $v/\sigma_D < 0.5$. More recently, Green et al. (2014) analysed a population of local, gas-rich, star-forming galaxies in the DYNAMO survey, measuring $\sigma_D \sim 50 \text{ km s}^{-1}$ and $2 < v/\sigma_D < 10$. The galaxies in DYNAMO cover a similar range of morphologies to this work (rotating discs, perturbed rotators, complex kinematics, compact), but extend to higher masses. It is worth noting that Green et al. (2014) did not observe any dependence of v/σ_D with stellar mass. Interestingly, my sample appears to be consistent with the dispersion of tidally-stirred dwarfs, at $\sigma_D = 13.1 \pm 1.9 \text{ km s}^{-1}$, but with overall velocity contribution of larger galaxies, with $v/\sigma_D = 3.0 \pm 1.4$. This suggests that these dwarfs are experiencing galaxy harrassment (tidal disruptions to their velocity fields), and is consistent with the disturbed rotation curves I observe.

4.4.4 Rotation curve quality

Reliable mass-to-light ratios are dependent on good quality observations. Unfortunately, not many of the rotation curves in this sample are simple to analyse: several are disturbed, and others have multiple SF regions or possible counter-rotating cores. In my case I restrict my M/L analysis to the galaxies that meet the following criteria:

1. $\sin(i)\cos(\phi) > 0.4$, so there is neither a large correction for galaxy inclination nor for misalignment between slit and galaxy position angle; and,
2. not very small and faint, so that the photometry is reliable (this cutoff is effectively between galaxies in the original SINGG sample and fainter galaxies identified in this work); and,
3. not otherwise strongly disturbed (e.g. Fig. 4.28).

The resulting sample then consists of ten dwarf galaxies that constitute Sample A, out of 22 for which I have DEIMOS measurements. The galaxies within Sample A are indicated in Table 4.1.

The fraction of my sample that meets criterion (i) is 60% (Sample A, plus three that pass criterion (i) but fail criteria (ii) and (iii)). I calculate the expected fraction that meets the first criterion as follows. The position angle misalignment is given by $\phi = PA - 30^\circ$, when the galaxy position angle with respect to the mask is $30^\circ \leq PA \leq 90^\circ$, and by $\phi = 0^\circ$ when $0^\circ \leq PA < 30^\circ$. For a randomly-oriented galaxy, a PA of 45° then gives a median $\phi = 15^\circ$. Half of a sample of such galaxies should therefore have $\phi \leq 15^\circ$. Solving $\sin(i)\cos(15^\circ) > 0.4$ for i gives a minimum

inclination of 23° , below which the amplitude in the rotation curve rapidly becomes too low to measure. For a randomly-selected sample, the frequency of any given inclination should be constant⁷, so up to $\sim 3/4$ of galaxies are more edge-on than this. The resulting expected fraction of galaxies that meets my first criterion is therefore $1/2 \times 3/4 = 37.5\%$; considerably lower than the 60% in my sample. This difference is most likely attributable to triaxiality of the irregular galaxies, as well as group effects causing a non-random orientation in position angles in my sample. In particular, there is hint of a stream of dwarf galaxies in J1051-17 (see Fig 4.2), which will be discussed in a forthcoming paper (Kilborn et al., 2014, in prep).

4.4.5 M/L ratios

I test for the presence of DM by calculating M/L ratios through fitting model curves to observed rotational velocity as described above. A high M/L ratio implies the presence of DM and a normal hierarchical formation mechanism. In general the M/L ratios in this sample are low, but not dramatically so, at a mean M/L ratio of $0.73 \pm 0.39 M_\odot / L_\odot$. Low M/L ratios in general simply confirm that these are young galaxies forming stars. Some of my wider sample do not have sufficient signal at radii $> r_{turn}$, so that my modelling calculates lower limits on masses and mass-to-light ratios. However, this does not affect Sample A, which all have reliable measurements within r_{turn} and are well-modelled.

I plot M/L ratios as a function of the luminosity-metallicity relation using Sample A in Fig 4.7. While sparse, the data suggest a trend towards higher mass-to-light ratios with higher luminosity. This is consistent with the view that the luminosity-metallicity relation arises from the deeper potential well of larger galaxies, which makes them more able to retain metal-rich supernovae ejecta (Gibson & Matteucci, 1997; Kauffmann et al., 2003).

Unfortunately, none of the strong TDG candidates identified above is part of Sample A, so I cannot include any of them in this analysis. In essence this is because none of the three has a well-behaved mass-follows-light rotation curve: J1051-17:g11 has no detectable H α on the southern semi-major axis, and a large correction for inclination; J1059-09:S10 is bulge-dominated; J1403-06:595 has a disturbed rotation curve. An improved strategy for identifying TDGs in this manner is: 1) measure metallicities with low-resolution spectra of as many galaxies as possible in a field, preferring those with easiest (edge-on) inclinations; and 2) measure

⁷This assumption holds for inclined disks; there is a lower chance of seeing a triaxial galaxy face-on (van den Bergh, 1988).

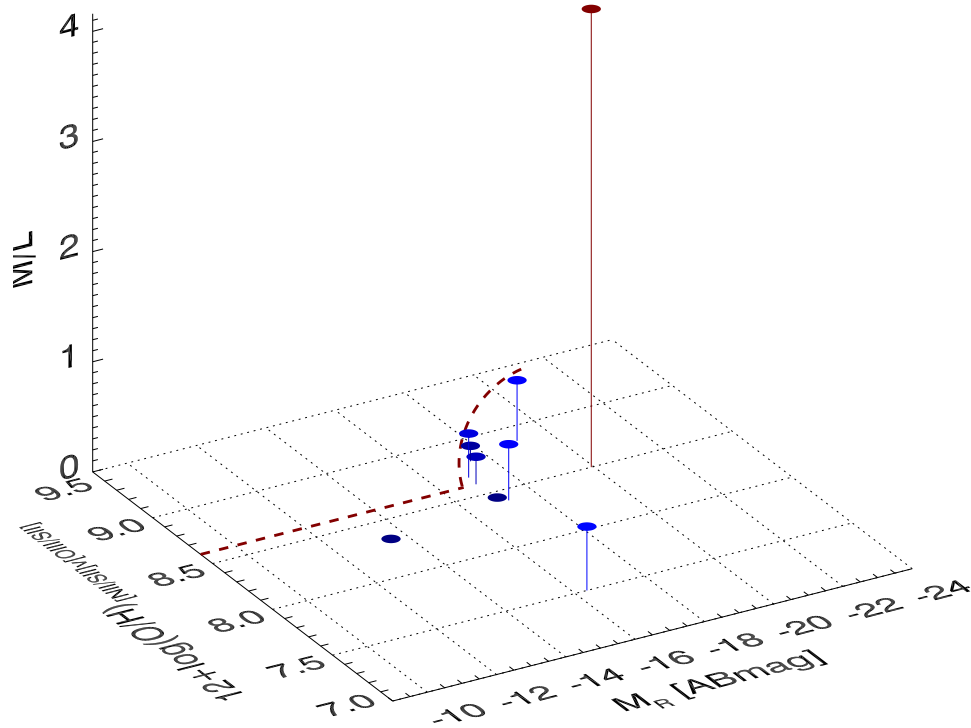


FIGURE 4.7: Mass-to-light ratio as a function of the luminosity-metallicity relation for the galaxies in my sample that have reliable mass-to-light ratios. The data points are colour-coded by mass-to-light ratio, with red being the highest and blue the lowest in this sample. The red, dashed line is the strong TDG candidate diagnostic line as defined in Chapter 3 (Sweet et al., 2014).

rotational velocity with medium-resolution spectra of a subset of these, either optimising slit orientation for the high-metallicity candidates, or using an integral field unit spectrograph. In this way the effects of large inclination / position angle corrections can be minimised. However, this strategy does not take into account tidally disturbed or stripped matter at the outskirts of target galaxies, leading me to consider that problem in Subsection 4.4.6.

4.4.6 Can the falling rotation curves of TDGs be detected?

In order to confirm a tidal dwarf galaxy by its rotation curve when the M/L ratio is not known *a priori*, it is necessary to measure its velocity to sufficient radii to detect any fall in velocity consistent with the predicted mass-follows-light model curve⁸. In principle, because of the

⁸Other tracers of DM exist, such as atomic and molecular gas kinematics from line-widths, but these require more sensitive observations and are consequently outside of the scope of this work.

gradual, Keplerian fall-off, this translates to measurements of at least twice the turnover radius $r_{turn} = 1.2r_e$. This measurement becomes difficult at an exponential rate if it is assumed that H α emission has the same profile as continuum light. In practice, however, there are two bigger issues with measuring the rotation curve of a TDG.

Firstly, the H α emission may be clumpy and more centrally-concentrated than the continuum light, making the measurement more difficult than predicted. I define detectability radius r_{det} , a function mostly of the distribution of the H α light but also influenced by the proximity to other SF regions (e.g. see the discussion for J1051-17:S7 in Figure 4.14). Detectability becomes an issue if $2r_{turn} \gtrsim r_{det}$. This can be visualised in Figure 4.6 and Figures 4.9 to 4.29, with H α flux as a function of radius plotted as a red, dotted line. If the H α light is *less* centrally-concentrated than predicted by the continuum light, then this criterion works in my favour because the measurement at large radii is easier to make than for a simple exponential. Either way, one must assume that the velocity of HII regions is representative of the dwarf galaxy that contains them. This will often be the case, even if the HII region is very large and non-central, as seen in Richards et al. (2014, MNRAS submitted). However, this will not be the case if the region is being removed due to tidal forces - as in the second issue.

Secondly, the more critical issue is that the tidal field that forms a TDG may be strong enough that outer baryonic matter is stripped off, making the measurement impossible. I note that for a normal dwarf in this scenario its DM halo will inhibit stripping from occurring. Tidal stripping becomes a problem when $2r_{turn} \gtrsim r_{tidal}$, where $r_{tidal} = 0.4d(m/M)^{1/3}$ is the tidal radius of the dwarf galaxy (for a fluid, triaxial satellite, as in Shu, 1982); d = distance of closest approach, m = mass of dwarf galaxy, M = mass of giant host galaxy. It is worth noting that the velocity field will be disturbed even before the proximity criterion for stripping is reached. As discussed in (Renaud et al., 2009), tidal fields can be compressive as well as destructive depending on the shape of the potentials involved; indeed it is this mechanism that is responsible for the formation of TDGs. Aguilar & White (1986) also pointed out that while strong tidal encounters decrease the effective radius of a galaxy, weak encounters puff up the galaxy instead. Indeed, the strong dispersion component in many of my dwarfs may be evidence of such tidal stirring taking place. This disturbance is also problematic for a sound measurement of a rotation curve. However, I do not attempt to quantify this here for the sake of simplicity in this analysis.

I calculate r_{tidal} for each galaxy in my sample, assuming $d = \sqrt{2}d_{proj}$, where d_{proj} = projected distance to the nearest large galaxy, and the factor of $\sqrt{2}$ is based on a 45° projection angle. This is assuming that the current deprojected distance is the distance of closest approach. It

is clearly very likely that this is not in fact the closest approach because the dwarf galaxies are most probably either on their way towards or away from the nearby giant, so will be closer in the future or have already been in the past. Therefore I am overestimating the tidal radius. For this calculation I also assume a dynamical M/L ratio for ‘dwarfs’ (galaxies with $M_R > -22$) of $1 M_\odot/L_\odot$, and $4 M_\odot/L_\odot$ for ‘giant’ ($M_R < -22$) galaxies, consistent with McGaugh & de Blok (1998); Toloba et al. (2011); Kalinova et al. (2013). This gives a mass ratio m/M of $1/4(l/L)$, where l and L are the luminosity of the dwarf and giant galaxy respectively, so that $r_{tidal} = 0.4\sqrt{2}d_{proj}(l/4L)^{1/3}$.

In Fig. 4.8 I plot r_{tidal} vs. r_e ; the dashed line indicates the required radius of $2r_{turn}$. Four of the 22 galaxies in my sample fall below this line, indicating that these could not be confirmed as TDGs because no baryons remain bound where the rotation curve is falling. A further five to six galaxies are borderline. Others in this sample could also be undetectable, given that the tidal radius is likely overestimated. Clearly, a large r_{tidal} is required for a galaxy to be confirmed as a TDG; that is, the dwarf must be far from the nearest giant. However, the further away from the giant, the less likely the dwarf is to be formed in a tidal manner (*c.f.* J0443-05:S3, which has the largest r_{tidal} in the sample, and a DM-rich rotation curve, so is not a TDG). Further to this, I reiterate that the $2r_{turn}$ detection limit only indicates where the falling-velocity baryons do not remain bound. If a dwarf galaxy lies above this line then those baryons remain bound, but there must also be sufficiently bright H α light to meet the detectability radius r_{det} criterion discussed at the start of this section before the galaxy can be confirmed as a TDG. Even with these DEIMOS observations only three (14%) galaxies have $r_{det} \gtrsim 2r_{turn}$ (shown as yellow pentagons in Fig. 4.8): J0443-05:S3, J1051-17:S5, J1059-09:S7. None of these has a falling rotation curve, so none are true TDGs.

This effect is problematic for TDG candidates in the literature that have been identified based on their location within tidal streams, because the strong tides distort the rotation curves and dynamical M/L ratios. This is clear in the work by Mendes de Oliveira et al. (2001), who used velocity gradients to ascertain whether or not star-forming regions within tidal tails in Stephan’s Quintet would remain bound, forming TDGs. None of the rotation curves shows a fall-off in velocity, and all are severely disturbed by the tidal field. The M/L ratios measured are inflated (5-73 M_\odot/L_\odot), requiring DM in opposition to predictions. It may be argued that one can do better with HI measurements, probing to larger radii than H α is often observed at. For example, Carignan & Purton (1998) detected a declining rotation curve for DDO154 and measured its ‘total’ mass. In that case, this was possible because DDO154 is isolated,

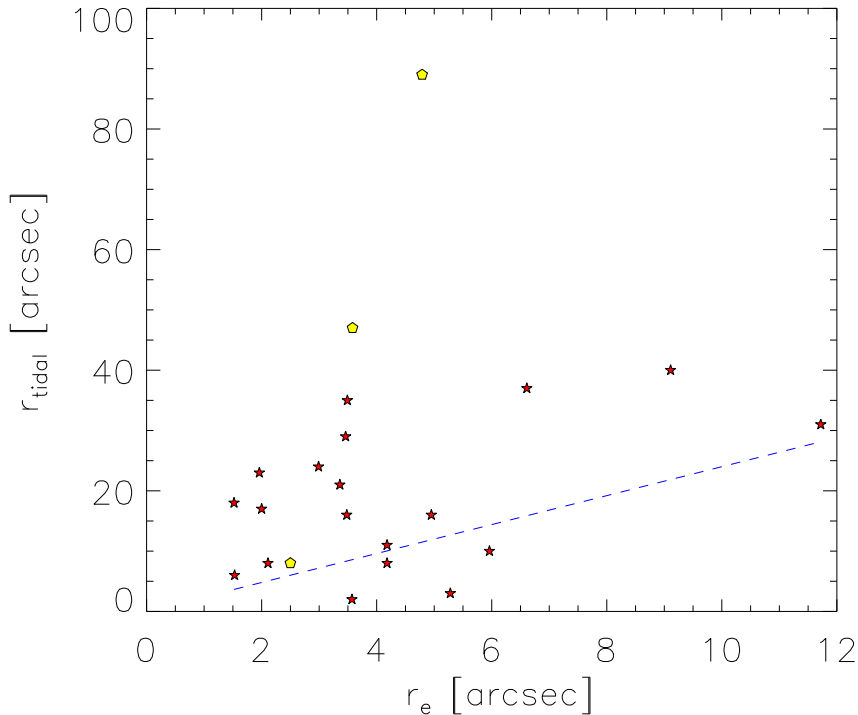


FIGURE 4.8: Tidal radius vs. effective radius for my sample of galaxies. See text for calculation of tidal radius. The blue, dashed line indicates nominal detection limit of $2r_{turn} = 2.4r_e$. Below this limit it is not possible to detect a falling rotation curve because those baryons are tidally removed. Yellow pentagons represent the galaxies in my sample that have measurable $H\alpha$ beyond $2r_{turn}$; the galaxies that are not measurable at that radius are shown as red stars.

and therefore not tidally truncated, which is rarely the case. However, this mass includes a substantial DM component and therefore rules out a tidal origin for this galaxy. Measurements of falling rotation curves remain difficult except for a few select cases.

4.4.7 The strongly-falling rotation curve of J0443-05:S4

My best candidate for a tidal dwarf galaxy based on metallicity and rotation curve is HIPASS J0443-05:S4 shown in Fig. 4.6. This galaxy has a metallicity $12+\log(O/H)=8.86$ and R -band magnitude $M_R=-19.07$, placing it within the luminosity-metallicity relation defined by the SDSS control sample. However, it is near a giant spiral S2 which has a metallicity just 0.32 dex higher at $12+\log(O/H)=9.18$ and $M_R=-22.57$. I note that these differences in magnitude and metallicity are similar to those measured in the M31-M32 system ($\Delta\text{mag} = 4.43$; $\Delta\text{metallicity} = 0.22$ dex; Richer et al., 1998), for which a tidal *encounter* has been proposed (e.g. Faber, 1973; Bekki et al., 2001; Choi et al., 2002).

This galaxy's rotation curve is falling rapidly beyond the turnover radius r_{turn} , indicating that

no dark matter is required to explain its observed velocity. In fact, it shows a significant downturn *below* the mass-follows-light profile shown in blue, even reaching zero at the outskirts of the galaxy. This galaxy is near my nominal detection limit of $r_{\text{tidal}} = 2r_{\text{turn}}$, indicating that there could be tidal warping of the rotation curve. However, the symmetry of this system suggests that it is not experiencing extreme tidal forces, so I do not believe that tides are causing the severe downturn. The rapidly-falling rotation curve is not consistent with the predictions for a TDG, and the lack of evidence for tides corroborates this. The error bars (derived from the peak location error in the χ^2 -minimisation fit to the H α line) indicate that low S/N is not responsible for the unusual shape of this rotation curve. Nor can the downturn be attributed to instrumental signatures or residual sky lines; the same shape is observed for other emission lines falling in other locations on the detector.

I have three hypotheses for the sub-mass-follows-light relation exhibited by the measured rotation curve: 1) a rotating disk that becomes increasingly pressure-supported at large radii; 2) a face-on disk surrounding a bar that is tilted away from a face-on orientation; 3) a kinematic twist where the disk is warped.

Firstly, the image panel of Figure 4.6 indicates a ring of concentrated HII regions (appearing orange-red) with a surrounding halo of stars (shown in cyan). This structure is also evident (and slightly more resolved) in SDSS imaging. I also note the upturn in dispersion (green, dashed line in the rotation curve panel), which is robust against a change in bin size, and evident in the spectrum cutout. The imaging and the upturn in dispersion together lead me to model the pressure-supported component in more detail for this case. I fit an exponential profile to the dispersion correction and follow the methods of Meurer et al. (1996) again, but this time including the now non-zero $2\partial\ln(\sigma)/\partial r$ term. The resulting correction σ_D is shown in magenta, and the total circular velocity in cyan. The negative contribution of the pressure-supported component gives a falling total circular velocity. This suggests that I have detected a rotating disk that becomes pressure-supported at large radii, though it is not clear what would cause the increased velocity dispersion at the outskirts.

Secondly, I propose that the central, rising velocity profile could belong to a tilted bar, and the falling profile to a face-on disk with no measurable rotation. The observed morphology hints at a central bar, though more detailed imaging is required to confirm this. A polar ring structure like this is unusual in a dwarf (cf. De Rijcke et al., 2013), but could conceivably arise as a tilt to the galaxy's existing disk, triggered by an interaction with the neighbouring giant S2, if not the typical (for giant polar ring galaxies) method of accreting material from the nearby

galaxy (Athanasoula & Bosma, 1985). The size of the bar relative to the disk in this scenario is reminiscent of the morphological (*c.f.* dynamical) bar of the LMC⁹, as is the dwarf-giant separation (~ 50 kpc in both cases). van der Marel & Kallivayalil (2014) recently measured the LMC (stellar) rotation curve, but due to the high degree of scatter in the stellar velocities there is no clear trend in the outskirts of the galaxy with which to compare J0443-05:S4.

My third hypothesis is that I am observing a kinematic twist or warp, where the kinematic position angle varies smoothly with radius (Krajnović et al., 2008). Kinematic and isophotal twists are caused by bars, often occurring with spiral arms (e.g. VCC0523, Ryś et al., 2013) or shells (e.g. Figure 5 of Emsellem et al., 2006). For a good visual example of an isophotal twist see Elmegreen et al. (1996), especially their Figure 1 (NGC1300 I). A twist of this magnitude could cause the line of nodes (region of zero velocity) to lie in the edges of a poorly-aligned slit, mimicking a falling rotation curve such as I observe for J0443-05:S4. Indeed, the minor axis rotation curve of NGC1068 (Emsellem et al., 2006) shows a similar falling rotation curve to ours.

To distinguish between these three degenerate scenarios I require additional data, in the form of integral field spectroscopy.

4.5 Chapter Summary

In this chapter I presented DEIMOS observations of a sample of 22 star-forming dwarf galaxies in gas-rich groups. After prioritising my known group members in the slit mask design, I placed spare slits on as many sources as possible, with preference to extended (i.e. galaxy-like) sources. In doing so I identified six additional small galaxies as new members of two of my groups.

I measured metallicity of those galaxies within my sample that have the necessary strong emission lines and found three new very strong TDG candidates (J1051-17:g11, J1403-06:595, J1059-09:S10).

I constructed rotation curves for the dwarf galaxies in my sample and modelled the total circular velocity as the quadrature sum of rotational velocity (set by a mass-follows-light fit to the central regions of each galaxy) and a velocity dispersion contribution. All but one of the galaxies show signs of rotation with a mean of 39.3 km s^{-1} at r_{turn} , but most of the velocity fields are disturbed so that a mass-follows-light profile fits neither on its own nor with a DM

⁹To be clear, the LMC is not considered by most to be a TDG.

component. The galaxies have a proportionally large pressure support component on average at $\sigma_D = 13.1 \pm 1.9 \text{ km s}^{-1}$, consistent with tidally-stirred dwarfs. The generally disturbed nature of the velocity fields and the large amount of dispersion indicate that these galaxies are experiencing weak tidal fields.

M/L ratios in my sample are low ($0.73 \pm 0.39 M_\odot / L_\odot$), indicating that the stellar populations in these galaxies are young, consistent with their high rates of star-formation. There is some suggestion of a trend of M/L ratio with luminosity in my sample, with fainter galaxies having lower mass-to-light ratios.

One galaxy in my sample, J0443-05:S4, has a strongly-falling rotation curve, reaching zero velocity at the outskirts of the galaxy. I propose that I may be observing 1) a rotating, star-forming disk that becomes pressure-supported at large radii; 2) a tilted bar with a face-on disk; 3) a kinematic twist, with the line of nodes falling within the edges of the slit.

Even with very high sensitivity DEIMOS data, it remains difficult to convincingly measure the falling rotation curve of a TDG, due to both physical and observational effects. Observationally, the limitations of slit - galaxy position angle alignment severely constrain my ability to reliably measure kinematics of all galaxies in a group. To overcome these observational effects, integral field unit spectroscopy should be employed. For DEIMOS with a constraint of $\pm 30^\circ$, I have reliable measurements for 60% of my sample. This is considerably greater than the predicted 37.5%, suggesting that the position angles of the galaxies are aligned, probably due to group effects.

Physically, many of the rotation curves in my sample are disturbed due to recent interaction, or are not smooth due to having multiple star-forming regions. In addition to this the outskirts of many of the dwarfs may be tidally stripped by interactions with neighbouring galaxies. As much as half of my sample could be affected by this. Even in the absence of tidal stripping, H α light rapidly becomes progressively fainter beyond the turnover radius if it follows the stellar mass distribution. Only 14% of my sample has detectable H α light at sufficient radii to measure any fall in rotation curve; none of these has a falling rotation curve, so none is a TDG. It seems that falling rotation curves expected of TDGs can be detected only rarely, if at all.

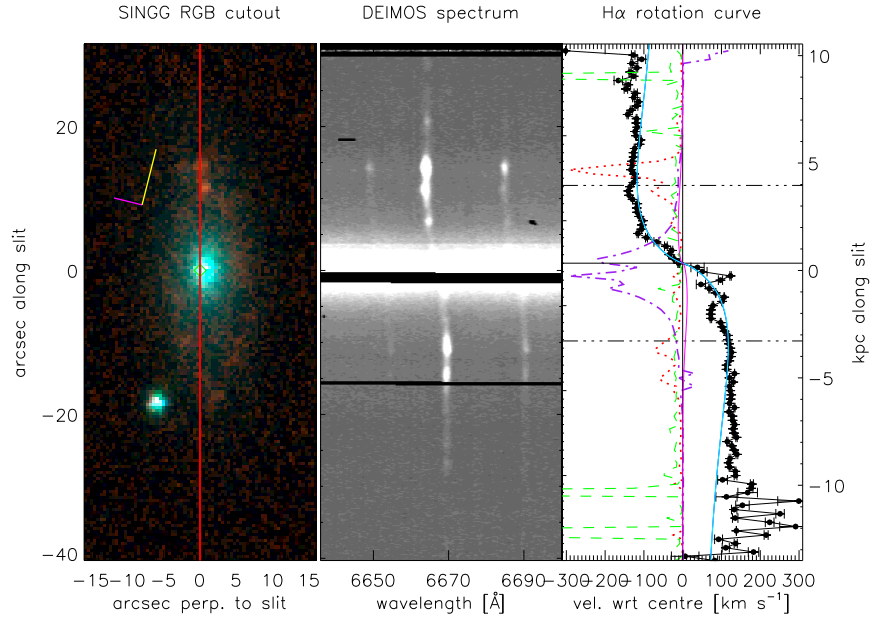


FIGURE 4.9: J0443-05:S3. The layout of this figure is the same as for Figure 4.6. This galaxy is the most ‘normal’ in my sample, with a small stellar bulge (cyan) surrounded by a star-forming disk (red), and a flat rotation curve, consistent with a DM halo. Its tidal radius is much larger than its effective radius, borne out by the large radius to which I measure a typical rotation curve. It also has a below-average amount of pressure support and the highest M/L ratio in my sample at $4.15M_{\odot}/L_{\odot}$.

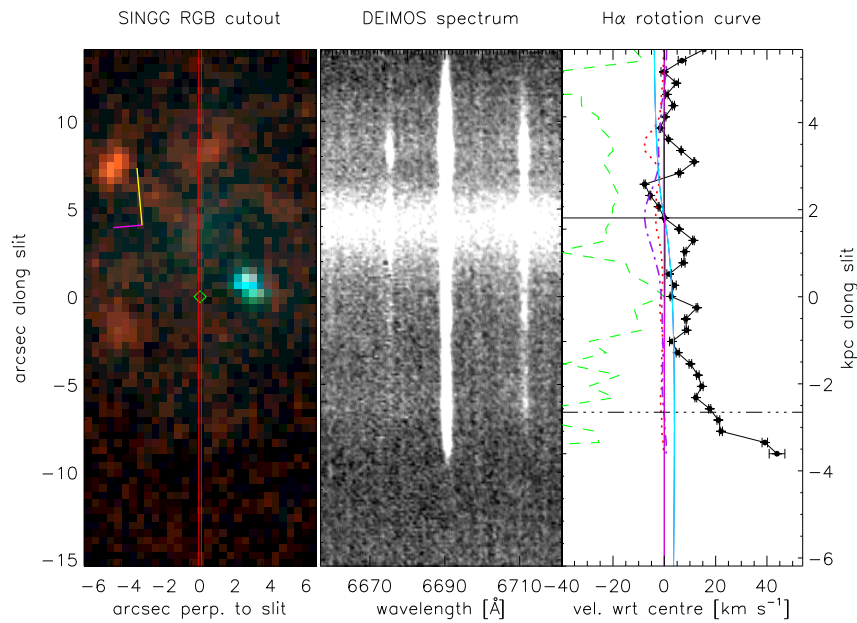


FIGURE 4.10: J1051-17:S3. The layout of this figure is the same as for Figure 4.6. This galaxy is face-on, so no meaningful velocity field is measurable.

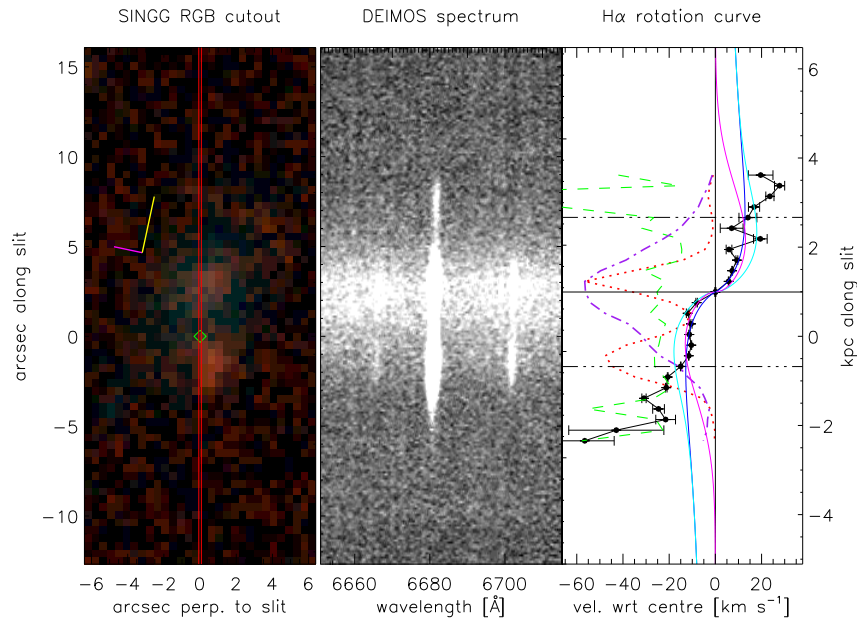


FIGURE 4.11: J1051-17:S4. The layout of this figure is the same as for Figure 4.6. This galaxy has three separate HII regions with a linear velocity gradient, consistent with solid body rotation. There is a substantial amount of pressure support in this galaxy. The observed rotation rises above the model predictions, suggestive of the presence of DM. It has a low M/L ratio ($0.58M_{\odot}/L_{\odot}$), consistent with most of the dwarfs in my sample.

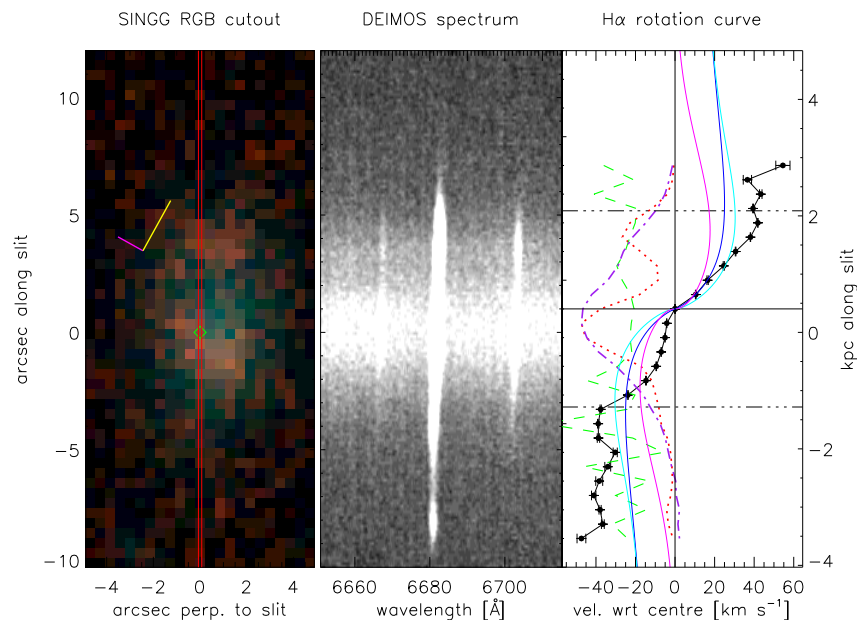


FIGURE 4.12: J1051-17:S5. The layout of this figure is the same as for Figure 4.6. There appear to be two SF regions to this galaxy. The velocity profile of this galaxy is not well fit by the canonical mass-follows-light rotation curve. However, this galaxy lies well above the detection limit set by r_{tidal} , so is not likely suffering from tidal effects.

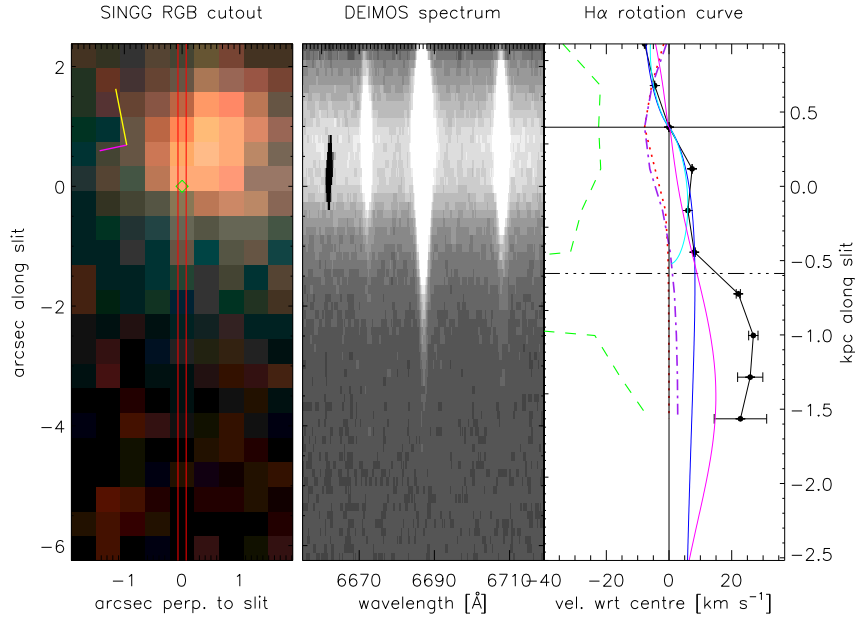


FIGURE 4.13: J1051-17:S6. The layout of this figure is the same as for Figure 4.6. This blue compact dwarf galaxy is dominated by pressure support instead of rotational velocity. Its observed velocity profile is distorted beyond r_{turn} by the nearby giant S1. A slit placed on the edge of S1 prevented this slit from spanning the length of S6.

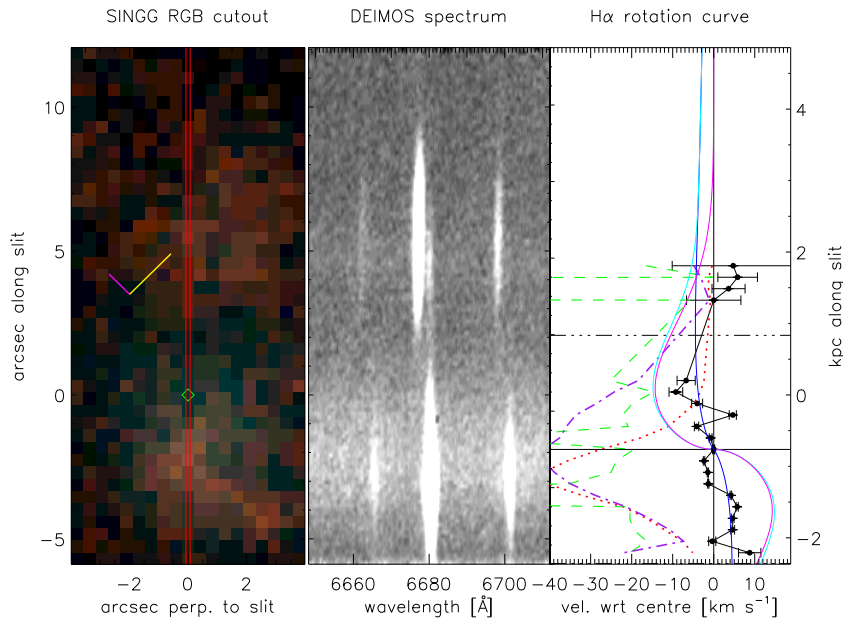


FIGURE 4.14: J1051-17:S7. The layout of this figure is the same as for Figure 4.6. S7 is the brighter feature to the SW of the slit (that is, the bottom of this figure). Also measured in this slit is an HII region in the plane of the disk of S1 ('S7a'), towards the top of this figure. The velocity field shown here is that of S7 only. It is disrupted, consistent with this galaxy having recently passed through the disk of S1 and possibly inducing star formation in S7a. There is also a large amount of dispersion contribution.

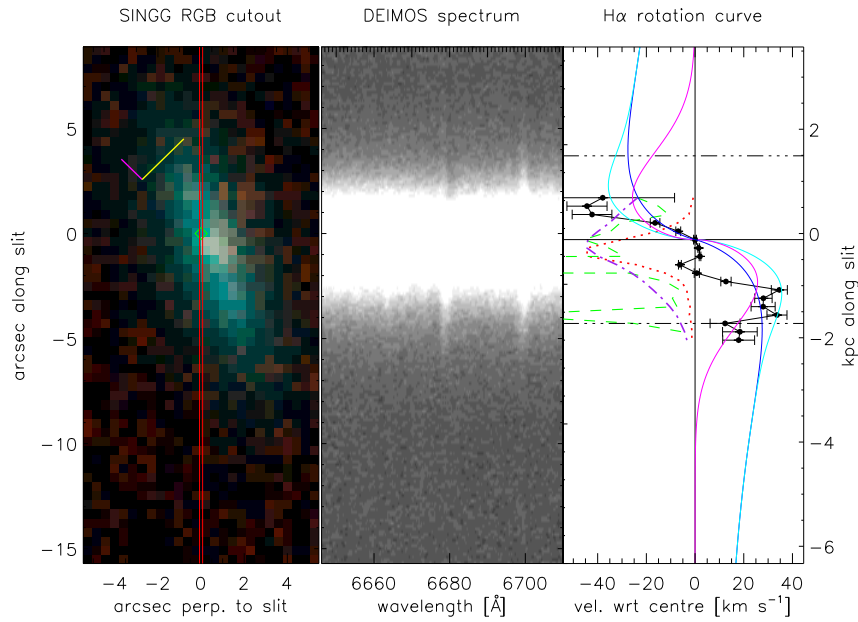


FIGURE 4.15: J1051-17:S8. The layout of this figure is the same as for Figure 4.6. The velocity field of this galaxy is suggestive of a mass-follows-light profile with a kinematically decoupled core. The faint $H\alpha$ emission of this galaxy and bright continuum at the centre makes the velocity field difficult to measure beyond the measurements shown here, especially at the NE of the slit. The apparent $H\alpha$ absorption in the central panel is in fact an adjacent, poorly-subtracted sky line.

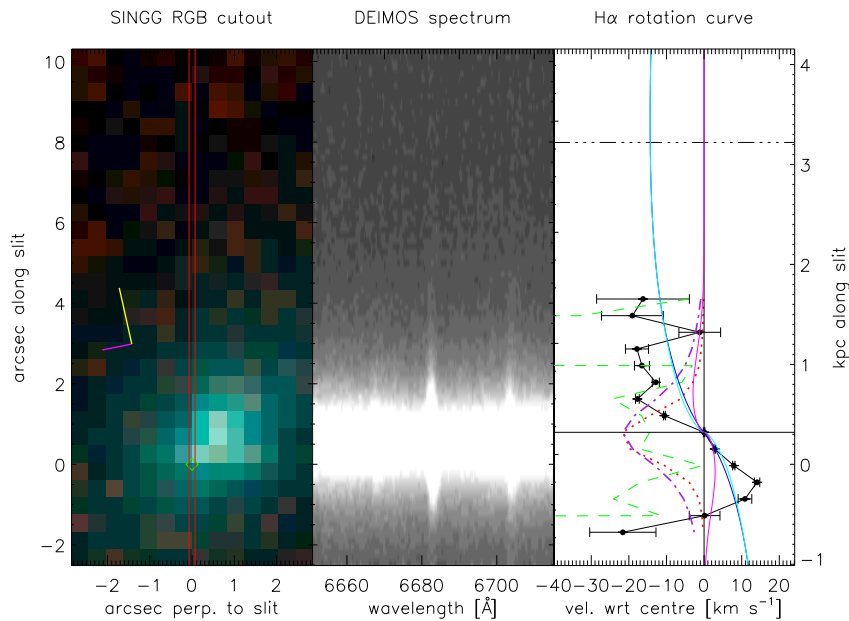


FIGURE 4.16: J1051-17:g04. The layout of this figure is the same as for Figure 4.6. The misalignment between optical and slit PAs prohibits sound measurement of this small, newly-identified galaxy.

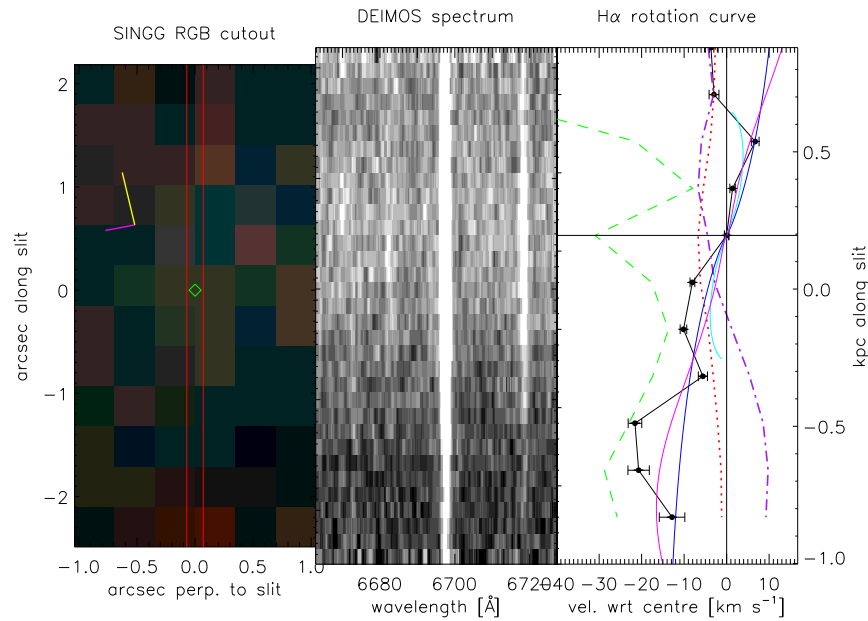


FIGURE 4.17: J1051-17:g07. The layout of this figure is the same as for Figure 4.6. This new, faint galaxy has strong $H\alpha$ emission but very faint continuum. The slit is not well-placed to measure the kinematics of this galaxy.

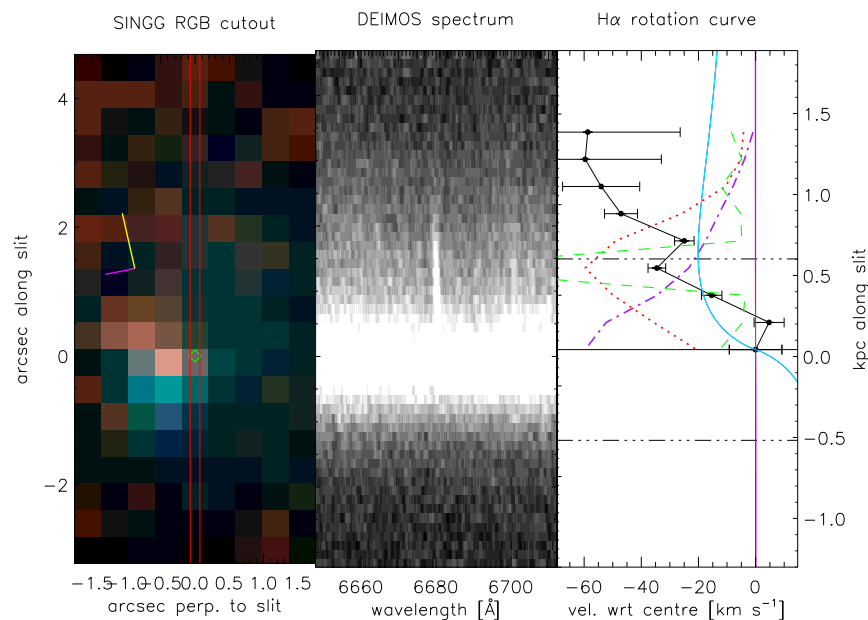


FIGURE 4.18: J1051-17:g11. The layout of this figure is the same as for Figure 4.6. For this new galaxy there is a very large correction for inclination / orientation. There are no observed data points below the continuum centre because there is insufficient $H\alpha$ light on this side of the galaxy. Its high metallicity leads me to classify this galaxy as a very strong TDG candidate.

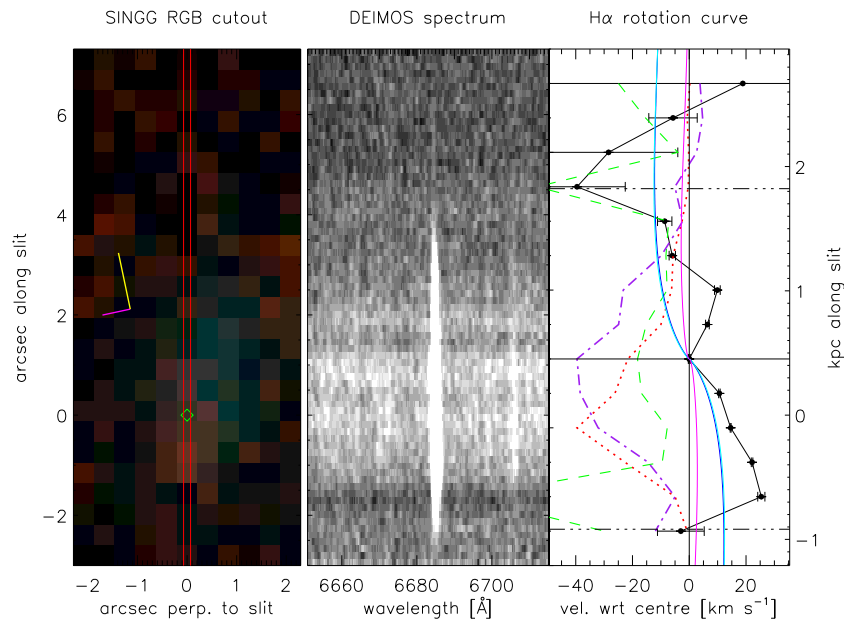


FIGURE 4.19: J1051-17:g13. The layout of this figure is the same as for Figure 4.6. This galaxy's inclination is uncertain, so it is difficult to measure its mass-to-light ratio. Its velocity field appears to be disturbed.

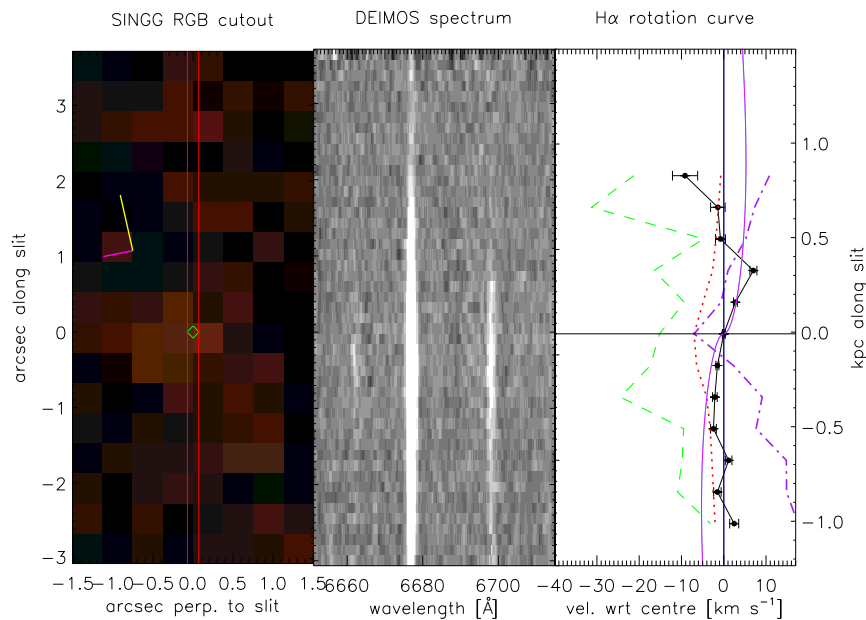


FIGURE 4.20: J1051-17:2905. The layout of this figure is the same as for Figure 4.6. This galaxy has very low surface brightness, so is barely evident in the SINGG image. It is well below the tidal stripping detection limit due to its small size and proximity to the giant S1. It may in fact be a HII region in the disk of S1.

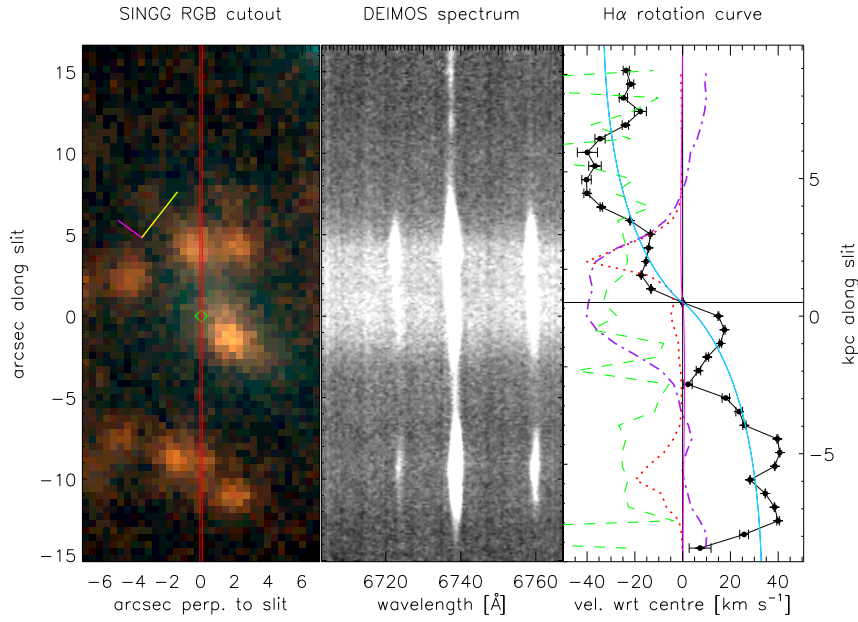


FIGURE 4.21: J1059-09:S2. The layout of this figure is the same as for Figure 4.6. This clumpy galaxy is consistent with a mass-follows-light profile. Note that the large corrections for slit position angle and galaxy inclination contribute to the large M/L ratio.

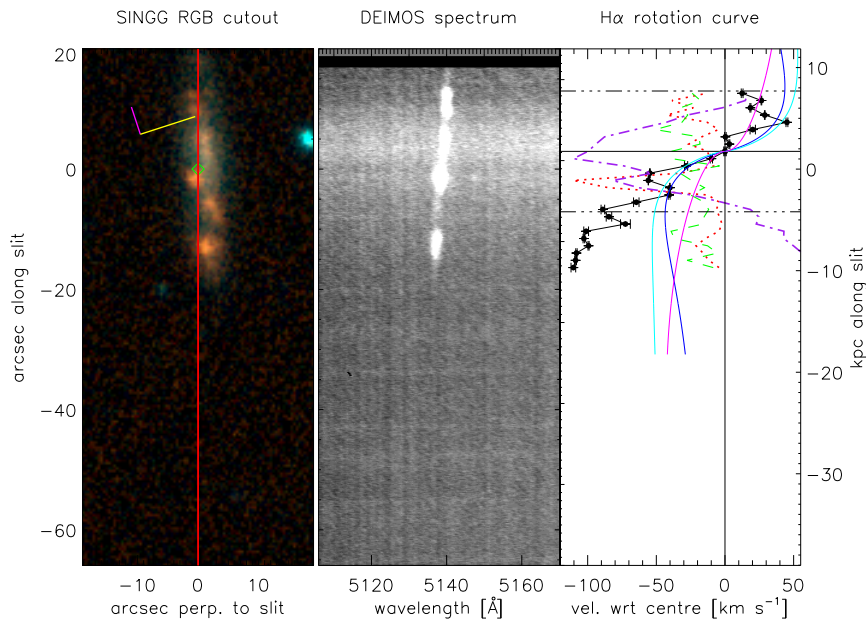


FIGURE 4.22: J1059-09:S5. The layout of this figure is the same as for Figure 4.6. For this slit, H α and [NII] lines fall on the edge of the CCD, so I opt for the [OIII] λ 5007 line to avoid any possible edge curvature errors. While the H α line is brighter and measurable \sim 1 kpc further out, it is not reliable because of proximity to the chip edge. The observed velocity rises above the model curves, suggestive of the presence of DM.

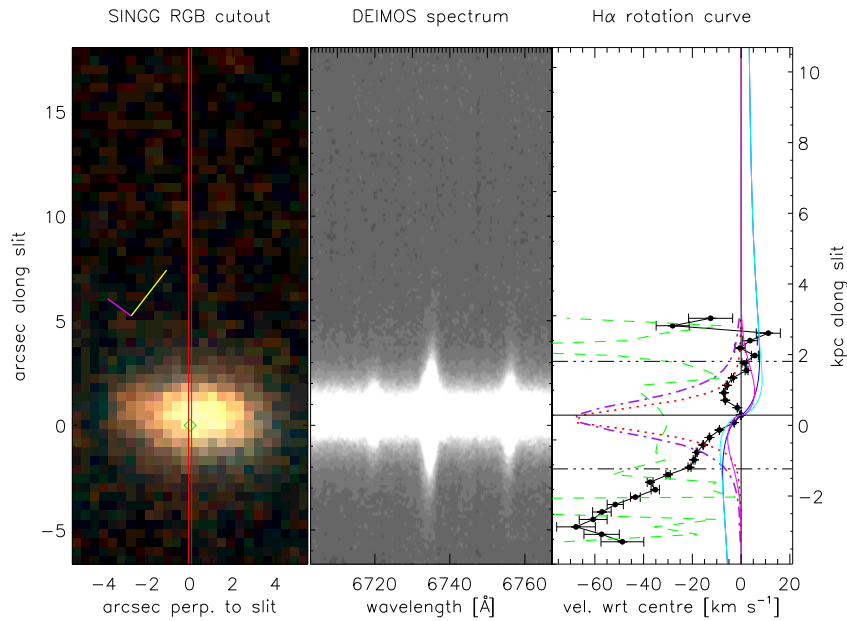


FIGURE 4.23: J1059-09:S7. The layout of this figure is the same as for Figure 4.6. The rotation curve of this blue compact dwarf galaxy has a very unusual shape. It is very near the interacting galaxies S1 and S3, so is likely to be tidally disturbed by them. Moreover, the slit is close to aligning with the minor axis of this galaxy, so the velocity gradient might well be due to a galactic wind.

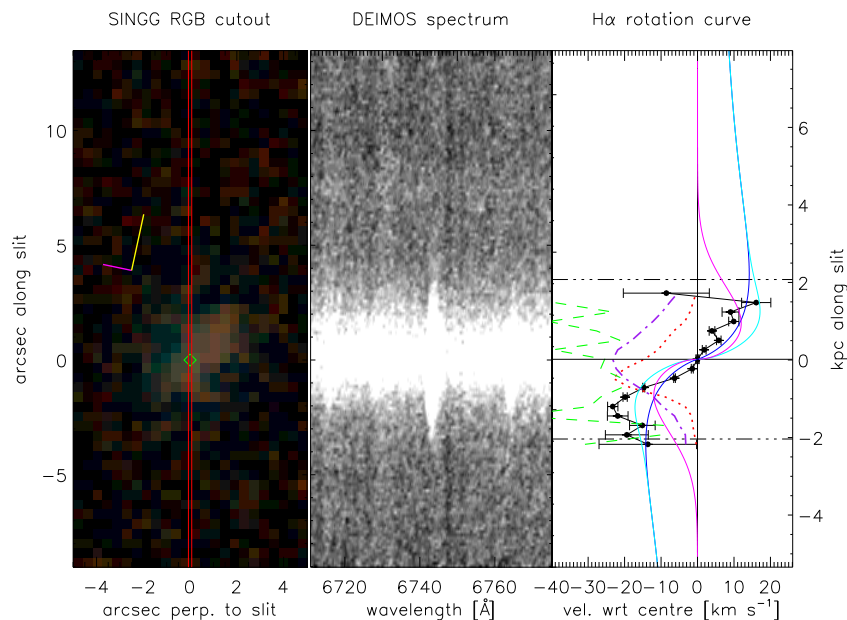


FIGURE 4.24: J1059-09:S8. The layout of this figure is the same as for Figure 4.6. Mass follows light for this small galaxy. It has a metallicity 2.5σ above the SDSS mean for its luminosity, so is a good TDG candidate. Moreover, it is near (in projected space) and may be related to the very high metallicity dwarf S10.

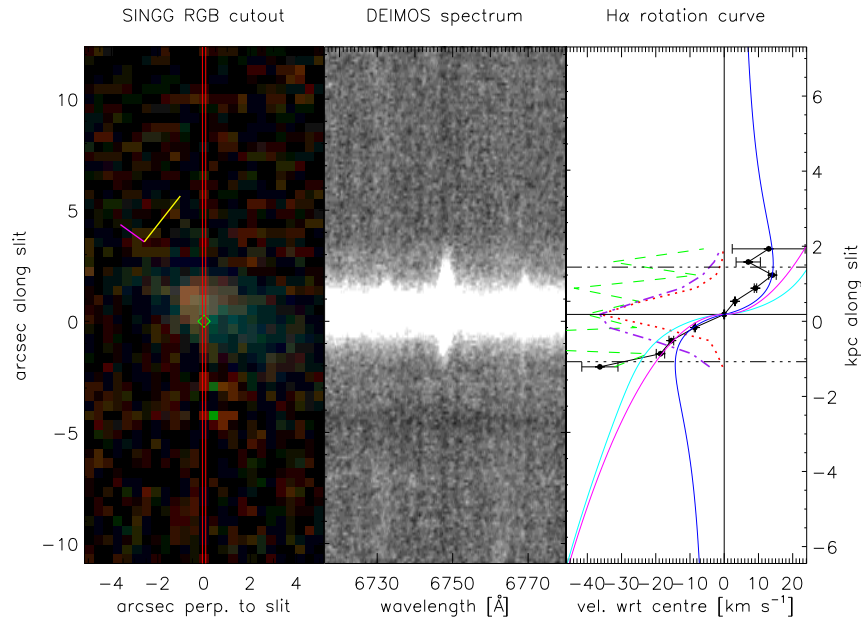


FIGURE 4.25: J1059-09:S9. The layout of this figure is the same as for Figure 4.6. This small galaxy is dispersion-dominated.

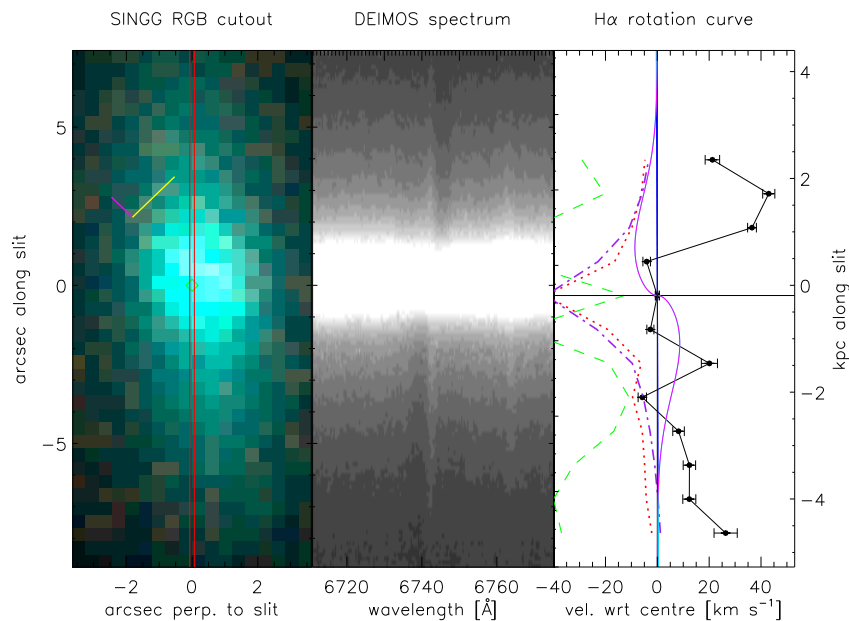


FIGURE 4.26: J1059-09:S10. The layout of this figure is the same as for Figure 4.6. This galaxy has a very strong bulge (as evidenced by large amount of dispersion and the blue colour in this figure), so cannot be treated as a pure disk. Its rotation curve is not well fit by a predicted mass-follows-light relation. However, there are strong signs of $H\alpha$ absorption indicating clear rotation of the stellar component. The galaxy has a high metallicity consistent with a TDG, but is not near a host, so must be an old TDG if it is one. It is near another dwarf (S8) whose high metallicity makes it a good TDG candidate.

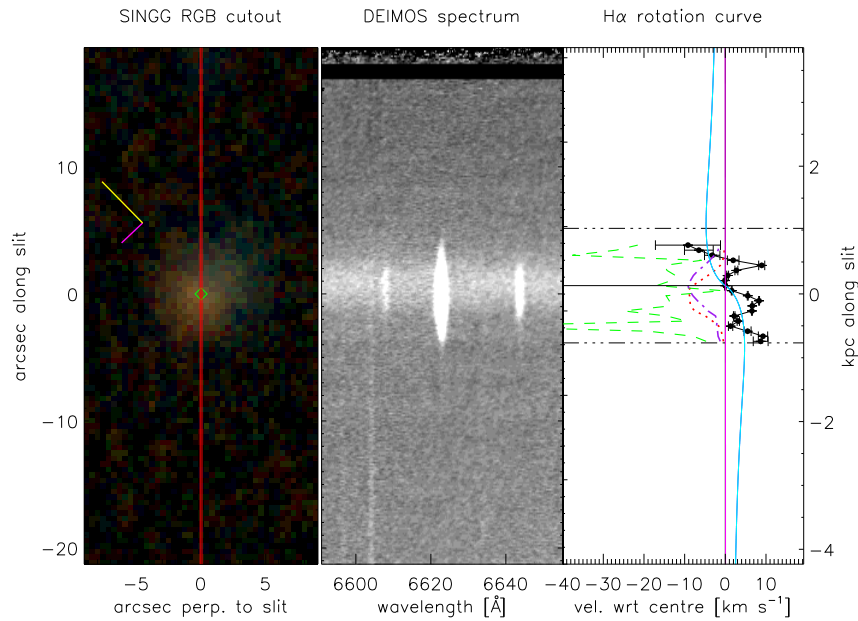


FIGURE 4.27: J1403-06:S3. The layout of this figure is the same as for Figure 4.6. This slit measures an offset HII region within a very low surface brightness dwarf galaxy, so it is difficult to claim rotation for this galaxy. It is only marginally detectable based on my r_{tidal} detection limit, and indeed I do not measure rotation past r_{turn} .

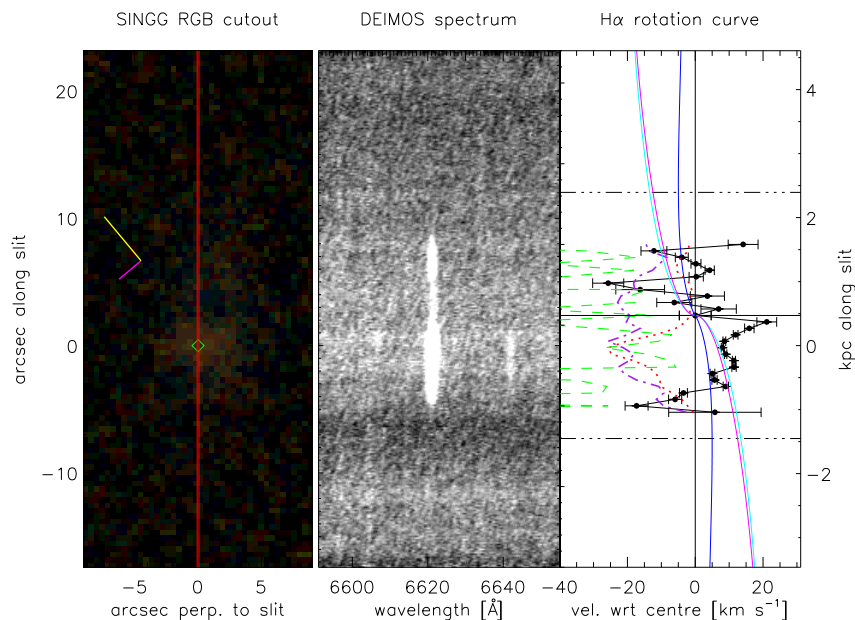


FIGURE 4.28: J1403-06:S4. The layout of this figure is the same as for Figure 4.6. This very low surface brightness galaxy consists of two HII regions likely disturbed by the two giant interacting galaxies S1 and S2. It is sufficiently small to lie below the detection limit set by r_{tidal} .

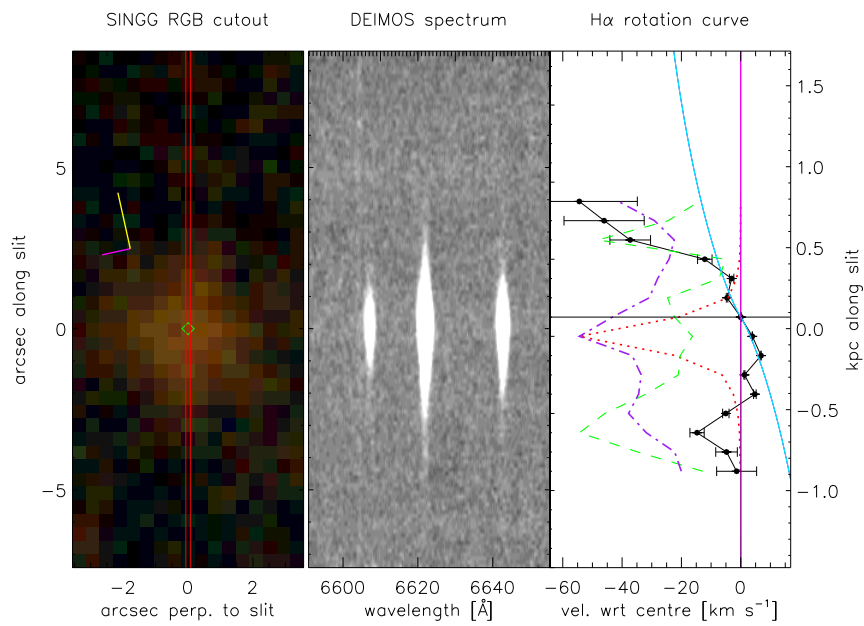


FIGURE 4.29: J1403-06:595. The layout of this figure is the same as for Figure 4.6. This appears to be a giant HII region within the halo of the giant galaxy S2. It has high metallicity consistent with a TDG, but a very warped rotation curve. Due to its small size and proximity to S2, it is well below the tidal stripping detection limit.

5

Conclusions

5.1 Motivation

In this thesis I presented new methods for the classification of tidal dwarf galaxies (TDGs). Existing TDGs in the literature are discovered by their location within the young tidal tails in which they form (e.g. in the Antennae galaxies; Mirabel et al., 1992), but these distort the TDGs' velocity field, demonstrating that they have not yet reached dynamical equilibrium. As a result there are no strong measurements of the falling rotation curves expected for TDGs (*c.f.* Carignan & Purton, 1998). Mass measurements are also inflated so it is not possible to confirm whether or not they are bonafide TDGs based on the absence of DM (Casas et al., 2012).

TDGs in the literature usually have high metallicity (e.g. Weilbacher et al., 2000; Weilbacher et al., 2003; Sweet et al., 2014; Duc et al., 2014) because they form from the pre-enriched material within the tidal tails of the giant galaxies (Bournaud, 2010). However, these metallicity measurements are calibrated using different methods because of the properties of the samples from which they are drawn. The different calibration methods give vastly different results, so

it is not possible to compare a galaxy measured with one method to a control sample measured with another (Kewley & Ellison, 2008).

5.2 Aims

The general aims of my research were to develop new methods for the identification and measurement of TDGs, in an attempt to overcome the existing problems discussed above. Specifically, the first aim was to select a representative sample of groups without tidal streams but where the properties of these dwarfs could be efficiently measured. The second aim was to consistently measure metallicities and construct a new diagnostic for identifying TDG candidates. The final aim was to measure the rotation curves of these galaxies, detecting the presence or absence of DM. This would then confirm which TDG candidates are bonafide TDGs and consequently allow me to determine the relative frequency of the TDG formation mechanism.

5.3 Catalogue and detection of star-forming dwarf group members

In the second chapter of this thesis (Paper 1) I detailed the selection of Choirs, the gas-rich groups of star-forming galaxies that form the sample for this work. The Choir groups are ideal for studying TDGs because they provide the necessary group environments for forming TDGs by fly-bys or weak interactions, without the young, expanding tidal tails that distort the mass measurements of many of the existing TDGs in the literature. Further to that, the star-forming nature of these dwarfs allows emission line metallicity measurements of a much larger sample than absorption line studies would allow.

Choir member galaxies were selected from the optical narrow-band $H\alpha$ imaging of SINGG (Meurer et al., 2006), an optical follow-up of HiPASS (Barnes et al., 2001), designed to measure the rate of formation of the highest-mass stars. The smallest galaxies within the Choir groups do not have sufficient HI gas to be detected on their own in HiPASS but are detected in SINGG because of their location within a HI-rich group of galaxies. Nearly all of the candidate member galaxies are confirmed to lie at the redshift of the HI group.

The Choir groups appear normal in terms of star formation efficiency and HI content. They are

more compact than the Local Group and groups in the Garcia (1993) catalogue but larger than Hickson compact groups Hickson et al. (1989). The member galaxies have normal radii, $H\alpha$ equivalent width, R -band surface brightness and specific star formation rates when compared to the wider SINGG sample. Consequently they form an ideal sample within which to determine the fraction of dwarf galaxies that is formed in a tidal manner.

5.4 The metallicity of tidal dwarf galaxies

In Chapter 3 (Paper 2) I developed a diagnostic for identifying TDGs in the absence of optical tidal streams. This diagnostic is based on the luminosity-metallicity relation for normal galaxies, since TDGs are more metal-rich for their size and luminosity. I used a consistent metallicity measurement for the 53 Choir member galaxies in my sample and all control samples, eliminating the calibration-dependent biases that plague other work (e.g. Kewley & Ellison, 2008). The SDSS control sample used to define this diagnostic contains two sub-populations of metal-rich giants and metal-medium dwarfs, and an apparent floor in metallicity for dwarfs fainter than $M_R = -16$, at $12 + \log(O/H) = 8.28 \pm 0.10$. The diagnostic is confirmed by Bekki's simulations of TDGs and by other TDG candidates in the literature, both of which have metallicities significantly elevated above the SDSS relation. I used this diagnostic to identify three (16% of dwarfs) strong TDG candidates ($12 + \log(O/H) > 8.6$), which have metallicities significantly above the SDSS control sample. I also identified four (21%) very metal-poor galaxies ($12 + \log(O/H) < 8.0$), which are consistent with Hydra cluster dwarfs (Duc et al., 2001). Unlike those in the literature, the TDG candidates I have identified do not lie within tidal streams, so they are more likely to have measurable dynamical masses (Casas et al., 2012).

5.5 The kinematics of tidal dwarf galaxies

In the penultimate chapter of this thesis I presented rotation curves of 22 galaxies, including six newly-discovered dwarfs, across four Choir groups. The simultaneous measurement of multiple rotation curves within a group is novel, and makes use of the wide field of view of the DEIMOS spectrograph and the large aperture of Keck. I identified three additional very strong TDG candidates using my new luminosity-metallicity diagnostic. I modelled the velocity fields of the sample and found that these galaxies have a large pressure-supported component, suggesting that they are influenced by weak tidal fields. The disturbed shape and small extent of many

of the rotation curves give further evidence of tidal effects even though there are no obvious signs of tidal interaction in most of the Choir groups. In fact, the smallest dwarfs in closest proximity to the giants are being tidally stripped of the very material required to measure a falling rotation curve. This affects as much of half of my sample, and similarly for other studies of TDGs in groups.

For the reliable rotation curves I measured low M/L ratios, as expected for these young, star-forming galaxies. One galaxy has a rotation curve that falls below the TDG mass-follows-light prediction, which could be explained as 1) a star-forming disk which is increasingly pressure-supported at large radii; 2) a tilted bar within a face-on disk; 3) a kinematic twist, where the line of nodes is twisted into the edges of the slit. The orientation of our slit and complexity of the galaxy mean that I cannot distinguish between these three scenarios with current data. The down-side of multi-object slit spectroscopy rotation curve measurements is that slit orientation choice is very limited. Slit orientation affects only 40% of my sample, as the galaxies' position angles are not completely random; for a randomly-distributed sample of inclined disks observed with DEIMOS I predict that 62.5% of galaxies would be unmeasurable. Integral field spectroscopy will overcome these observational effects, though is more observationally expensive. However, the physical effects of group tides remain, so that outer baryons are tidally removed. This renders it impossible to measure convincing falling rotation curves unless a newly-formed TDG becomes quickly but gently removed from the field in which it forms. Even in such a case, the H α light must be sufficiently bright at the outskirts to allow measurement. The falling rotation curves expected for TDGs are therefore very unlikely to be detectable.

5.6 Future work

The rarity of measurable falling rotation curves means that large surveys are required for their detection; while the variation in galaxy position angles necessitates integral field unit spectroscopy. These two constraints point to surveys such as the SAMI galaxy survey (Allen et al., 2014) as an ideal vehicle for future studies of TDGs. Integrated metallicity measurements should first be used to identify candidate TDGs that lie above the luminosity-metallicity relation. Detailed modelling of the 2D velocity field can then be conducted to determine which of the candidates have falling rotation curves. Finally, resolved HI emission line follow-up of the best candidates can be used to extend the optical measurement to higher radii, giving a

stronger detection of a falling rotation curve. Though rare, if a falling rotation curve is detected it would have serious consequences for the gravitational models that ascribe flat rotation curves to a modification to Newtonian dynamics (MOND, Gentile et al., 2007).

References

References for Chapters 2 and 3 are contained within those chapters.

Aguilar, L. A., & White, S. D. M. 1986, *ApJ*, 307, 97

Allen, J. T. et al. 2014, *ArXiv e-prints*, 1407.6068

Athanassoula, E., & Bosma, A. 1985, *ARAA*, 23, 147

Baldry, I. K. et al. 2012, *MNRAS*, 421, 621

Barnes, D. G. et al. 2001, *MNRAS*, 322, 486

Bekki, K., Couch, W. J., Drinkwater, M. J., & Gregg, M. D. 2001, *ApJL*, 557, L39

Bell, E. F., McIntosh, D. H., Katz, N., & Weinberg, M. D. 2003, *The Astrophysical Journal Supplement Series*, 149, 289

Benson, A. J., Bower, R. G., Frenk, C. S., Lacey, C. G., Baugh, C. M., & Cole, S. 2003, *ApJ*, 599, 38

Benson, A. J., Frenk, C. S., Lacey, C. G., Baugh, C. M., & Cole, S. 2002, *MNRAS*, 333, 177

Bode, P., Ostriker, J. P., & Turok, N. 2001, *ApJ*, 556, 93

Bournaud, F. 2010, *Advances in Astronomy*, 2010, 1

Bournaud, F., & Duc, P.-A. 2006, *A&A*, 456, 481

Bournaud, F. et al. 2007, *Science*, 316, 1166

Boylan-Kolchin, M., Bullock, J. S., & Kaplinghat, M. 2012, *MNRAS*, 422, 1203

Brodie, J. P., & Huchra, J. P. 1991, *Astrophysical Journal*, 379, 157

- Carignan, C., & Purton, C. 1998, *ApJ*, 506, 125
- Casas, R. A., Arias, V., Peña Ramírez, K., & Kroupa, P. 2012, *MNRAS*, 424, 1941
- Choi, P. I., Guhathakurta, P., & Johnston, K. V. 2002, *AJ*, 124, 310
- Dalcanton, J. J. 2007, *The Astrophysical Journal*, 658, 941
- de Blok, W. J. G., McGaugh, S. S., & van der Hulst, J. M. 1996, *MNRAS*, 283, 18
- De Rijcke, S., Buyle, P., & Koleva, M. 2013, *ApJL*, 770, L26
- Dénes, H., Kilborn, V. A., & Koribalski, B. S. 2014, *ArXiv e-prints*, 1407.1619
- Dopita, M. A., & Ryder, S. D. 1994, *ApJ*, 430, 163
- Dopita, M. A., Sutherland, R. S., Nicholls, D. C., Kewley, L. J., & Vogt, F. P. A. 2013, *ApJS*, 208, 10
- Doyle, M. T. et al. 2005, *Monthly Notices of the Royal Astronomical Society*, 361, 34
- Duc, P. A., Brinks, E., Springel, V., Pichardo, B., Weilbacher, P., & Mirabel, I. F. 2000, *The Astronomical Journal*, 120, 1238
- Duc, P. A., Cayatte, V., Balkowski, C., Thuan, T. X., Papaderos, P., & van Driel, W. 2001, *Astronomy & Astrophysics*, 369, 763
- Duc, P.-A. et al. 2011, *MNRAS*, 417, 863
- Duc, P.-A., & Mirabel, I. F. 1998, *A&A*, 333, 813
- Duc, P.-A., Paudel, S., McDermid, R. M., Cuillandre, J.-C., Serra, P., Bournaud, F., Cappellari, M., & Emsellem, E. 2014, *MNRAS*, 440, 1458
- Elmegreen, D. M., Elmegreen, B. G., Chromey, F. R., Hasselbacher, D. A., & Bissell, B. A. 1996, *AJ*, 111, 1880
- Emsellem, E., Fathi, K., Wozniak, H., Ferruit, P., Mundell, C. G., & Schinnerer, E. 2006, *MNRAS*, 365, 367
- Faber, S. M. 1973, *ApJ*, 179, 423
- Faber, S. M. et al. 2003, in *Society of Photo-Optical Instrumentation Engineers (SPIE) Conference Series*, Vol. 4841, *Instrument Design and Performance for Optical/Infrared Ground-based Telescopes*, ed. M. Iye & A. F. M. Moorwood, 1657–1669

- Font, A. S. et al. 2011, MNRAS, 417, 1260
- Fontana, A. et al. 2006, A&A, 459, 745
- Freeman, K. C. 1970, Astrophysical Journal, 160, 811
- Garcia, A. 1993, Astronomy & Astrophysics Supplement Series, 100, 47
- Garnett, D. R., & Shields, G. A. 1987, Astrophysical Journal, 317, 82
- Gentile, G., Famaey, B., Combes, F., Kroupa, P., Zhao, H. S., & Tiret, O. 2007, A&A, 472, L25
- Gibson, B. K., & Matteucci, F. 1997, Astrophysical Journal v.475, 475, 47
- Gómez, P. L. et al. 2003, ApJ, 584, 210
- Green, A. W. et al. 2014, MNRAS, 437, 1070
- Guo, Q., White, S., Li, C., & Boylan-Kolchin, M. 2010, MNRAS, 404, 1111
- Hickson, P., Kindl, E., & Auman, J. R. 1989, Astrophysical Journal Supplement Series (ISSN 0067-0049), 70, 687
- Hunsberger, S. D., Charlton, J. C., & Zaritsky, D. 1996, Astrophysical Journal v.462, 462, 50
- Iglesias-Paramo, J., & Vilchez, J. M. 1997, ApJ, 479, 190
- Kalinova, V., van de Ven, G., Lyubenova, M., Falcon-Barroso, J., & van den Bosch, R. 2013, in American Astronomical Society Meeting Abstracts, Vol. 221, American Astronomical Society Meeting Abstracts 221, 241.05
- Kauffmann, G. et al. 2003, MNRAS, 346, 1055
- Kewley, L. J., & Ellison, S. L. 2008, The Astrophysical Journal, 681, 1183
- Klypin, A., Kravtsov, A. V., Valenzuela, O., & Prada, F. 1999, ApJ, 522, 82
- Krajnović, D. et al. 2008, MNRAS, 390, 93
- Kroupa, P., Pawlowski, M., & Milgrom, M. 2012, International Journal of Modern Physics D, 21, 30003
- Larson, R. B. 1974, MNRAS, 169, 229
- Lequeux, J., Peimbert, M., Rayo, J. F., Serrano, A., & Torres-Peimbert, S. 1979, Astronomy & Astrophysics, 80, 155

- Lewis, I. et al. 2002, *MNRAS*, 334, 673
- Marino, R. A. et al. 2013, *A&A*, 559, A114
- Mayer, L., Governato, F., Colpi, M., Moore, B., Quinn, T., Wadsley, J., Stadel, J., & Lake, G. 2001, *ApJ*, 559, 754
- McGaugh, S. S., & de Blok, W. J. G. 1998, *ApJ*, 499, 41
- Mendes de Oliveira, C., Plana, H., Amram, P., Balkowski, C., & Bolte, M. 2001, *AJ*, 121, 2524
- Meurer, G. R., Carignan, C., Beaulieu, S. F., & Freeman, K. C. 1996, *AJ*, 111, 1551
- Meurer, G. R. et al. 2006, *ApJS*, 165, 307
- Milgrom, M. 1983, *ApJ*, 270, 365
- . 2007, *ApJL*, 667, L45
- Mirabel, I. F., Dottori, H., & Lutz, D. 1992, *Astronomy and Astrophysics* (ISSN 0004-6361), 256, L19
- Moore, B., Ghigna, S., Governato, F., Lake, G., Quinn, T., Stadel, J., & Tozzi, P. 1999, *ApJL*, 524, L19
- Navarro, J. F., Frenk, C. S., & White, S. D. M. 1997, *ApJ*, 490, 493
- Penny, S. J., Conselice, C. J., de Rijcke, S., & Held, E. V. 2009, *MNRAS*, 393, 1054
- Ploekinger, S., Hensler, G., Recchi, S., Mitchell, N., & Kroupa, P. 2014, *MNRAS*, 437, 3980
- Renaud, F., Boily, C. M., Naab, T., & Theis, C. 2009, *ApJ*, 706, 67
- Richer, M., McCall, M. L., & Stasińska, G. 1998, *A&A*, 340, 67
- Ryan-Weber, E. V. et al. 2004, *AJ*, 127, 1431
- Ryder, S. D., & Dopita, M. A. 1994, *ApJ*, 430, 142
- Ryś, A., Falcón-Barroso, J., & van de Ven, G. 2013, *MNRAS*, 428, 2980
- Sanders, R. H., & McGaugh, S. S. 2002, *ARAA*, 40, 263
- Shu, F. H. 1982, *The Physical Universe* (University Science Books)
- Skillman, E. D., Kennicutt, R. C., & Hodge, P. W. 1989, *Astrophysical Journal*, 347, 875

- Sweet, S. M., Drinkwater, M. J., Meurer, G., Bekki, K., Dopita, M. A., Kilborn, V., & Nicholls, D. C. 2014, *The Astrophysical Journal*, 782, 35
- Sweet, S. M. et al. 2013, *Monthly Notices of the Royal Astronomical Society*, 433, 543
- Toloba, E., Boselli, A., Cenarro, A. J., Peletier, R. F., Gorgas, J., Gil de Paz, A., & Muñoz-Mateos, J. C. 2011, *A&A*, 526, A114
- Tremonti, C. A. et al. 2004, *ApJ*, 613, 898
- Tully, R. B. 1988, *Nearby galaxies catalog* (Cambridge University Press)
- van den Bergh, S. 1988, *PASP*, 100, 344
- van der Marel, R. P., & Kallivayalil, N. 2014, *ApJ*, 781, 121
- van Zee, L., Haynes, M. P., Salzer, J. J., & Broeils, A. H. 1997, *AJ*, 113, 1618
- Vílchez, J. M., & Iglesias-Páramo, J. 2003, *The Astrophysical Journal Supplement Series*, 145, 225
- Weilbacher, P. M., Duc, P.-A., & Fritze-v. Alvensleben, U. 2003, *A&A*, 397, 545
- Weilbacher, P. M., Duc, P. A., Fritze-v Alvensleben, U., Martin, P., & Fricke, K. J. 2000, *Astronomy & Astrophysics*, 358, 819
- Zaritsky, D., Kennicutt, R. C. J., & Huchra, J. P. 1994, *Astrophysical Journal*, 420, 87